COVER PAGE

A convolutional, scale-adaptive framework for large-scale shoreline change modeling

Mohsen Taherkhani[a,b,c,1], Sean Vitousek[d], and Peter Ruggiero[e]

[a]Department of Civil, Environmental and Construction Engineering, University of Central Florida, Orlando, FL 32816, USA; [b]Center for Integrated Coastal Research, University of Central Florida, Orlando, FL 32816, USA; [c]Department of Civil and Construction Engineering, Oregon State University, Corvallis, OR 97331, USA; [d]U.S. Geological Survey, Pacific Coastal and Marine Science Center, Santa Cruz, CA 95060, USA; [e]College of Earth, Ocean, and Atmospheric Sciences, Oregon State University, Corvallis, OR 97331, USA.

[1]To whom correspondence should be addressed. E-mail: mohsen.taherkhani@ucf.edu

ORCID: https://orcid.org/0000-0002-9716-441X

This preprint has been submitted for publication in SCIENTIFIC REPORTS and is currently under review. This preprint has also been submitted to EarthArXiv. Subsequent versions of this manuscript may have slightly different content.

Keywords

U.S. Pacific Northwest (PNW) | *Satellite-derived shoreline observations* | *Shoreline change modeling* | *Convolutional framework* | *AI model interpretability*

A convolutional, scale-adaptive framework for large-scale shoreline change modeling

Mohsen Taherkhani[a,b,c,1], **Sean Vitousek**[d], **and Peter Ruggiero**[e]

This preprint manuscript was compiled on August 7, 2026. It is currently under consideration at a peer-reviewed journal. Conclusions may change in subsequent versions.

Understanding sandy beach evolution under geologic, hydrodynamic, morphologic, and anthropogenic influences, and particularly future climate variability and sea level rise, has become increasingly important. Several numerical models have been developed to simulate sandy beach evolution, ranging from high-fidelity, process-based models to reduced-complexity approaches, to data-driven and hybrid methods, and spanning scales from relatively small (hundreds of m-days) to relatively large (hundreds of km-decades). Data-driven approaches, however, often lack explicit representation of the physical processes governing shoreline change, a key sandy beach evolution metric. Here, we present a hybrid, scale-adaptive convolutional framework for shoreline change modeling that effectively bridges reduced-complexity and data-driven approaches and apply it to the U.S. Pacific Northwest sandy beaches (∼750 km, Oregon and Washington). Using 40 years (1984–2024) of primarily satellite-derived shoreline data, we hindcast shoreline position evolution across 22 littoral cells comprising over 10,000 transects at 50-m alongshore resolution. Hindcast results yield a median validation Root Mean Square Error of 14.1 m and a Mielke's index of 0.51, similar to recent shoreline-change benchmarks. Our framework is based on a sum of convolution operations over hydrodynamic forcing with optimized kernel functions to model shoreline response. The resulting kernel shapes quantify the beach's morphodynamic memory, revealing shoreline response timescales and magnitudes that vary systematically with geographical latitude and coastal orientation across the region. The framework's computational efficiency and physical interpretability make it well-suited for future stochastic shoreline projections under changing climatic conditions, ultimately supporting informed coastal management and adaptation policies.

U.S. Pacific Northwest (PNW) | Satellite-derived shoreline observations | Shoreline change modeling | Convolutional framework | AI model interpretability

Significance Statement

Accurately predicting shoreline change is vital for developing management strategies to safeguard coastal communities and ecosystems. This work introduces a data-driven shoreline change model that links traditional physical modeling approaches with Artificial Intelligence (AI)-based deep learning techniques. We apply this model to hindcast four decades (1984-2024) of historical shoreline evolution along the U.S. Pacific Northwest. By leveraging a large dataset of satellite-derived shoreline positions, our model is optimized to replicate the real-world variability of shorelines throughout the sandy beaches of the Pacific Northwest. As a reduced-complexity model, this approach is particularly well-suited for projecting future shoreline evolution in a probabilistic framework, accommodating a diverse range of climate change scenarios. These projections could assist coastal communities and stakeholders in managing climate-related coastal risks, contributing to enhanced resilience of vulnerable ecosystems and infrastructure.

Shoreline evolution, driven by both natural and anthropogenic forces, directly affects coastal economies, ecosystems, and infrastructure worldwide (1, 2). Predicting this evolution is therefore important for improving coastal management and adaptation planning (3). The physical factors that govern coastal evolution are increasingly well understood, yet accurately predicting shoreline change remains a significant challenge across various spatial and temporal scales (4, 5). Physics-based modeling stands as the backbone of modern shoreline change prediction through its integration of hydrodynamic, sediment transport, and geomorphic processes (6). Nonetheless, shoreline change modeling faces impediments, including the complexities of sediment dynamics, the interplay between natural and human influences, and the inherent uncertainties in climate and sea level projections (2).

Shoreline change modeling has transformed widely over the past four decades, spanning physics-based (process-based or full-physics), reduced-complexity (reduced-physics), and data-driven approaches. The emergence of modern computers and improved coastal monitoring technology sparked widespread adoption of physics-based models (e.g., Delft3D (7)) that mathematically combine small-scale processes to simulate coastal morphodynamics (8–15). While these models excel at simulating short-term hydrodynamic processes and morphodynamic responses to storms, their high computational cost and parametric uncertainty/sensitivity has limited their effectiveness for medium-to-long-term and large-scale shoreline evolution projections (16–18). In parallel, reduced-complexity modeling approaches began emerging as an alternative by relying on scarce but high-quality, long-term morphodynamic datasets to develop empirical predictions of shoreline change (19–25). Recent breakthroughs in AI and Deep Learning (DL) have accelerated the adoption of data-driven approaches in shoreline modeling. These methods are particularly attractive owing to their minimal reliance on prescribed governing equations and

Author affiliations: [a]Department of Civil, Environmental and Construction Engineering, University of Central Florida, Orlando, FL 32816, USA.; [b]Center for Integrated Coastal Research, University of Central Florida, Orlando, FL 32816, USA.; [c]Department of Civil and Construction Engineering, Oregon State University, Corvallis, OR 97331, USA.; [d]U.S. Geological Survey, Pacific Coastal and Marine Science Center, Santa Cruz, CA 95060, USA.; [e]College of Earth, Ocean, and Atmospheric Sciences, Oregon State University, Corvallis, OR 97331, USA.

[1]To whom correspondence should be addressed. E-mail: mohsen.taherkhani@ucf.edu

physical parameters, in tandem with the growing global availability of spatiotemporally high-resolution satellite imagery (24, 26–29). Hybrid models have also emerged that combine elements of reduced-complexity and data-driven approaches and offer a middle ground by balancing computational efficiency with physical process representation while incorporating observations (13, 30–34). However, challenges remain regarding model generalizability and the ability to extrapolate beyond training datasets, particularly over long-term periods (35–37). Furthermore, while the data-driven models demonstrate increasing popularity and high potential in shoreline modeling (e.g., refs. (29, 36, 38–41)), their rapid adoption in coastal morphodynamics, among other fields of geoscience, has raised questions regarding their interpretability, i.e., the ability to understand the physical mechanisms underlying a model's predictions. The increasing emphasis on interpretability has motivated the development of explainable AI (XAI) (42, 43), a growing movement aimed at reducing the "black-box" nature of AI models that do not explicitly follow known physical relationships (36). Shoreline change models thus stand to benefit from frameworks that bridge reduced-complexity and data-driven approaches, incorporating physical understanding to improve interpretability.

Among reduced-complexity approaches, "equilibrium" models stand out for various reasons (13). They are based on the notion that coastal morphodynamics consistently evolve towards an equilibrium state, dynamically responding to external oceanic forcings such as wave action and sea level change. Thus, changes in these forcings create morphodynamic "disequilibrium," triggering the coastal morphology to transition towards a new equilibrium state (13). These approaches have known limitations where geologic settings and sediment supply highly influence shoreline behavior at seasonal-to-interdecadal time scales (44–46). Yet, the capacity to incorporate key forcing variables while preserving a balance between simplicity, predictive skill, and computational efficiency has established this concept as the main principle underlying several prominent shoreline evolution models (e.g., refs. (47–49)). The core tenet in equilibrium models posits that the variations in oceanic forcings during a specific antecedent period contribute most to driving morphodynamics toward a new equilibrium state, but because the forcing conditions are constantly changing, the "memory" or influence of antecedent conditions on the morphodynamic state decreases over time. This concept essentially outlines the fundamentals of convolution, which was initially implemented in the field of coastal morphodynamics by Kriebel and Dean (1993) (50), and subsequently revisited by Miller and Dean (2004) (47), although its full potential in shoreline modeling at that time was not realized. Recently, Vitousek et al. (2025) (51) re-vitalized the convolution approach by demonstrating that equilibrium models (i.e., refs. (48, 49)) are theoretically equivalent to the numerical concept of a discrete convolution operation. In their approach, an exponential "memory window" (or "kernel") is convolved with a forcing signal, meaning that the forcing signal's influence on shoreline change at a specific time diminishes exponentially as time progresses. Their model demonstrated strong performance in the 2024 ShoreShop 2.0 benchmarking competition (37, 52).

Despite these advances in equilibrium and convolutional modeling, no existing approach yet links reduced-complexity and data-driven methods to provide region-scale shoreline hindcasts that are simultaneously computationally efficient, physically interpretable, and validated against high-resolution observational data across diverse littoral settings. In this work, we focus on the sandy beaches of the U.S. Pacific Northwest (PNW), extending $\sim$750 km along the U.S. West Coast and encompassing the coasts of Oregon and Washington. Spanning approximately 42°N to 48°N, the PNW coast is predominantly composed of dissipative, low-sloping (median slope of $\tan\beta \sim 0.025$), mesotidal beaches exposed to energetic wave conditions (53–56). This region is broken up into 22 morphologically distinct, pre-defined littoral cells approximately tens of kilometers in length, bordered by intermittent headlands and bay or river inlets (5, 55, 57). Throughout the PNW, shoreline variability is mainly driven by sea level fluctuations, changing storminess patterns, large-scale climate modes—particularly El Niño-Southern Oscillation (ENSO) and Pacific Decadal Oscillation (PDO)—and riverine and estuarine sediment contributions (sources and sinks) (5, 55, 56, 58–61). Several shoreline modeling studies have been conducted for the sandy beaches of the PNW (e.g., refs. (5, 61–66)). However, these modeling efforts have generally been limited to specific coastal extents throughout the region, covering only a few littoral cells at most, and, except ref. (67), do not effectively incorporate various modes of shoreline evolution, such as cross-shore and alongshore components, across different temporal scales.

The goal of this study is to provide the first hindcasts of shoreline position evolution (1984-2024) across the sandy beaches of the entire PNW at a high spatial resolution (10,599 shore-normal transects at 50-m-alongshore spacing across 22 littoral cells). Following the work of Vitousek et al. (2025) (51), we develop a hybrid, convolutional model that bridges reduced-complexity and data-driven approaches. This model is based upon three fundamental pillars, grounded in the findings of Taherkhani et al. (2026) (56), who used a composite of lidar-, GPS-, and satellite-derived shoreline positions (1984–2024) throughout the PNW to identify distinct modes of shoreline position variability. The *first pillar* involves specifying different modes of shoreline position evolution, wherein the cross-shore and alongshore modes together account for over 90% of the variability in detrended shoreline positions averaged across all 22 analyzed littoral cells. The *second pillar* involves prescribing predominant types of oceanic forcing, i.e., wave energy, water level variation, or a combination thereof, that drives each mode of shoreline position variability. The *final pillar* concerns the formulation and optimization of equilibrium timescale functions (or kernel function), as "morphodynamic memory," that effectively link each modal shoreline response to its corresponding oceanic forcing. This three-pillar framework ensures the multi-scale or "scale-adaptive" character of our approach, as well as its grounding in real-world/observed behavior across the PNW. Our modeling effort also highlights the important contribution of satellites, the planet's most extensive resource of coastal change data, utilized for both calibrating and validating the model, which enables us to create a "model at the scales of data" (28). In what follows, we first present transect-scale hindcast performance spanning 22 studied littoral cells in the PNW. We then report shoreline variability component-level performance at the littoral cell scale for Sand Lake (Oregon) and Long Beach (Washington), selected for their contrasting geological, morphological, and geographical characteristics. Finally, we examine what the optimized kernel properties reveal about morphodynamic memory across the PNW, including how shoreline responses vary with geographical latitude and coastal orientation.

Results

Hindcast performance.

The U.S. Pacific Northwest. We perform transect-scale shoreline position hindcasting to encompass all 10,599 sandy beach transects, spaced 50 m alongshore, across the 22 pre-defined littoral cells in the PNW, covering the entirety of Oregon's and most of Washington's sandy beaches (Refer to Supporting Information [SI] for details on Washington coast coverage). We hindcast total shoreline position (Y_t), the quantity directly observable via satellite or ground truth methods (Refer to Materials and Methods and SI for details on the composite of observed satellite-, lidar-, and GPS-derived shoreline position data), modeled as the linear superposition of five components: cross-shore seasonal (Y_{CS}), cross-shore interannual (Y_{CI}), alongshore (Y_{Al}), relative sea level rise-induced (Y_{RSLR}), and residual interdecadal trend (Y_R), each described in further detail in the Sand Lake hindcast subsection below. The hindcast spans 40 years (1984–2024), with the first 30 years (1984–2014) used for calibration, during which model parameters are optimized, and the final 10 years (2014–2024) reserved for validation against withheld observations. We evaluate hindcast performance during both calibration and validation periods using four metrics: the Pearson correlation coefficient ($Corr$), standard deviation (STD), Root Mean Square Error ($RMSE$), and Mielke's index (λ). Of these, $Corr$ and STD are used during optimization, $Corr$ as the objective function (Eq. 22) and STD for amplitude scaling (Eq. 23), while $RMSE$ and λ serve as independent performance metrics. Mielke's index is a dimensionless skill metric ranging from 1 (perfect agreement) to 0 (no skill). Refer to Eqs. 17, 18, 19, and 20 in Materials and Methods for the mathematical definitions of these metrics.

Fig. 1 illustrates hindcast performance across the PNW (Fig. 1a-b) over the 1984–2024 period. During the validation period, the model achieves a median $RMSE$ of 14.1 m (Inter-quartile range [IQR]: 10.5-19.4 m) and an unweighted median $Corr$ of 0.57 (IQR: 0.37-0.69), with approximately 77% of transects exhibiting $RMSE$ below 20 m and 66% exceeding $Corr$ of 0.50 (Fig. 1b). Also, the PNW-wide median Mielke's index is 0.51 (IQR: 0.30-0.63; Fig. 1d). The Taylor diagram (Fig. 1c) integrates $Corr$, STD, and $RMSE$ into a unified view, with diamond and star symbols distinguishing calibration and validation periods, respectively. Mielke's index (Fig. 1d) reveals comparable performance between calibration and validation for most littoral cells: median λ for Oregon, Washington, and the broader PNW during validation (calibration) is 0.53 (0.66), 0.46 (0.67), and 0.51 (0.66), respectively. Component-specific Mielke's index and $RMSE$ values, i.e., for cross-shore seasonal (CS), cross-shore interannual (CI), and alongshore (Al) components, across all 22 littoral cells are presented in SI Fig. S3. STD, as a complementary performance parameter, provides valuable context for interpreting the spatial variability of $RMSE$. As evident in Fig. 1b, transects with higher observed shoreline variability tend to exhibit higher $RMSE$, reflecting a close spatial relationship between the two metrics across the region. This spatial consistency in hindcast performance is further confirmed by the normalized Taylor diagram (Fig. 1c), where transect-scale metrics cluster tightly during both calibration and validation periods, indicating coherent model behavior across littoral cells. However, spatially variable performance is evident near estuarine and riverine entrances, as discussed below.

Beyond these summary metrics, Fig. 2 presents the observed and modeled total shoreline positions across all 22 littoral cells over the full 1984-2024 period. In Fig. 2, a transect-specific, 40-year linear trend is removed from the observed shoreline positions, while the modeled interdecadal trend components (Y_{RSLR} and Y_R), computed for all transects following the procedure described in Materials and Methods, are excluded from the modeled positions, to promote the visualization of seasonal-to-interannual variability. These linear trends, for both observed and modeled positions, are retained when computing total shoreline positions (Y_t) used in the overall model performance evaluation (Fig. 1). These heatmaps (often called hovmöller diagrams) provide a comprehensive view of the spatiotemporal evolution of shoreline positions throughout the PNW, illustrating the model's ability to capture both the timing and magnitude of shoreline variability at regional scale. The close agreement between observed and modeled patterns across most of the coastline is visually apparent at both seasonal and interannual scales. At interannual scales, several littoral cells, particularly in central and northern Oregon, exhibit pronounced multi-year trends accounting for tens of meters of shoreline variability, which the model reproduces satisfactorily—PNW-wide median $RMSE$ values for the CI and Al components range from $\sim$7.1 m to $\sim$8.3 m, with calibration and validation periods in close agreement (Refer to SI Fig. S3). At seasonal scales, the effects of exceptionally energetic wave seasons and elevated water levels during El Niño years are visible across the PNW, notably during the winters of 1997-1998 and 2015-2016 (54, 56, 69). The 2015-2016 El Niño signal is particularly noteworthy because it falls within the validation period and is captured by the model without being informed by shoreline observations. This signal is most prominently visible across central and northern Oregon littoral cells. Hindcast performance is generally strongest for open-coast transects away from estuarine influences.

Despite the overall satisfactory performance, notable spatial variability in hindcast metrics is evident across the region (Figs. 1b and 2). This variability follows a recurrent regional pattern, where sandy beaches situated near estuarine

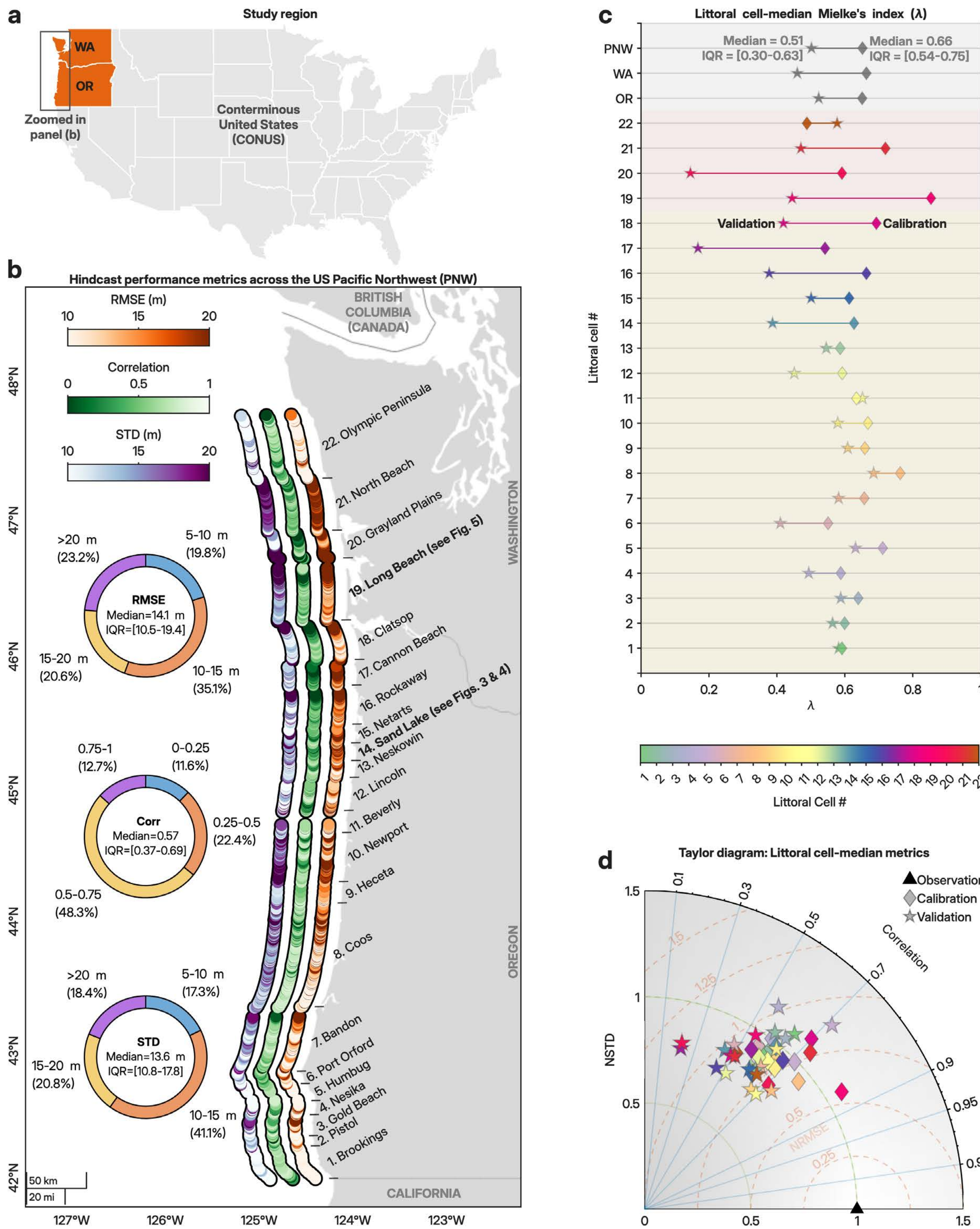

Fig. 1. Hindcast performance across the 22 analyzed littoral cells in the PNW. (a) Study region highlighting the outer coast of the U.S. Pacific Northwest (PNW), encompassing the sandy beaches of Oregon and Washington. **(b)** Hindcast performance metrics (during the validation period—2014-2024), namely Root Mean Square Error ($RMSE$), Pearson correlation coefficient ($Corr$), and standard deviation (STD) across all 10,599 sandy beach transects (with 50-m alongshore spacing) within the 22 analyzed littoral cells throughout the PNW—refer to Materials and Methods for formal definitions of each performance metric. Donut charts show the distribution of transects across magnitude intervals for each metric. The median values and inter-quartile ranges (IQRs) for the PNW are depicted in the center of each chart. Sand Lake and Long Beach littoral cells, examined in detail in Figs. 3–5, are indicated in bold. **(c)** The normalized Taylor diagrams, adjusted (normalized) for standard deviation ($NSTD$) and Root Mean Square Error ($NRMSE$), depict the littoral cell-median performance metrics corresponding to total shoreline positions during the calibration (1984-2014) and validation (2014-2024) periods, marked with diamonds and stars, respectively (colored per the colorbar for each littoral cell). **(d)** Littoral cell-median Mielke's index (λ; where 0 indicates no skill and 1 indicates perfect agreement, accounting for both correlation and bias) during calibration and validation periods (indicated by diamonds and stars, respectively), for individual littoral cells and aggregated across Oregon (OR), Washington (WA), and the PNW. Similarly, the indices are colored per the colorbar for individual littoral cells. Credit: basemaps, Natural Earth (via MATLAB (68)).

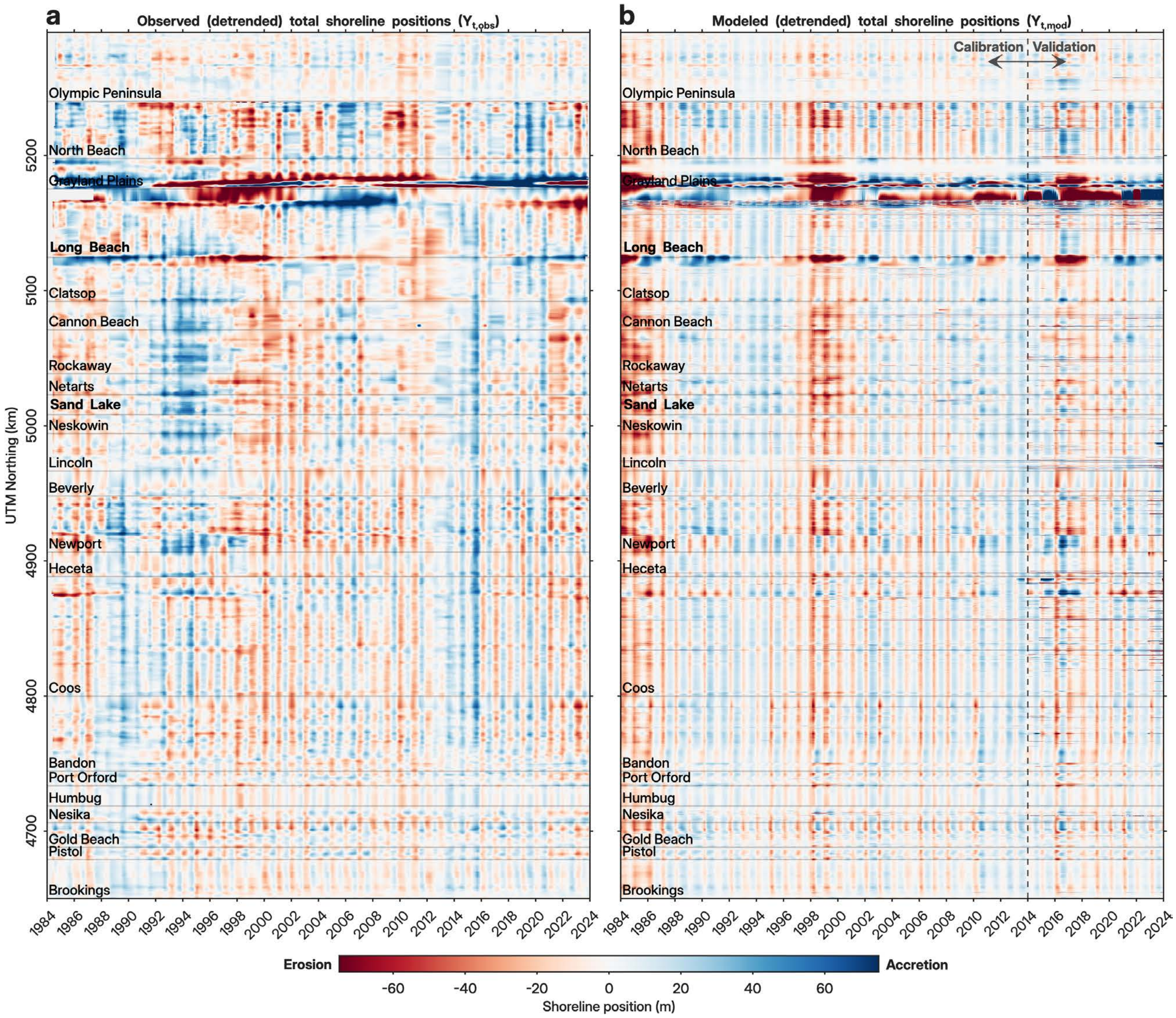

Fig. 2. Comparison of the detrended observed and modeled (hindcast) shoreline positions across the PNW during 1984-2024. Detrended **(a)** observed and **(b)** modeled (hindcast) total shoreline positions ($Y_{t,obs}$ and $Y_{t,mod}$, respectively, in meters) across the 22 analyzed littoral cells in the PNW from 1984 to 2024, displayed as spatiotemporal heatmaps where the y-axis represents alongshore position (UTM Northing) spanning all littoral cells from south (Brookings) to north (Olympic Peninsula), and the x-axis represents time. For observations, a 40-year linear trend is removed from each transect. For modeled positions, the interdecadal relative sea level rise-induced (Y_{RSLR}) and residual trend (Y_R) components are excluded to promote the visualization of seasonal-to-interannual variability. Positive values indicate accretion (seaward shoreline movement), and negative values denote erosion (landward shoreline movement). Sand Lake and Long Beach littoral cells, examined in detail in Figs. 3–5, are indicated in bold. The dashed vertical line in panel (b) separates the calibration (1984–2014) and validation (2014–2024) periods.

entrances often exhibit lower hindcast accuracy than adjacent open-coast segments. In Oregon, prominent examples include the entrances of Rogue River in Gold Beach littoral cell (SI Fig. S10), Coos Bay and Siuslaw and Umpqua Rivers in Coos littoral cell (SI Fig. S15), Yaquina Bay in Newport littoral cell (SI Fig. S17), Siletz Bay in Lincoln littoral cell (SI Fig. S19), Netarts Bay in Netarts littoral cell (SI Fig. S21), and Tillamook Bay in Rockaway littoral cell (SI Fig. S22). In Washington, this pattern is particularly pronounced near the entrances of Columbia River, Willapa Bay, and Grays Harbor, which separate the coastline between Clatsop (in Oregon) and North Beach littoral cells (Fig. 1 and SI Figs. S25-26). A notable example is the southern extremity of Grayland Plains littoral cell, adjacent to Willapa Bay entrance, which contains one of the most rapidly eroding shorelines in the continental U.S., with contemporary (1984–2024) erosion rates of up to 20 m/year (55) (Refer to SI Fig. S25). These reduced-performance extents indicate the complexity of estuarine and riverine sediment exchange processes, including localized sediment sources, sinks, and morphological features (e.g., ebb-tidal deltas) that are not captured by our framework's regional-scale forcing inputs. Conversely, performance metrics generally improve with increasing distance from these estuarine influences.

Sand Lake littoral cell. Sand Lake littoral cell is relatively short (∼12 km) and situated along the coast of Tillamook County in northern Oregon. The beaches of Tillamook County, extending from Cascade Head (south) to Cape Falcon (north), include extensive sandy beaches interlaced with headlands and steep bluffs. This littoral cell, spanning from Cape Kiwanda in the south to Cape Lookout in the north (Refer to Fig. 3), is notable for its considerable sand deposits (with a median sand grain size of ∼0.2 mm (55)), particularly at the northern extremity where a dune sheet extends well inland. Sand Lake littoral cell is sparsely inhabited and encompasses the unjettied Sand Lake estuary near its center. Despite its sand-rich character, long-term historical measurements reveal a net erosional pattern, with approximately 63% of the littoral cell's extent undergoing erosion (1960s through 2002) (55). This littoral cell is also situated on a segment of the Oregon coast undergoing relative submergence due to rising sea level that outpaces the region's slight tectonic uplift (55, 70). The Empirical Orthogonal Function (EOF) decomposition of satellite-derived shoreline positions (1984-2024 (56)—Refer to SI and SI Fig. S1) indicates that Sand Lake, akin to other littoral cells in central-northern Oregon coast, is predominantly driven by cross-shore variability. Among the top three EOF modes, explaining ∼94% of the variability in total, the cross-shore component of shoreline positions (i.e., mode 1) accounts for ∼78%.

At the transect scale, we use time series of significant wave height (H_s), peak wave period (T_p), wave direction (θ), and still water level (η_{SWL}; Refer to Materials and Methods and SI for details on the historical hydrodynamic data) to construct the forcing functions (F), one of the two central elements of our convolutional framework, the other being the kernel functions (K), for each component of shoreline position variability (Refer to Materials and Methods for details). Fig. 3a-d shows these hydrodynamic forcings at an example transect (transect #51 out of 257, from south to north) within Sand Lake littoral cell, identified by the orange triangle in Fig. 3e. The forcing functions for the cross-shore seasonal (F_{CS}), cross-shore interannual (F_{CI}), and alongshore (F_{Al}) components (Fig. 3f, i, l) are defined via Eqs. 6, 8, and 11, respectively. Each forcing function (F) is convolved ($*$) with its corresponding optimized kernel function (K; Fig. 3g, j, m) to produce the component-wise hindcast shoreline positions (Y) during 1984–2024. Fig. 3h, k, and n compare the observed and modeled shoreline positions at this example transect for each component, i.e., cross-shore seasonal (Y_{CS}), cross-shore interannual (Y_{CI}), and alongshore (Y_{Al}). The component-wise observed shoreline positions are derived from the EOF decomposition described in Materials and Methods. For each transect, 13 parameters are optimized across the three kernel functions (K_{CS}, K_{CI}, K_{Al}) and the alongshore forcing function (F_{Al}); Refer to Materials and Methods for details. Shaded regions in these panels represent the 95% confidence intervals (C.I.) derived from autoregressive (AR)-based uncertainty quantification (Refer to Materials and Methods). The remaining two components—the relative sea level rise-induced trend (Y_{RSLR}; Eq. 15) and the residual interdecadal trend (Y_R; Eq. 16), capturing shoreline change not explicitly accounted for by wave activity or sea level rise—are shown in Fig. 3o. The 95% C.I. for these two components is derived via block-bootstrapping (with replacement) of the historical SWL and shoreline position time series, respectively. The total modeled shoreline position (Y_t; Eq. 3) is presented alongside observations in Fig. 3p, where the 95% C.I. is derived from the summed component ensembles.

At this example transect within Sand Lake littoral cell, during the 30-year calibration period (1984-2014), the cross-shore seasonal component achieves $RMSE = 11.2$ m and $Corr = 0.69$, while the cross-shore interannual component yields $RMSE = 12$ m and $Corr = 0.63$. The cross-shore seasonal component maintains consistent performance during validation (2014-2024; $RMSE = 10.5$ m, $Corr = 0.77$). However, the cross-shore interannual component decreases during validation ($Corr = -0.09$), indicating the difficulty of validating a very low-frequency signal with only a few effective cycles within a 10-year window. Nonetheless, the validation $RMSE$ of 9.6 m for this component remains comparable to its calibration value (12 m), suggesting that the poor correlation reflects phase misalignment of a low-frequency signal rather than a fundamental failure in capturing its magnitude. The alongshore component achieves $RMSE = 7.8$ m and $Corr = 0.44$ during calibration and $RMSE = 10$ m and $Corr = 0.19$ during validation, indicating that hindcasting this component at this location is more challenging than the cross-shore components. Nevertheless, the total shoreline position at this transect achieves $RMSE = 17.6$ m, $Corr = 0.62$, and $\lambda = 0.63$ during calibration, and $RMSE = 12.1$ m, $Corr = 0.70$, and $\lambda = 0.60$ during validation, with the latter demonstrating moderate-to-high accuracy based on the PNW-wide metric distributions. This performance is primarily driven by the cross-shore dominated morphodynamics of Sand Lake littoral cell, where cross-shore components account for ∼78% of the total ∼94% variance explained by the top three EOF modes (Refer to SI Fig. S1). The alongshore component contributes only ∼16%, and its lower skill has a proportionally small effect on total shoreline position hindcast performance.

The interdecadal sea level rise-induced trend (Y_{RSLR}; Fig. 3o), estimated via the Bruun rule (Eq. 15), indicates a negligible erosional signal at this transect, consistent with the modest rate of relative sea level rise at the nearest tide gauge (2.52 ± 0.6 mm/year [95% C.I.] during 1970-2024; Garibaldi, Oregon, station ID: 9437540) (71). In contrast, the residual interdecadal trend (Y_R) shows a larger accretional signal, resulting in a net positive (marginally accretional) interdecadal trend at this location.

The optimized kernel functions (K_{CS}, K_{CI}, K_{Al}; Fig. 3g, j, m) differ in their "peak response time" (τ_{peak}, the time to peak kernel amplitude) and "effective morphodynamic memory" (τ_{eff}, the duration over which a forcing event appreciably influences shoreline position, defined as the time at which the kernel amplitude decays to 1% of its peak value), representing the distinct timescales of each component. At this example transect, τ_{peak} (τ_{eff}) values are approximately 3.9 (16.4), 0.6 (43.6), and 22.6 (110.3) months for the cross-shore seasonal, cross-shore interannual, and alongshore components, respectively. The physical interpretation of these kernel properties and their spatial variability across the PNW are examined in detail in the Morphodynamic Memory subsection below.

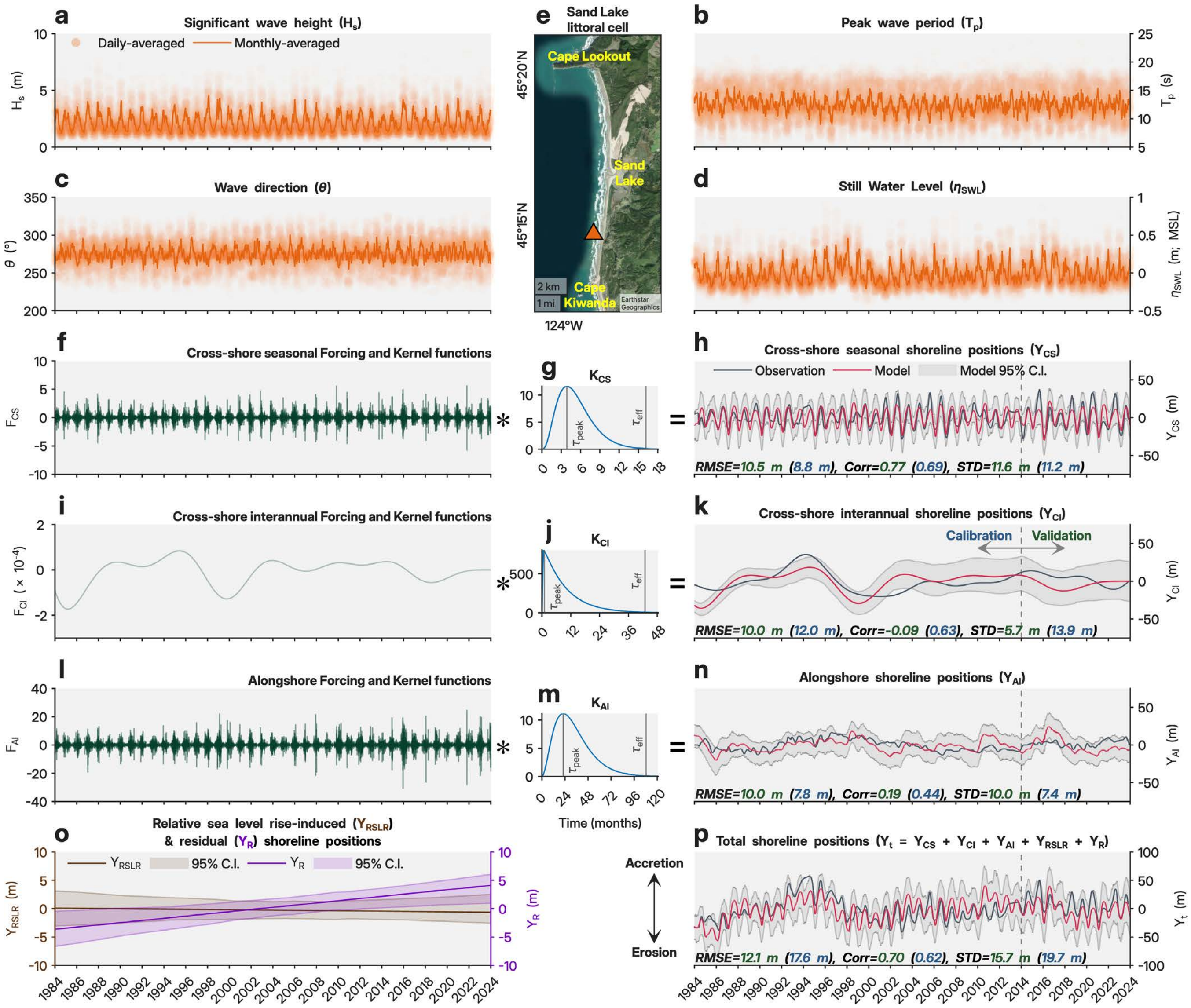

Fig. 3. Time series of hydrodynamic forcings, convolutional forcing (F) and kernel (K) functions, and the components of shoreline position variability and their hindcast performance at an example transect in Sand Lake littoral cell, Oregon. Time series of **(a)** significant wave height (H_s), **(c)** peak wave period (T_p), **(d)** wave direction (θ), and **(e)** Still Water Level height (η_{SWL}). **(b)** The location of the example transect (transect #51, from south to north, among 257 transects) within this littoral cell (highlighted by the orange triangle). Refer to Fig. 1 for the location of this littoral cell on the Oregon coast. **(f-n)** Each row of panels represents the time series of the forcing (F; left) and kernel (K; center—calibrated to best reproduce the observed shoreline positions) functions utilized in the convolutional framework ($F * K = Y$), the observed and modeled (hindcast) shoreline positions for distinct components of shoreline position variability (right), namely, cross-shore seasonal (CS), cross-shore interannual (CI), and alongshore (Al) components. τ_{peak} and τ_{eff}, highlighted on panels (g), (j), and (m), respectively denote "peak response time" and "effective morphodynamic memory," which are the time at which the kernel function reaches its maximum amplitude and the total duration over which a forcing event exerts appreciable influence on shoreline positions. Gray shading in panels (h), (k), and (n) represents the 95% confidence intervals (C.I.) of the hindcast, derived from autoregressive (AR) residual-based uncertainty quantification (Refer to Materials and Methods for details). **(o)** Time series of the modeled relative sea level rise-induced and residual shoreline position variability (i.e., Y_{RSLR} and Y_R, respectively). The 95% C.I. for these two components is derived via block-bootstrapping (with replacement) of the historical SWL and shoreline position time series, respectively (Refer to Materials and Methods). **(p)** Time series of total shoreline positions (Y_t), i.e., the superposition of the observed and modeled shoreline positions in panels (h), (k), (n), and (o), respectively. The 95% C.I. for Y_t in panel (p) is derived from the summed component ensembles. The Root Mean Square Error ($RMSE$), Pearson correlation coefficient ($Corr$), and standard deviation (STD) for the hindcast individual components and the total shoreline positions, during both calibration (1984-2014) and validation (2014-2024) periods, are shown in corresponding panels, with validation values shown first and calibration values in parentheses. Credit: basemaps, Earthstar Geographics (via MATLAB (68)).

We extend the transect-scale analysis to all 257 sandy beach transects across Sand Lake littoral cell. Fig. 4a-c presents the spatiotemporal variability of total observed ($Y_{t,obs}$) and modeled ($Y_{t,mod}$) shoreline positions, alongside their difference ($\Delta Y_t = Y_{t,obs} - Y_{t,mod}$) throughout this littoral cell. Validation-period performance metrics for all 257 transects are shown in Fig. 4e, with littoral cell-scale medians of $RMSE = 16.0$ m (IQR: 14.5-18.5 m), $Corr = 0.45$ (IQR: 0.31-0.61), and $\lambda = 0.39$ (IQR: 0.29-0.54; Refer to Fig. 1c). Based on the PNW-wide metric distributions, these values demonstrate fair hindcast accuracy across this littoral cell. The median STD (14.7 m) contextualizes the $RMSE$, indicating that the model error is comparable to the natural shoreline variability at this littoral cell. The

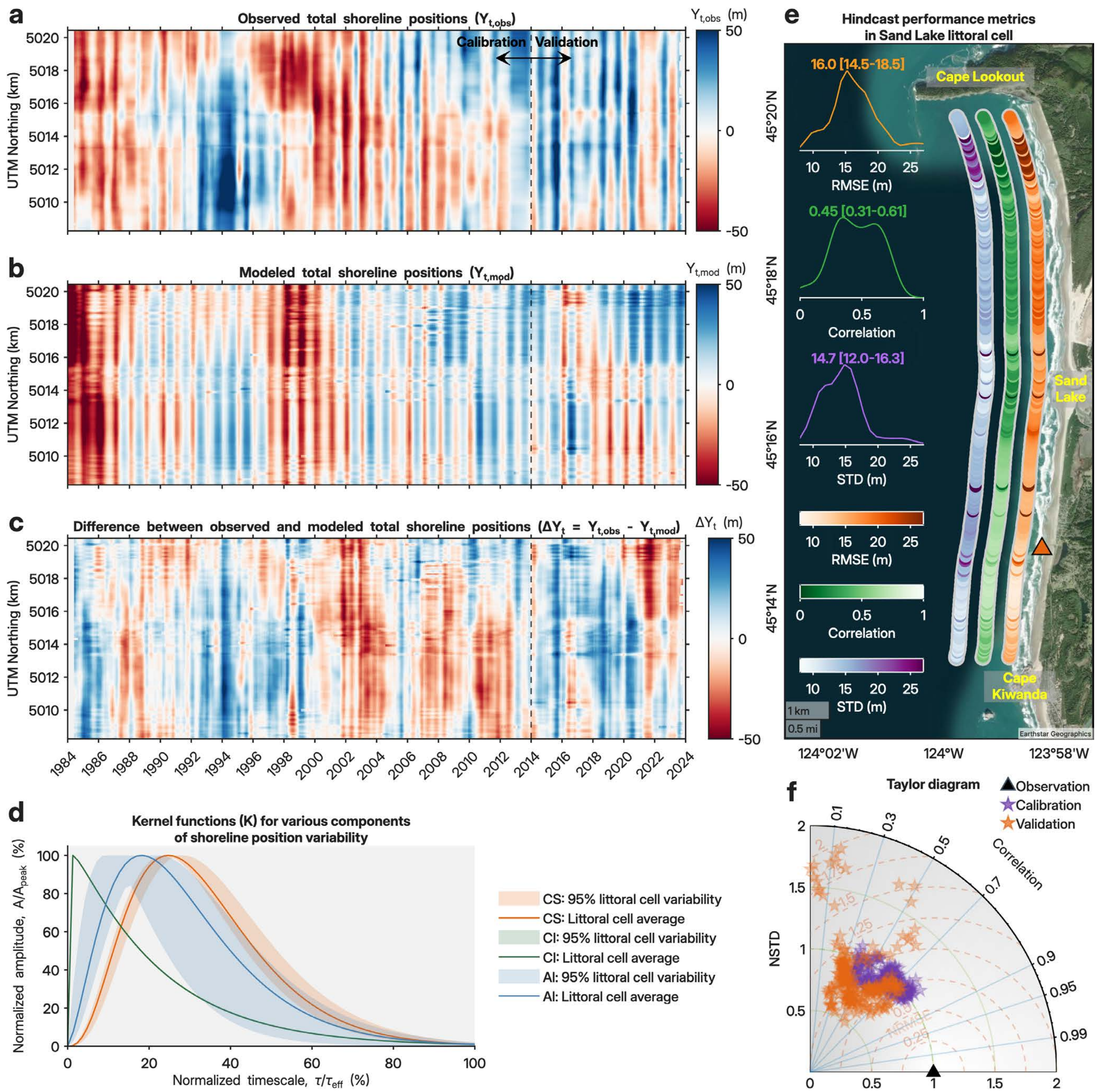

Fig. 4. Hindcast performance of the historical (observed) shoreline positions throughout Sand Lake littoral cell, Oregon. Spatiotemporal representation (heatmap; y-axis denotes the UTM northing and x-axis specifies time) of the total **(a)** observed ($Y_{t,obs}$) and **(b)** modeled (hindcast) ($Y_{t,mod}$) shoreline positions, alongside **(c)** their difference ($\Delta Y_t = Y_{t,obs} - Y_{t,mod}$). The dashed vertical line separates the calibration (1984–2014) and validation (2014–2024) periods. **(d)** The normalized (adjusted for amplitude [A] and effective morphodynamic memory [τ_{eff}]) shapes of the convolution kernel functions (K) optimized for all transects across this littoral cell, colored by component (orange: CS, green: CI, blue: Al), with solid lines representing the littoral cell average and shading denoting the 95% within-littoral cell variability across transects. **(e)** Spatial (alongshore) variability of the Root Mean Square Error ($RMSE$), Pearson correlation coefficient ($Corr$), and standard deviation (STD) of the modeled total shoreline positions during the validation period (2014-2024) in this littoral cell. This panel also features the kernel density estimation (KDE) for each metric across all transects within this littoral cell, alongside their littoral cell-median values and inter-quartile ranges (IQRs) shown above each KDE (the y-axis is not scaled). The location of the example transect showcased in Fig. 3 is indicated by the orange triangle in this panel. Refer to Fig. 1 for the location of this littoral cell on the Oregon coast. **(f)** The normalized (for standard deviation [$NSTD$] and Root Mean Square Error [$NRMSE$]) Taylor diagrams for the total shoreline position variability of all transects in this littoral cell, during both calibration and validation periods, where each point corresponds to an individual transect. Credit: basemaps, Earthstar Geographics (via MATLAB (68)).

model captures both seasonal and interannual patterns of cross-shore variability well throughout the calibration period, as visually apparent in Fig. 4a-b. Performance during validation is roughly consistent with calibration across most transects, as confirmed by the tight clustering in the normalized Taylor diagram (Fig. 4f). Hindcast accuracy is strongest in the southern half of the littoral cell, with metrics declining toward the northern half where larger accretional residual trends and elevated shoreline variability are present. Component-specific performance across this littoral cell follows the patterns noted at the example transect, where the cross-shore seasonal component performs consistently across calibration and validation, the cross-shore interannual component shows reduced validation skill due to limited low-frequency cycles, and the alongshore component remains the most challenging to hindcast (Refer to SI Fig. S3 for component-level metrics). The normalized kernel shapes across all transects in this littoral cell (Fig. 4d) show within-cell consistency, with the 95% variability band confirming that kernel shapes are coherent across transects for each component. The spatial patterns and physical interpretation of these kernels are examined in the Morphodynamic Memory subsection below.

Long Beach littoral cell. Long Beach littoral cell, a subcell of the Columbia River Littoral Cell (CRLC)—also including Clatsop in Oregon, and Grayland Plains and North Beach littoral cells in Washington (Refer to Fig. 1b)—stretches roughly 44 km along the southern Washington coast, making it one of the longest in the PNW. Bounded by the northern jetty of the Columbia River to the south and the unjettied entrance of Willapa Bay to the north (illustrated in Fig. 5e), this coastal segment features gently sloping beaches backed by vegetated foredunes and is characterized by well-sorted medium to fine sand (55). Historical monitoring campaigns and numerical analyses (e.g., refs. (55, 61, 65)) have revealed a nuanced coastal system that, while exhibiting strong accretionary trends over extended time frames, displays considerably greater complexity at shorter time scales, with transient hydrodynamic events and localized erosional hotspots reflecting reversals in longshore sediment transport patterns. Although jetty construction at the southern boundary contributed to accretionary trends over multidecadal timescales (59), it remains uncertain how these trends will evolve in the future, in part given that sediment supply from the Columbia River has substantially diminished over the past century due to interventions such as damming (59). Relatively high tectonic uplift rates over much of Long Beach littoral cell largely offset sea level rise, resulting in near-zero net contemporary relative sea level change (55). This littoral cell is distinct within the PNW coastal system as its multidecadal trends are driven primarily by alongshore morphological variability (56). It represents the only littoral cell in the PNW where the primary mode (i.e., mode 1) of EOF decomposition of the detrended satellite-derived shoreline positions during 1984-2024 has been associated with alongshore variability, explaining roughly 50% of the ∼85% total variability captured by the top three EOF modes. Furthermore, modes 1 and 3 together account for 62% of total variability, both associated with alongshore processes (56).

For brevity, transect-scale hindcast performance at two contrasting locations within Long Beach littoral cell, one near the southern jetty-influenced boundary (Benson Beach) and one relatively near the littoral cell midpoint, is presented in SI Fig. S2. We extend the analysis to all 839 transects across Long Beach littoral cell. Fig. 5a-c presents the observed, modeled, and residual total shoreline positions throughout this littoral cell. The heatmaps reveal that the model reproduces the interannual-to-interdecadal trends evident in the observations across the broad spatial extent of this cell. The residual panel (Fig. 5c) confirms this, with differences between observed and modeled positions remaining small relative to the total signal across most of the littoral cell, except at the northern extremity of this littoral cell.

Validation-period performance metrics for all 839 transects are shown in Fig. 5e, with littoral cell-scale medians of $RMSE = 14.8$ m (IQR: 13.2-21.8 m), $Corr = 0.54$ (IQR: 0.32-0.63), and $\lambda = 0.45$ (IQR: 0.26-0.55; Refer to Fig. 1c), reflecting a fair-to-moderate hindcast accuracy throughout this littoral cell. Performance metrics decline toward the northern extremity of this littoral cell (Refer to Fig. 5e and Fig. 5a-c), near the unjettied Willapa Bay entrance, consistent with the pattern of reduced accuracy near estuarine entrances noted at the PNW scale. Component-specific performance follows a pattern distinct from Sand Lake, where the alongshore component, which dominates variability in this littoral cell, plays a larger role in overall accuracy (Refer to SI Fig. S3 for component-level metrics). Additionally, Long Beach exhibits among the strongest interdecadal trends of any PNW littoral cell, with pronounced erosion in the short southern segment between the Columbia River entrance and North Head, contrasting with strong accretion from North Head northward to Willapa Bay entrance (Refer to Fig. 5a-b and SI Fig. S2). These opposing trends, well captured by the model, highlight the importance of the Y_R component in this littoral cell (Refer to SI Fig. S2e and m). Performance during validation is roughly consistent with calibration across most transects, as confirmed by the tight clustering in the normalized Taylor diagram (Fig. 5f), mainly with the exception of transects near the Willapa Bay entrance.

As in Sand Lake, the normalized kernel shapes across transects in Long Beach (Fig. 5d) exhibit within-cell consistency; their physical interpretation is examined in the Morphodynamic Memory subsection below. Hindcast performance for all remaining littoral cells in the PNW is presented in SI Figs. S8-S27.

To evaluate the reliability of our uncertainty quantification, we compute the empirical percentage of the observed shoreline positions falling within the 95% C.I. (hereafter, within-C.I. percentage) for each component and for total shoreline positions across all littoral cells (SI Fig. S4). Among individual components, the cross-shore seasonal (CS) and alongshore (Al) components yield median empirical within-C.I. percentages of approximately 93-96%, closely tracking the nominal 95% target and indicating well-calibrated uncertainty bands across the PNW. The cross-shore interannual (CI) component consistently approaches 100%, reflecting the conservative capping applied to this low-frequency signal (Refer to Materials and Methods). Notably, in Long Beach littoral cell, where the alongshore component dominates shoreline variability, its within-C.I. percentage remains close to 95%, demonstrating well-calibrated bands even for the component carrying the most variance. A comparison with Monte Carlo (MC) parameter perturbation at four example transects across the PNW (SI Fig. S5) further underscores the advantage of the AR approach. While

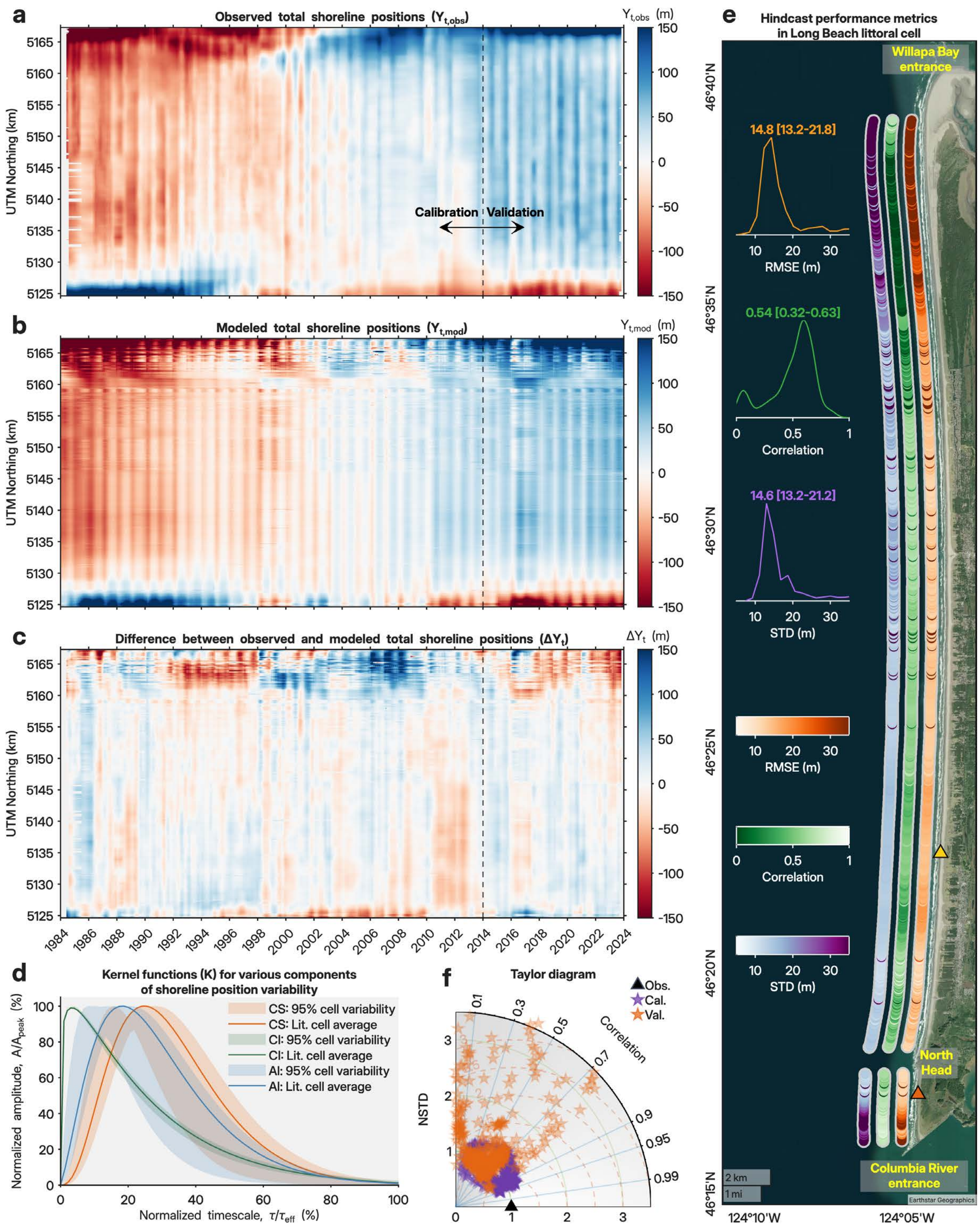

Fig. 5. Hindcast performance of the historical (observed) shoreline positions throughout Long Beach littoral cell, Washington. Spatiotemporal representation (heatmap; y-axis denotes the UTM northing and x-axis specifies time) of the total **(a)** observed ($Y_{t,obs}$) and **(b)** modeled (hindcast) ($Y_{t,mod}$) shoreline positions, alongside **(c)** their difference ($\Delta Y_t = Y_{t,obs} - Y_{t,mod}$). The dashed vertical line separates the calibration (1984–2014) and validation (2014–2024) periods. **(d)** The normalized (adjusted for amplitude [A] and effective morphodynamic memory [τ_{eff}]) shapes of the convolution kernel functions (K) optimized for all transects across this littoral cell, colored by component (orange: CS, green: CI, blue: Al), with solid lines representing the littoral cell average and shading denoting the 95% within-littoral cell variability across transects. **(e)** Spatial (alongshore) variability of the Root Mean Square Error ($RMSE$), Pearson correlation coefficient ($Corr$), and standard deviation (STD) of the modeled total shoreline positions during the validation period (2014-2024) in this littoral cell. This panel also features the kernel density estimation (KDE) for each metric across all transects within this littoral cell, alongside their littoral cell-median values and inter-quartile ranges (IQRs) shown above each KDE (the y-axis is not scaled). The locations of the example transects detailed in SI Fig. S2 are indicated by the orange and yellow triangles in this panel. Refer to Fig. 1 for the location of this littoral cell on the Washington coast. **(f)** The normalized (for standard deviation [$NSTD$] and Root Mean Square Error [$NRMSE$]) Taylor diagrams for the total shoreline position variability of all transects in this littoral cell, during both calibration and validation periods, where each point corresponds to an individual transect. Credit: basemaps, Earthstar Geographics (via MATLAB (68)).

both methods yield comparable coverage for the cross-shore seasonal component, MC produces substantially lower coverage for the cross-shore interannual component (as low as 3% and 7% during validation), where uncertainty sources beyond parameter values are most consequential, particularly for a component that accounts for approximately 70% of cross-shore shoreline variability across the PNW (56). For the alongshore component, MC exhibits inconsistent behavior—producing unrealistically wide bands in some cases and underestimating uncertainty in others—while AR provides consistently calibrated bounds across all components and transects. This confirms that parameter perturbation alone captures only a fraction of the aggregate data+model uncertainty, whereas the AR residual-based approach aims to implicitly account for all interacting sources. At the PNW scale, the within-C.I. percentage for total shoreline positions is approximately 98% and 99% during calibration and validation, respectively, satisfying our intended conservatism above the nominal 95% target. This conservatism stems primarily from the low-frequency components (Y_{CI}, Y_{RSLR}, and Y_R), where uncertainty is harder to constrain, while the higher-frequency components (cross-shore seasonal and alongshore), which carry the most management-relevant variability at seasonal-to-interannual time scales, remain well-calibrated near the nominal 95%.

Morphodynamic memory across the PNW. Beyond hindcast performance, the optimized kernel functions (K; Refer to Fig. 3g, j, and m) provide a physically interpretable window into how the PNW coast responds to hydrodynamic forcings, here presented in the form of various forcing functions (F). We characterize each kernel by three properties: (1) the peak response time (τ_{peak}), representing how quickly the shoreline reaches its maximum response to a particular forcing event or period; (2) the effective morphodynamic memory (τ_{eff}), defined as the time at which the kernel amplitude decays to 1% of its peak value, representing the total duration over which a forcing event appreciably influences shoreline positions; and (3) the kernel amplitude ($|A|$), representing the strength of the shoreline response to a particular forcing (Refer to Materials and Methods for details on the adopted kernel functional form, the definition of component-specific kernels, and the optimization of their parameters). Analyzing the spatial variability of these properties across all 22 littoral cells reveals systematic patterns that demonstrate the interplay between the PNW's geomorphic setting, geographic position, and hydrodynamic forcing regime.

How fast does the coast respond? The peak response time (τ_{peak}; Fig. 6b-d) varies structurally across components; the cross-shore seasonal component responds on the order of ~3-4.5 months, the cross-shore interannual component on the order of ~0.75-2.5 months, and the alongshore component on the order of ~12-30 months (Refer to SI for further details on the characteristics of these time scales). For the cross-shore seasonal component, τ_{peak} shows fair correlations with latitude ($R^2 = 0.10$, $p = 0.152$) and coastal orientation ($R^2 = 0.11$, $p = 0.134$; Fig. 6e-f), suggesting a possible but statistically inconclusive spatial dependence. The cross-shore interannual component shows a similar correlation with orientation ($R^2 = 0.12$, $p = 0.110$; Fig. 6h) but negligible dependence on latitude ($R^2 = 0.02$, $p = 0.572$; Fig. 6g). In both cases, the lack of statistical significance indicates that cross-shore peak response times are relatively stable across the PNW. In contrast, the alongshore component exhibits a strong latitudinal correlation ($R^2 = 0.50$, $p < 0.05$; Fig. 6i), meaning the northern PNW littoral cells take considerably longer to reach their peak shoreline response to alongshore forcing than their southern counterparts.

For how long does the coast remember? The effective morphodynamic memory (τ_{eff}; SI Fig. S6) reveals a complementary spatial structure. For the cross-shore seasonal component, τ_{eff} is stable across the PNW (~13-17 months), with no significant latitude or orientation dependence (SI Fig. S6e-f), indicating a relatively spatially uniform seasonal recovery timescale (Refer to SI for further details on the characteristics of these time scales). The cross-shore interannual component, however, shows a moderate-to-strong dependence between τ_{eff} and coastal orientation ($R^2 = 0.25$, $p < 0.05$; SI Fig. S6h), translating to shorter interannual memory for more west-facing, open coastlines. The alongshore component, similar to τ_{peak}, exhibits the strongest spatial signal, with τ_{eff} increasing significantly, and showing a strong correlation with latitude ($R^2 = 0.41$, $p < 0.05$; SI Fig. S6i), ranging from approximately 80 months in southern Oregon to over 140 months in northern Washington. Together with the τ_{peak} results, this indicates that northern littoral cells respond more slowly to alongshore forcing and retain the imprint of that forcing for longer.

How strongly does the coast respond? The kernel amplitude ($|A|$; SI Fig. S7) shifts the focus from temporal characteristics to the intensity of the shoreline response to each forcing signal. The cross-shore seasonal amplitude increases significantly with coastal orientation ($R^2 = 0.33$, $p < 0.05$; SI Fig. S7f), indicating that more west-facing coastlines respond more strongly to seasonal wave forcing. The cross-shore interannual amplitude correlates moderately-to-strongly with latitude ($R^2 = 0.32$, $p < 0.05$; SI Fig. S7g), indicating that northern littoral cells are more sensitive to interannual hydrodynamic forcing variability. The alongshore amplitude shows no significant spatial trends, indicating that the strength of the alongshore response is likely governed more by local geomorphic conditions (e.g., littoral cell length and sediment supply) than by regional-scale gradients.

These findings reveal a distinct spatial pattern in the PNW's morphodynamic memory. The alongshore component is primarily influenced by latitude, with both the timing and duration of coastal memory increasing northward, while interannual response intensity also strengthens with latitude. Coastal orientation, in turn, affects seasonal response intensity and modulates interannual memory duration. Alongside the systematic between-cell variability, kernel shapes are highly consistent within individual littoral cells, as demonstrated by the tight 95% variability bands in Figs. 4d and 5d (also refer to SI Figs. S8-27). This within-littoral cell coherence further supports the physical interpretability of the optimized kernels, as neighboring transects, sharing similar forcing and geomorphic conditions, yield consistent response functions rather than erratic, physically implausible shapes.

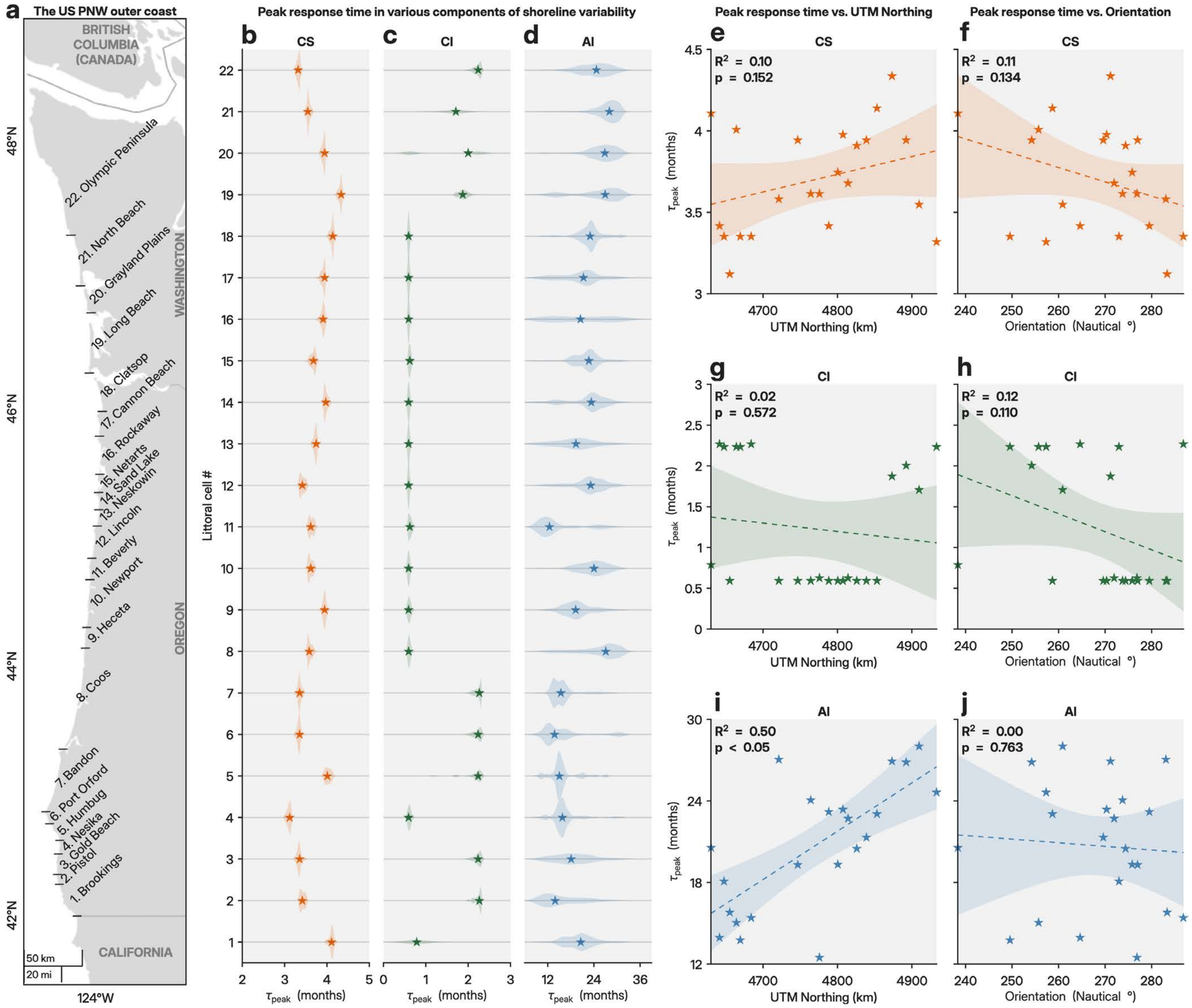

Fig. 6. Variability of peak response time (τ_{peak}) in the optimized kernel functions (K) across the 22 analyzed littoral cells in the PNW. (a) Map of the U.S. Pacific Northwest (PNW) outer coast showing the locations and boundaries of all 22 analyzed littoral cells. **(b–d)** Violin plots depicting the within-littoral cell distribution of τ_{peak} (in months) for the cross-shore seasonal (CS; orange), cross-shore interannual (CI; green), and alongshore (Al; blue) components, respectively. Stars denote littoral cell-median values. **(e–j)** Littoral cell-median τ_{peak} linearly regressed against littoral cell-average UTM Northing (left column; in km) and seaward, shore-normal orientation (right column; in nautical degrees) for each component (denoted at the top-right of each panel), with the coefficient of determination (R^2) and its corresponding p-value (with a significance level of $\alpha = 0.05$) reported. Dashed lines indicate the best-fit regression, with shading representing the 95% confidence interval (C.I.) of the linear fit. Refer to SI Figs. S6 and S7 for equivalent variability analyses on the effective morphodynamic memory (τ_{eff}) and kernel amplitude ($|A|$), respectively. Credit: basemaps, Natural Earth (via MATLAB (68)).

Discussion

Performance of the convolutional framework in a broader context. Implementing shoreline change models across large spatiotemporal scales, while accounting for various patterns of shoreline variability at seasonal-to-interdecadal scales, remains rare. CoSMoS-COAST represents the primary benchmark, with regional applications to California (32, 33), the U.S. South Atlantic Coast (18), and O'ahu (Hawai'i) (72). Its initial application to some extents of the PNW beaches yielded modest performance (66), primarily due to the framework's limited capacity to resolve the interannual cross-shore and alongshore variability that characterizes this region, partly motivating the development of our scale-adaptive approach. As detailed in SI Table S1, our framework achieves comparable hindcast skill (validation) across the PNW, performing on par with both CoSMoS-COAST's regional applications and most recent multi-model benchmarking studies (31, 37). The slightly higher median $RMSE$ (14.1 m vs. 12.4 m for California) reflects the PNW's greater shoreline variability (median observed $STD = 13.6$ m) and the more challenging coastal setting—characterized by high-energy wave conditions, mesotidal ranges, and predominantly low-sloping beaches compared to California (73)—rather than a deficiency in model skill. This is corroborated by the median Mielke's index of $\lambda = 0.51$, which closely matches California's index of agreement (d = 0.55; (33, 74)). The $RMSE$ is also comparable in magnitude to the median observed shoreline variability (STD = 13.6 m), as well as being below the estimated satellite-derived shoreline uncertainty for the region (~16.7 m; (56)) and the Landsat pixel resolution (15 m pan-sharpened), indicating that the model approaches the observational noise floor.

Our framework's EOF-based component targeting distinguishes it from approaches that model total shoreline position and subsequently decompose the output (75). Alternative decomposition strategies, such as Complete Ensemble Empirical Mode Decomposition (CEEMD; (76)) and Discrete Wavelet Transform (DWT; (77)), also separate signals prior to modeling, but our EOF-based approach exploits the orthogonality of its modes to ensure uncorrelated components and minimize error propagation during calibration. This EOF-based approach is particularly effective for the PNW, where cross-shore and alongshore variability modes are geomorphically distinct (5, 61, 65), well-separated by EOF analysis (56), and driven by different physical forcings.

Hindcast skill varies predictably across different components in our framework. The cross-shore seasonal signal (Y_{CS}), with its high frequency and many observable cycles, is consistently well-reproduced (SI Fig. S3b,f). This component sufficiently captures the shoreline response to sustained, regionally coherent elevated forcing episodes lasting several months, particularly El Niño fall-winter seasons (56, 69, 78), e.g., 1997-98 and 2015-16 (Refer to Fig. 2), with the latter notably falling within the validation period. Individual storm events, which operate at shorter time scales (e.g., several days) than our framework targets, are not specifically resolved, nor are they the primary driver of seasonal-to-interdecadal shoreline variability in the PNW. Interannual components (Y_{CI}, Y_{Al}) are inherently more difficult, where fewer effective cycles constrain calibration, and phase misalignment during the 10-year validation window can depress $Corr$ despite reasonable $RMSE$ values. Two mechanisms mitigate this at the total shoreline level. First, in many instances, errors in Y_{CI} and Y_{Al} partially offset when superimposed, yielding total $RMSE$ and Mielke's index values that improve upon those of individual interannual components across most littoral cells (compare SI Fig. S3a with S3c-d). Second, in littoral cells with strong interdecadal trends, such as Long Beach (littoral cell #19), Y_R dominates total variability, and the model's ability to capture this dominant signal sustains overall hindcast accuracy even where interannual components underperform. Notably, Long Beach achieves total performance comparable to other well-performing littoral cells despite exhibiting among the highest shoreline variability in the PNW (Refer to Fig. 5, SI Figs. S2, and S3a,e).

Spatial and component-level limitations in hindcast performance. The most prominent spatial limitation in hindcast performance is the recurrent decline in accuracy near estuarine entrances throughout the PNW (Figs. 1b, 2, and SI Figs. S8-S27). These locations—the Columbia River (whose sediment supply has substantially diminished over the past century due to damming (59)), Willapa Bay, and Grays Harbor entrances within the CRLC (55, 61), as well as several other estuarine entrances along the Oregon coast—involve sediment exchange processes including ebb-tidal delta dynamics, relatively minor fluvial sediment sources and sinks, and estuarine circulation. These processes operate at spatial and temporal scales not captured by our regional-scale forcing functions. This is consistent with the recognized limitations of equilibrium-based approaches in settings where underlying geology and sediment supply exert dominant control on shoreline behavior (44–46). The southern extremity of Grayland Plains littoral cell (SI Fig. S25), adjacent to Willapa Bay, exemplifies this challenge, with contemporary erosion rates of up to 20 m/year (55) driven by processes that our framework's linear residual trend (Y_R) cannot fully represent. The spatial coherence of these residual patterns near known areas of anomalous geomorphology with sediment sources and sinks suggests that the difference between modeled and observed shoreline positions (Refer to Figs. 4c, 5c, and SI Figs. S8-S27) could potentially serve as a proxy for unresolved sediment budget contributions; however, validating this interpretation would require independent geomorphologic data and modeling beyond the spatiotemporal scope of this study.

Component-specific challenges further reveal the model's limitations. The cross-shore interannual component (Y_{CI}) is most affected by equifinality, where its low-frequency nature provides far fewer independent cycles to constrain the optimization compared to the seasonal component, rendering it more susceptible to non-unique parameter solutions, while phase misalignment during the relatively short validation window further depresses correlation despite reasonable $RMSE$ values, as mentioned above. The alongshore component (Y_{Al}) faces a distinct challenge. Its forcing function is highly sensitive to its optimizable parameters, as evidenced by the unrealistically wide uncertainty bands produced by Monte Carlo (MC) parameter perturbation at four example transects (SI Fig. S5). Wave direction uncertainty in the hindcast forcing product (79, 80) compounds this sensitivity further. For both components, increasing the number of initial optimization seeds and optimization cycles could improve convergence, though the fundamental sensitivity of longshore transport formulations to the relative wave angle (61, 81) remains a structural limitation. The simplified Bruun rule used for the relative sea level rise-induced trend (Y_{RSLR}) also carries well-documented limitations in translating relative sea level rise into shoreline change (82–84). While its impact is likely modest over the 40-year hindcast period compared to other error sources, it could become increasingly consequential for longer-term projections. Satellite data temporal resolution is lower pre-1999, when observations relied solely on Landsat 5 mission (85), contributing to apparent mismatches in the early portion of the record. These data-related limitations are discussed further in the Limitations subsection.

Morphodynamic memory and its spatial controls across the PNW. The two-parameter Gamma-shaped kernel adopted in our framework, unlike the single-parameter, exponential kernel used in prior convolutional models (e.g., ref. (51)), can represent a delayed peak response, capturing the lag between hydrodynamic forcing and maximum shoreline response. This additional flexibility provides a more sophisticated representation of morphodynamic memory and enables the systematic analysis of peak response time (τ_{peak}), effective morphodynamic memory (τ_{eff}), and kernel amplitude ($|A|$)

across all 22 littoral cells, revealing spatial patterns that align with known geomorphic and hydrodynamic gradients of the PNW (86–88). Latitude exerts the strongest control on alongshore memory, where both τ_{peak} ($R^2 = 0.50$) and τ_{eff} ($R^2 = 0.41$) increase northward, consistent with the northward increase in littoral cell length. Coastal orientation controls cross-shore response intensity, with more west-facing coastlines responding more strongly to seasonal forcing ($|A_{CS}|$, $R^2 = 0.33$), potentially indicating greater exposure to north Pacific swell and, thus, the resulting stronger morphological response (Refer to, e.g., ref. (73)). Orientation also modulates interannual memory duration ($\tau_{eff,CI}$, $R^2 = 0.25$), with more exposed coastlines exhibiting shorter interannual memory. Interannual response intensity ($|A_{CI}|$, $R^2 = 0.32$) increases with latitude, indicating greater sensitivity of northern littoral cells to interannual hydrodynamic variability.

These latitude- and orientation-dependent patterns are corroborated by two complementary lines of recent evidence. Taherkhani et al. (2026) (56), using UMAP-based classification (89) of seasonal-to-interannual teleconnection metrics between ENSO/PDO, wave and water level forcing, and shoreline variability EOF modes, found that a littoral cell's geographical latitude and planform orientation influence how it experiences these climate-shoreline teleconnections. Our kernel analysis confirms this from an independent, model-based perspective. Beyond the PNW, Castelle et al. (2024) (90) reported analogous patterns along the Atlantic coast of Europe, where west-facing open coastlines showed stronger and more alongshore-uniform correlations with dominant winter climate indices, comparable to central-northern littoral cells in the PNW, while embayed and sheltered coastlines exhibited weaker and more spatially variable responses. The convergence of these findings across two ocean basins suggests that latitude- and orientation-dependent morphodynamic memory may be a general characteristic of open, wave-dominated coastlines exposed to large-scale climate variability.

Future directions. As demonstrated throughout this work, the shape of the kernels plays a central role in determining the framework's capacity to represent morphodynamic memory across different components and timescales. This underscores that future convolution-related efforts to further bridge reduced-complexity and AI-based approaches in shoreline modeling, potentially covering spatiotemporal scales beyond those addressed here, could benefit from exploring more advanced and flexible kernel formulations. When recast as an ordinary differential equation (Refer to SI), our framework shares mathematical structure with structured State-Space Models (SSMs) (91), indicating that a recently developed DL architecture such as Mamba (92), which uses SSM layers as convolution-like filters, may be naturally well-suited for this purpose. Notably, Mamba can dynamically adapt its kernel shape in a context-dependent manner throughout a sequence (e.g., time series), a capability that could address the need for resolving additional timescales, such as individual short-term (days-long) storm events, and processes, such as estuarine sediment exchange and ebb-tidal delta dynamics, that remain unresolved in our current framework.

Once calibrated, our model's computational efficiency makes it well-suited for stochastic projections of future shoreline positions under a broad range of climate scenarios (93–95). The model accommodates future changes in hydrodynamic forcing, including storminess and interannual water level variability, which are highly modulated by ENSO and PDO (56, 69, 96). If the characteristics of these climate modes alter under climate change (Refer to, e.g., refs. (95, 97–99)), the resulting changes in wave climate and water levels propagate naturally through the forcing functions into the shoreline projections. Changes in interdecadal relative sea level rise are similarly accommodated, subject to the Bruun rule limitations noted earlier. However, because the kernels are calibrated on 1984-2024 conditions, extrapolation to substantially different climate regimes and several-decade time scales requires caution (Refer to, e.g., ref. (35)). The framework's probabilistic outputs, including the empirically substantiated 95% uncertainty bands (covering "epistemic" uncertainty) produced for each component and total shoreline position, alongside physically interpretable kernel properties, offer advantages over black-box models for better communicating coastal hazards to stakeholders and decision-makers (43, 100, 101). This aligns with recent calls to distinguish event-scale dynamics from long-term trends and translate multi-temporal shoreline metrics into place-based risk insights (102, 103).

Materials and Methods

We used MATLAB (68) and its related auxiliary toolboxes (104–108) to perform our analyses and optimizations, and plot figures in this study. For brevity, we provide the key relevant information on (1) spatial coverage and discretization of the PNW outer coast, (2) historical wave, water level, and shoreline data, and (3) determining the dominant EOF modes of historical shoreline variability in SI. For further details, refer to Taherkhani et al. (2026) (56). Fig. 7 provides an overview of the modeling framework, summarizing the input data sources, convolutional procedure, optimization process, and final outputs.

The origins of convolution in the context of shoreline change modeling. The premise of applying convolution to coastal change studies was first laid out analytically by Kriebel and Dean (1993) (50). This concept was predicated on the assumption that beaches subjected to steady-state forcing conditions evolve toward a stable or equilibrium state in an approximately exponential manner, manifesting in the form of a convolution integral (47):

$$Y(t) = Y_0 e^{-k^{-1}t} + k \int_0^t e^{-k(t-\tau)} Y_{\mathrm{eq}}(\tau)\, d\tau, \qquad [1]$$

where Y, Y_{eq}, Y_0, and τ represent the instantaneous, equilibrium, and initial shoreline positions and the characteristic time scale (time lag), respectively, and k is a constant. Miller and Dean (2004) (47) subsequently revisited this concept and proposed a numerical approach to the application of convolution in shoreline evolution. Vitousek et al. (2025) (51) recently re-evaluated the characteristics of two well-known, equilibrium-based shoreline change models, namely Yates et al. (2009) (48) and Davidson et al. (2013) (49), by building on the concept of equilibrium (47, 109). They demonstrated that these equilibrium models are numerically equivalent to a convolutional framework, in which an exponential memory window ("filter" or "weighting function" or "kernel" [i.e., $\exp(-k(t-\tau))$]) is convolved with a forcing function (f), e.g., a seasonal significant wave height anomaly term:

$$Y(t) = Y_0 e^{-kt} + \int_0^t e^{-k(t-\tau)} f(\tau)\, d\tau. \qquad [2]$$

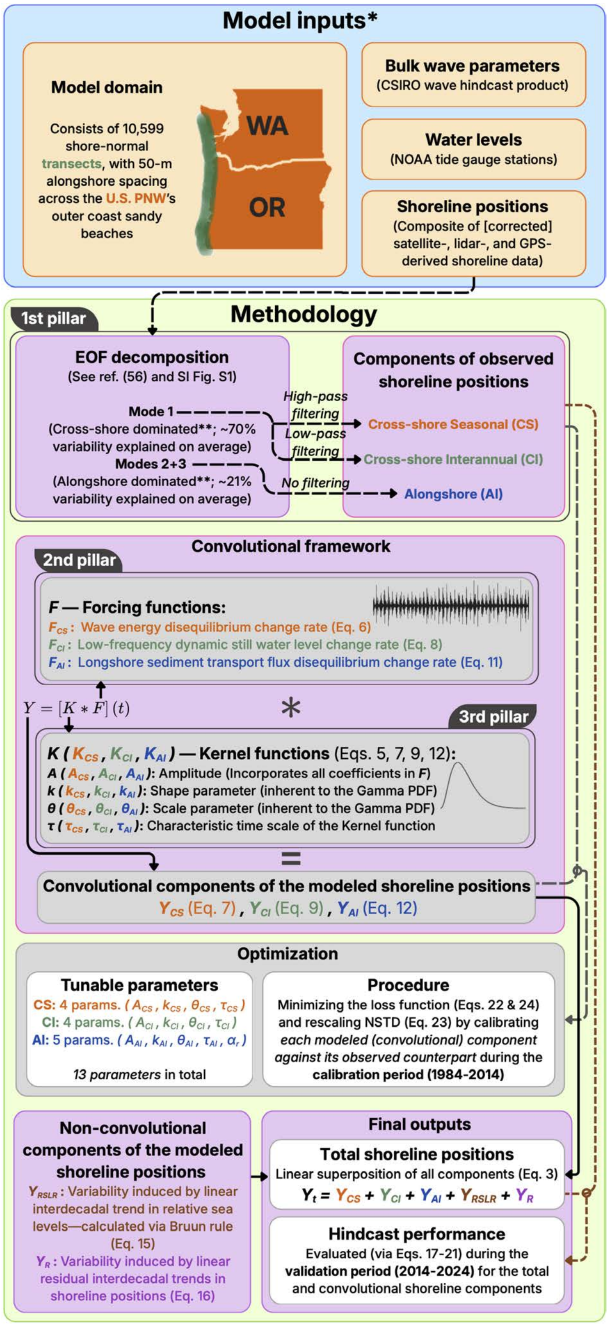

Fig. 7. Flowchart of the modeling framework, illustrating model inputs, methodology, and outputs. The framework relies on three pillars: (1) decomposition of the observed (historical) shoreline positions into cross-shore seasonal (CS), cross-shore interannual (CI), and alongshore (Al) components via Empirical Orthogonal Function (EOF) analysis and frequency filtering; (2) definition of component-specific forcing functions (F) derived from wave parameters and water levels; and (3) specification of Gamma-distribution-shaped kernel functions (K), whose parameters are optimized to reproduce observed shoreline variability (Y) via convolution ($Y = [K * F](t)$). *Refer to ref. (56) and SI for further details on the input data, including spatial discretization (transects) of the outer coast and historical wave, water level, and shoreline position data. **Long Beach is the only littoral cell among the 22 analyzed where the alongshore component dominates, with EOF mode 1 representing primarily alongshore variability (which, combined with mode 3, accounts for ∼62% of variability), while mode 2 mainly captures cross-shore variability (∼23% of variability). Refer to SI Fig. S1 for the spatiotemporal visualization of the top three EOF modes across all 22 analyzed littoral cells.

Here, k is a damping coefficient associated with seasonal cross-shore change in shorelines. Parallels are evident in these convolutional frameworks, as the analytical form proposed by Kriebel and Dean (1993) (50) appears closely identical to the numerical form derived by Vitousek et al. (2025) (51), with the sole exception of the change in the equilibrium forcing function, as demonstrated by Eqs. 1 and 2.

The PNW-tailored, scale-adaptive convolutional framework for shoreline change modeling. We propose a relatively simple, data-driven shoreline evolution model based on a convolutional framework, inspired by the convolution model introduced by Vitousek et al. (2025) (51). Our model is specifically designed to address real-world variability of historical shorelines across the sandy beaches of the PNW, building upon the findings of Taherkhani et al. (2026) (56). Their research explored various patterns (modes) of shoreline change occurring across different temporal scales throughout the PNW by analyzing 40 years (1984-2024) of composite satellite, lidar-, and GPS-derived shoreline positions, while also examining the primary drivers contributing to each mode of shoreline variability. Drawing on these insights, we developed our model around three fundamental pillars: (1) modes of historical shoreline variability, (2) the predominant forcing mechanisms driving each mode, and (3) the temporal scales over which each mode occurs. The first pillar ensures a representation of all dominant shoreline position change modes evident across the PNW, including both cross-shore and alongshore components. The second pillar addresses the external hydrodynamic forcings, i.e., wave components, water level variability, or combinations thereof, that effectively drive each mode of historical shoreline evolution. The third pillar captures the specific time scales over which each mode of historical shoreline variability manifests, effectively determining the time frame wherein the dominant hydrodynamic drivers exert maximum influence on the emergence of that particular mode.

The architecture of the convolutional framework. Taherkhani et al. (2026) (56) revealed that the cross-shore and alongshore components together, on average, account for over 90% of the variability in shoreline positions in nearly all 22 studied littoral cells across the PNW, based on an EOF analysis of detrended historical shoreline positions. More specifically, on average, the cross-shore component constitutes about 70% of the variability, while the alongshore component contributes around 21%. A clear interannual signal in the cross-shore component indicates that mode 1 from the EOF analysis is primarily responsible for the majority of interannual variability across nearly all littoral cells, except for Long Beach littoral cell. This finding underscores the importance of accurately hindcasting the interannual signal of the cross-shore component (Y_{CI}; where subscript "CI" denotes **C**ross-shore **I**nterannual), in addition to the sub-annual/seasonal cross-shore signal (Y_{CS}; where subscript "CS" denotes **C**ross-shore **S**easonal). Moreover, the alongshore component (Y_{Al}; where subscript "Al" denotes **Al**ongshore) in all examined littoral cells (except Long Beach) represents the second most dominant variability mode, effectively a superposition of modes 2 and 3 (modes 1 and 3 for Long Beach littoral cell) from the EOF analysis. Consequently, incorporating Y_{CS}, Y_{CI}, and Y_{Al} in our hindcasting framework has the potential to capture, on average, ∼91% of the variability in shoreline positions across the PNW. We address the long-term (interdecadal) trends in shoreline positions by accounting for gradual relative sea level rise (Y_{RSLR}; subscript "$RSLR$" denotes **R**elative **S**ea **L**evel **R**ise) and the slow effects of residual, unresolved processes (e.g., considerable sources and sinks of sediment) that cannot be modeled through a convolutional framework (Y_R; subscript "R" denotes **R**esidual). Ultimately, the final (**t**otal) shoreline position (Y_t) across the PNW, encompassing all its components at an arbitrary time t, can be represented as:

$$Y_t(t) = Y_{CS}(t) + Y_{CI}(t) + Y_{Al}(t) + Y_{SLR}(t) + Y_R(t). \qquad [3]$$

The first pillar involves decomposing total shoreline variability into its primary components. Each modeled component is then independently calibrated and validated against its observed (historical) counterpart.

In the convolutional framework we establish, we address the second and third pillars, which pertain to the hydrodynamic forcing and the associated morphodynamic timescales, respectively. We present our framework based on the convolutional foundation laid by Kriebel and Dean (1993) (50) and later expanded upon by Vitousek et al. (2025) (51), expressed as:

$$Y(t) = [K * F](t) = \int_{t_0}^{t} K(t-\tau)F(\tau)\,d\tau, \quad [4]$$

where K and F, respectively, denote our memory window (hereafter referred to as the kernel function) and the forcing function. These functions can be uniquely defined for each shoreline variability component (mode) presented. In theory, the mode-specific kernel function convolves with its corresponding forcing function (over a time scale τ) to reproduce the variability of that specific mode in the historical shorelines during the $t - t_0$ period. Essentially, the kernel function assigns a particular weight to antecedent external forcing conditions prior to an arbitrary time (i.e., $t - \tau$) to estimate the shoreline position associated with that specific mode at time t.

We adopt the functional form of a Gamma distribution as the kernel function in our convolutional framework, which has the following form:

$$K(x) = \frac{x^{k-1}e^{-\frac{x}{\theta}}}{\theta^k \Gamma(k)}. \quad [5]$$

In this kernel function, θ and k are the scale and shape parameters of the Gamma distribution, and $\Gamma(k)$ is the Gamma function, where for all positive integers of k, $\Gamma(k) = (k-1)!$. In our applications, the variable x of the kernel function is replaced by the effective time span by incorporating the characteristic time scale τ, i.e., $t - \tau$. Adopting this Gamma-shape form offers functions that are not provided by the exponential decay-like kernel function identified by Vitousek et al. (2025) (51). Most importantly, this kernel function is inherently a two-parameter function (i.e., θ and k), enhancing its versatility in the kernel's shape. It can be regarded as a generalization of the exponential decay-like PDF, which is fundamentally a one-parameter function, implying that a Gamma-shape kernel can accurately replicate a specific exponential decay-like kernel. This shape versatility becomes meaningful when modeling various modes of shoreline position variability. The kernel function facilitates the allocation of weights to antecedent forcing conditions, which, unlike an exponential decay-like kernel, may not necessarily emphasize the most recent conditions; in other words, it can incorporate a delay between specific hydrodynamic forcing and geomorphological response. Refer to SI for more details on the properties of the Gamma distribution kernel function. In the following subsections, we outline the forcing and kernel functions for each mode of shoreline variability presented in Eq. 3 individually. All forcing and kernel functions are constructed on a daily time step, thereby generating the corresponding shoreline position variability at the same temporal resolution.

Seasonal cross-shore component. A seasonal shoreline fluctuation is a prominent signal in the cross-shore component of shoreline variability (which accounts for ~70% of the total variability on average). Historically, reproducing this signal has been the primary objective of many shoreline change models, particularly equilibrium-based ones, which adhere to the principle that sandy beaches typically erode during large wave event seasons and subsequently recover during periods of smaller wave seasons (110). Recent studies focusing on the PNW have reported that the coastal dynamics in this region are predominantly wave-dominated (e.g., refs. (5, 61)). Driven by extratropical storms traversing the PNW, this region experiences one of the most energetic wave climates globally, with winter storms often generating very large deep-water wave heights exceeding 10 meters (e.g., ref. (111)). Taherkhani et al. (2026) (56) corroborate this finding, revealing that erosional shoreline position anomalies across the PNW are largely driven by a major increase in wave energy during those events. Building on these findings, as well as refs. (51, 109), we utilize the rate of change of wave energy anomaly (or disequilibrium) as the hydrodynamic forcing (F_{CS}) in our convolutional framework for modeling the seasonal cross-shore component of shorelines, represented as:

$$F_{CS}(t) = \frac{d}{dt}\frac{H_s^2(t) - \bar{H}_s^2}{\bar{H}_s^2}, \quad [6]$$

where $\bar{H}_s$ denotes the average (equilibrium) significant wave height (in meters) during 1984-2024. Subsequently, by following the convolutional framework delineated in Eqs. 4 and 5, the seasonal cross-shore component of shoreline variability (Y_{CS}) can be modeled as:

$$\begin{aligned} Y_{CS}(t) &= [K_{CS} * F_{CS}](t) \\ &= \int_0^t K_{CS}(t-\tau)F_{CS}(\tau)\,d\tau \\ &= \int_0^t \frac{-A_{CS}(t-\tau)^{k_{CS}-1}e^{-\frac{t-\tau}{\theta_{CS}}}}{\theta_{CS}^{k_{CS}}\Gamma(k_{CS})} \\ &\quad \times \frac{d}{d\tau}\frac{H_s^2(\tau) - \bar{H}_s^2(\tau)}{\bar{H}_s^2(\tau)}\,d\tau. \end{aligned} \quad [7]$$

Here, the variable A_{CS} represents the kernel's amplitude, essentially encompassing the product of all relevant coefficients and constants. The negative sign associated with A_{CS} highlights the inverse relationship between the wave-induced forcing and the shoreline position, indicating that an increase in F_{CS} corresponds to erosional behavior (i.e., shoreline recession). The kernel (K_{CS}) relies on four intrinsic parameters: A_{CS} (amplitude), k_{CS} (shape parameter), θ_{CS} (scale parameter), and τ_{CS} (the time-span over which K_{CS} applies). These parameters are optimized for individual transects by comparing and calibrating the modeled seasonal cross-shore component of the shorelines with its observed counterpart. The observed component is derived by applying a high-pass filter to mode 1 (mode 2 for Long Beach littoral cell) of the EOF analysis on detrended historical shorelines. This high-pass, 4th-order Butterworth filter, with a cutoff return period of 3 years, ensures that only close-to-annual signals are preserved in the observed data. We detail the specifics of optimizing these four parameters in the upcoming sections.

Using the time derivative of wave-induced forcing, rather than wave energy disequilibrium directly, is motivated by several physical considerations. Most notably, the derivative emphasizes rapid changes in wave energy (e.g., transient ramps and pulses) rather than absolute levels because rapid fluctuations are more effective at mobilizing sediment and driving shoreline response (e.g., refs. (112–114)). This formulation naturally suppresses constant or slowly varying anomalies that have little effect near equilibrium. The derivative also mitigates long-term drift and bias, keeping the model sensitive to the rate and timing of wave energy fluctuations rather than their absolute magnitude. Together, the derivative-based forcing and the kernel's transfer function yield a stable, lagged response consistent with the equilibrium-convolution framework. Refer to SI for additional details.

Interannual cross-shore component. We account for the influence of both waves and water levels when modeling the interannual variability of the cross-shore component in shoreline positions. Although the morphodynamics of PNW beaches are predominantly wave-dominated, water level variability plays an integral role in shaping the interannual variation of shorelines along the sandy beaches of the PNW (111, 115), as observed in other coastal settings (e.g., ref. (76, 116)). Almar et al. (2023) (117) and Taherkhani et al. (2026) (56), using different methodologies and water level datasets, demonstrated that interannual water level anomalies are a major contributor to interannual shoreline variability across the region. These variations can be substantial, particularly when large-scale climate patterns such as ENSO are at play. For example, during strong El Niño winters, monthly mean sea level anomalies can remain elevated for weeks to months, often adding tens of centimeters above typical tide levels. This increased background elevation, when combined with winter storm waves, substantially contributes to erosion and shoreline mobility

(88, 115–117). Moreover, waves can act as a secondary modifier in modulating seasonal-to-interannual water levels, with wave runup contributing notably to the variability of extreme Total Water Levels, that is, the superposition of Still Water Levels (SWLs; i.e., historical tide gauge data, which mainly consist of astronomical tides and non-tidal residuals (i.e., seasonal cycles, monthly mean sea level anomalies, and storm surge) and wave runup (88).

We define the forcing related to the interannual cross-shore component of shorelines by integrating SWLs and wave effects (specifically, wave setup while excluding wave swash to omit very high-frequency variability), referred to as Dynamic Still Water Levels (DSWLs). By applying a wave setup estimation for dissipative beaches (118) and considering the time rate of change in these hydrodynamic factors, we characterize the hydrodynamic forcing (F_{CI}) to be incorporated into the convolutional framework as follows:

$$\begin{aligned} F_{CI}(t) &= \frac{d}{dt}\Big(\eta_{DSWL}(t)\Big)_{LP} \\ &= \frac{d}{dt}\left(\eta_{SWL} + 0.016\sqrt{\frac{gH_0T_p^2}{2\pi}}\right)_{LP}. \end{aligned} \tag{8}$$

Here, g is the gravity constant ($9.81\ m\ s^{-2}$), H_0 and T_p, respectively, represent the deep-water significant wave height (in meters) and peak wave period (in seconds), and subscript LP signifies the application of a low-pass, 4th-order Butterworth filter with a cutoff return period of 3 years on the superposition of SWLs and the setup. This filtering ensures that only interannual modulations in these components are preserved, manifesting as interannual fluctuations in cross-shore shoreline positions, as hypothesized by previous scale-adaptive efforts in shoreline change modeling that shoreline variations at a specific temporal scale can be predicted via drivers exhibiting similar temporal fluctuations (76). Finally, we define our forcing term by taking the time derivative of this low-frequency superposition of SWLs and the setup for the reasons mentioned earlier. In alignment with the convolutional framework used for the seasonal cross-shore component (i.e., Eq. 7), the interannual cross-shore variability of shoreline positions (Y_{CI}) is modeled as:

$$\begin{aligned} Y_{CI}(t) &= [K_{CI} * F_{CI}](t) \\ &= \int_0^t K_{CI}(t-\tau)F_{CI}(\tau)\,d\tau \\ &= \int_0^t \frac{-A_{CI}(t-\tau)^{k_{CI}-1}e^{-\frac{t-\tau}{\theta_{CI}}}}{\theta_{CI}^{k_{CI}}\Gamma(k_{CI})} \\ &\quad \times \frac{d}{d\tau}\left(\eta_{SWL} + 0.016\sqrt{\frac{gH_0T_0^2}{2\pi}}\right)_{LP} d\tau. \end{aligned} \tag{9}$$

The additional variable A_{CI}, similar to its seasonal counterpart, denotes the amplitude of the kernel used here. For each transect, the four parameters inherent to the kernel (K_{CI}), namely, A_{CI} (amplitude), k_{CI} (shape parameter), θ_{CI} (scale parameter), and τ_{CI} (effective time span of K_{CI}), are optimized to best reproduce the observations. This is accomplished by calibrating the modeled interannual cross-shore component of shorelines against its observed counterpart, defined as the difference between mode 1 (mode 2 for Long Beach littoral cell) of the EOF analysis on detrended historical shorelines and its high-pass-filtered version, which isolates and removes the seasonal component of cross-shore shoreline variability. This approach ensures that only interannual-to-interdecadal signals are retained in the observed data.

Alongshore component. Alongshore variability in shoreline position, often attributed to gradients in longshore sediment transport, has been extensively investigated along the sandy beaches of the PNW. Several studies, e.g., refs. (5, 57, 65, 119), have aimed to monitor and model this geomorphological variability over limited segments of these beaches. Dominated by wave activity, particularly fluctuations in incident wave angles on seasonal to interannual scales, the alongshore migration of shorelines emerges as a key pattern in shoreline position variability across the PNW. Taherkhani et al. (2026) (56) found that, on average, alongshore shoreline migration accounts for approximately 21% of historical shoreline variability, representing the superposition of modes 2 and 3 (modes 1 and 3 for Long Beach littoral cell) derived from the EOF analysis of detrended historical shorelines during 1984–2024. This alongshore variability is especially pronounced along the Columbia River Littoral Cell (CRLC), encompassing Clatsop, Long Beach, Grayland Plains, and North Beach littoral cells (or sub-cells) in northern Oregon and southern Washington. Expanding on the findings of Anderson et al. (2018) (5) and Stevens et al. (2024) (61), Taherkhani et al. (2026) (56) observed a statistically significant influence of large-scale climate patterns in the Pacific Basin, namely, ENSO and PDO, on the interannual variability of alongshore shoreline migration across nearly all littoral cells in the PNW. Hence, incorporating this pattern of shoreline variability into our modeling framework is crucial.

Taherkhani et al. (2026) (56) revealed that in addition to the pronounced seasonal variability in incident wave angles, wave energy flux (WEF) exerts a statistically significant driving influence on the alongshore component of shoreline positions over interannual time scales. Thus, to establish our forcing function here, we adopt the Kamphuis formula (120) to quantify the longshore sediment transport flux (Q), expressed as:

$$Q = K_0 H_s^2\, T_p^{1.5}\, \sin^{0.6}(2\alpha), \tag{10}$$

where K_0 is a transect-specific constant, H_s denotes the near-breaking significant wave height, T_p represents the peak wave period, and α signifies the instantaneous relative angle between incoming waves and the shoreline orientation at a specific transect. The Kamphuis formula offers physical advantages over the commonly used CERC formula (121) by: (1) incorporating the modulation of the relative wave angle (α) effect through both significant wave heights (H_s) and peak wave periods (T_p), i.e., $Q \propto H_s^2\, T_p^{1.5}$, rather than relying solely on H_s as in the CERC formula ($Q \propto H_s^{2.5}$); and (2) being approximately proportional to the wave energy flux (i.e., $WEF \propto H_s^2\, T_p \implies WEF \underset{\sim}{\propto} Q$), which has been identified as a key driving factor in the interannual alongshore variability of shorelines, particularly near littoral cell boundaries.

Various aspects must be considered when determining the relative angle between instantaneous incident waves and shoreline orientation (i.e., α). First, at an arbitrary transect, if we estimate the shoreline angle (orientation) simply as the reference, static shoreline's angle (Refer to SI for details), it might not accurately represent the average shoreline angle at that transect during any given period, thereby introducing an inherent error. Moreover, the incident wave angles may contain errors as they are derived from a bulk wave hindcast product (79, 80). Additional errors could also be introduced through the wave propagation technique we have utilized. Accordingly, it is crucial to account for the accumulation of these potential errors in estimating the relative angle, particularly because one-line longshore transport models are known to be highly sensitive to even small shifts in relative wave angles (61, 81). To address this, we introduce a residual relative wave angle (α_r) that can be added to the initially estimated relative wave angle (α)—which is derived from the difference between the incident wave angles and the reference shoreline's angle—where Eq. 10 becomes $Q = K_0 H_s^2\, T_p^{1.5}\, \sin^{0.6}(2(\alpha + \alpha_r))$, with α_r as a variable that is optimized. Analogous to the seasonal and interannual components of the cross-shore shoreline positions, building on the insights of Turki et al. (2013) (122) and Jaramillo et al. (2021) (123), we describe the forcing associated with the alongshore shoreline variability (F_{Al}) as the change rate of the longshore sediment flux anomaly, given as:

$$F_{Al}(t) = \frac{d}{dt}\frac{Q(t) - \overline{Q}}{\overline{Q}}, \tag{11}$$

where $\bar{Q}$ denotes the average (equilibrium) alongshore sediment transport flux during 1984-2024. In line with the previously introduced convolutional frameworks (i.e., Eqs. 7 and 9), we model the alongshore variability in shoreline positions (Y_{Al}) as:

$$\begin{aligned} Y_{Al}(t) &= [K_{Al} * F_{Al}](t) \\ &= \int_0^t K_{Al}(t-\tau) F_{Al}(\tau)\, d\tau \\ &= \int_0^t \frac{-A_{Al}(t-\tau)^{k_{Al}-1} e^{-\frac{t-\tau}{\theta_{Al}}}}{\theta_{Al}^{k_{Al}} \Gamma(k_{Al})} \frac{d}{d\tau} \frac{Q(\tau)-\overline{Q}}{\overline{Q}}\, d\tau. \end{aligned} \quad [12]$$

In compliance with the procedure applied for Y_{CS} and Y_{CI}, the five parameters in Y_{Al}—comprising four inherent to the kernel (K_{Al}): A_{Al} (amplitude, absorbing the Kamphuis constant [K_0]), k_{Al} (shape parameter), θ_{Al} (scale parameter), and τ_{Al} (effective time-span of K_{Al}), and one parameter within the forcing function (i.e., α_r)—are optimized to ensure that the modeled alongshore component optimally aligns with its observed counterpart. This observed shoreline change signal reflects the superposition of modes 2 and 3 (modes 1 and 3 for Long Beach littoral cell) derived from the EOF analysis of the detrended historical shoreline positions. In the following sections, we detail the specifics related to the optimization of these five parameters pertinent to the alongshore variability of shoreline positions.

Interdecadal cross-shore component. Long-term (interannual-interdecadal) variations in hydrodynamic forcing, i.e., wave climate and sea level variability, are vital considerations when modeling shoreline evolution at interdecadal time scales (10-100 years). Yet, notable uncertainties emerge regarding future variability in wave climate within this region (93, 124). Also, it is well-established that waves largely influence Total Water Levels (TWLs), subsequently affecting sediment mobilization and shoreline evolution (60), although this impact predominantly manifests at shorter time scales (i.e., seasonal-interannual) rather than interannual-interdecadal periods, assuming no consistent increase/decrease in wave heights and peak wave periods. Nevertheless, the consistent yet consequential (125, 126) rise in sea levels directly affects shoreline positions, occurring over interdecadal time scales. The Bruun rule (127), which characterizes shoreline equilibrium shifts solely in response to long-term sea level variations, has been extensively used in modeling the influence of sea level rise on shoreline evolution. Despite its widespread use, it has been widely criticized for its simplifying assumptions, including a constant depth of closure and shore-parallel nearshore bathymetric contours, as well as its failure to account for wave climate changes and human interventions (82–84).

We model shoreline evolution on scales of decades to a century, driven by long-term relative sea level variability using the convolutional framework previously established for modeling other components of shoreline variability. Analogous to the interannual cross-shore component, we define the forcing (F_{RSLR}) driving interdecadal cross-shore shoreline variation as

$$F_{RSLR}(t) = \frac{d}{dt} \eta_{RSLR}(t). \quad [13]$$

The η_{RSLR} utilized here represents the interdecadal trend in historical SWL values (derived from tide gauge stations), calculated as the difference between unaltered and detrended SWLs. Notably, these SWLs effectively indicate the local relative sea level rise, representing a linear combination of vertical water motion rates influenced by factors such as glacier and ice cap melting, along with regional processes including variations in Earth's gravitational field and vertical land motion (VLM) (55, 60). The interdecadal cross-shore variation in shorelines (Y_{RSLR}) is modeled within the convolutional framework as follows:

$$\begin{aligned} Y_{RSLR}(t) &= [K_{RSLR} * F_{RSLR}](t) \\ &= \int_0^t K_{RSLR}(t-\tau) F_{RSLR}(\tau)\, d\tau. \end{aligned} \quad [14]$$

Nevertheless, recognizing the accelerating nature of sea level rise based on historical observations, it is conventional to approximate η_{RSLR} as a second-order polynomial trend (128) under the assumption of a constant acceleration rate over shorter periods (Refer to, e.g., ref. (129)). Given that premise, Eq. 7 can be refined to the extent (Refer to SI for details) that it analytically reproduces the Bruun rule, given as:

$$\begin{aligned} Y_{RSLR}(t) &= -C_{RSLR} \int_0^t \frac{d}{d\tau} \eta_{RSLR}(\tau)\, d\tau \\ &= -\frac{1}{\tan\beta} \eta_{RSLR}(t), \end{aligned} \quad [15]$$

where C_{RSLR} is a site-specific constant, incorporating the effect of the local shoreface slope ($\tan\beta$, i.e., the slope extending approximately from the average shoreline positions during 1984-2024 to the depth of closure on each transect). In favor of simplifying the optimization process for all components of shoreline variability and minimizing the complexity, we utilize the simplified Bruun rule, as illustrated in Eq. 15, to model the interdecadal, sea level rise-induced cross-shore shoreline variation across the PNW, given its satisfactory performance in previously developed hybrid shoreline evolution models for California (e.g., refs. (32, 33)) and the PNW (e.g., ref. (67)) applications. C_{RSLR} is assessed (outside of our optimization process) by integrating the effect of shoreface slopes ($\tan\beta$), allowing relative sea level trends (derived from tide gauge data) to be directly represented in the interdecadal movements of shoreline positions.

Residual trends. Given that our convolutional framework encompasses various components of shoreline variability across multiple temporal scales, it is essential to incorporate interannual-to-interdecadal trends in shoreline positions that cannot be explicitly estimated or modeled, primarily due to the complicated/unknown nature of the various physical mechanisms influencing these trends. Multiple factors, including fluvial- and/or shoreface-induced sediment sinks and sources, beach nourishment, aeolian sediment transport, bluff erosion, and headland sediment bypassing, can contribute to these residual trends (Refer to, e.g., refs. (32, 33)). Thus, we implicitly approximate this residual trend (Y_R), assuming a constant trajectory over a multi-decadal time frame. This is achieved by evaluating the difference between the multidecadal trend (spanning 40 years; 1984-2024) in the observed shoreline position ($Y_{obs,trend}$) and the relative sea level rise-induced shifts in the modeled shoreline position (Y_{RSLR}) time series at each transect, expressed as:

$$Y_R(t) = Y_{obs,trend}(t) - Y_{RSLR}(t). \quad [16]$$

Optimizing individual components of the modeled shoreline position variability. We optimize all 13 parameters introduced for the various components of shoreline variability (i.e., Y_{CS}, Y_{CI}, and Y_{Al}) across the PNW to calibrate our model against observations between 1984 and 2024. To this end, we individually calibrate each component by leveraging the prominent modes (patterns) of observed shoreline variability—which, on average, account for over 90% of the variability—obtained from the EOF analysis of historical shoreline positions (Refer to ref. (56)). This procedure ensures that all three pillars previously established for implementing our PNW-tailored shoreline change model are met.

Performance metrics and loss function. Following established methodologies from recent shoreline change modeling studies (e.g., refs. (31, 37, 75)), we evaluate our model's performance using four widely used statistical metrics: (1) Root Mean Square Error ($RMSE$), (2) Pearson correlation coefficient ($Corr$), (3) standard deviation (STD), and Mielke's index (λ) (130) between modeled and observed shoreline positions. The Root Mean Square Error ($RMSE$) is defined as:

$$\text{RMSE} = \sqrt{\frac{1}{n} \sum_{i=1}^{n} \left(y_i - \hat{y}_i\right)^2}, \quad [17]$$

the Pearson correlation coefficient ($Corr$) as:

$$\mathrm{Corr} = \frac{\sum_{i=1}^{n}\left(y_i - \bar{y}\right)\left(\hat{y}_i - \bar{\hat{y}}\right)}{\sqrt{\sum_{i=1}^{n}\left(y_i - \bar{y}\right)^2}\sqrt{\sum_{i=1}^{n}\left(\hat{y}_i - \bar{\hat{y}}\right)^2}}, \qquad [18]$$

the standard deviation (STD) as:

$$\mathrm{STD} = \sqrt{\frac{\sum_{i=1}^{n}\left(y_i - \bar{y}\right)^2}{n}}, \qquad [19]$$

and Mielke's index (λ) as:

$$\lambda = 1 - \frac{\frac{1}{n}\sum_{i=1}^{n}\left(y_i - \hat{y}_i\right)^2}{\mathrm{STD}(y)^2 + \mathrm{STD}(\hat{y})^2 + \left(\bar{y} - \bar{\hat{y}}\right)^2 + \kappa}, \qquad [20]$$

where

$$\kappa = \begin{cases} 0, & Corr \geq 0, \\ \frac{2}{n}\left|\sum_{i=1}^{n}\left(y_i - \bar{y}\right)\left(\hat{y}_i - \bar{\hat{y}}\right)\right|, & \text{otherwise.} \end{cases} \qquad [21]$$

In the above, n is the number of paired data points, y_i and $\hat{y}_i$ are the i-th observed and modeled shoreline positions, and $\bar{y}$ and $\bar{\hat{y}}$ are their respective means over the calibration or validation period. $\mathrm{STD}(y)$ and $\mathrm{STD}(\hat{y})$ denote the standard deviations of the observed and modeled time series, respectively. Mielke's index, similar to $Corr$, is dimensionless and ranges from 0 (no agreement) to 1 (perfect agreement) between the modeled and observed time series. This index provides a more comprehensive statistical framework that accounts for variance, bias, and correlation direction, making it potentially more informative. The first three metrics ($RMSE$, $Corr$, and STD) can be illustrated in a unified Taylor diagram (131), which provides a holistic visual representation of the model's performance at a specific transect (e.g., ref. (39)).

The optimization objective in our convolutional framework is to tune kernel functions (alongside the residual relative wave angle (α_r)) that ensure their unique shapes for each component of shoreline position variability, which, when convolved with the corresponding forcing function, accurately replicate the observed shoreline position. This essentially necessitates the optimization of the Pearson correlation coefficient ($Corr$) between the modeled and observed time series. Consequently, we first optimize the parameters (except for the amplitude, A) by formulating the Loss Function (L) so that its minimization ensures the maximization of $Corr$:

$$L = |1 - Corr|. \qquad [22]$$

Following that, we rescale the modeled time series by adjusting the amplitude (A) for each component of shoreline position variability. This is accomplished by equating the standard deviations of the modeled and observed shoreline positions, i.e., STD_{mod} and STD_{obs}, respectively, or simply:

$$NSTD = \frac{STD_{\mathrm{mod}}}{STD_{\mathrm{obs}}} \rightarrow 1, \qquad [23]$$

where $NSTD$ denotes the normalized standard deviation. No optimization is implemented here since A is derived via direct analytical computation.

To reliably gauge a model's true hindcasting and predictive capability, it is standard procedure to assess model performance on a separate (split), independent validation period instead of the calibration (training) period (e.g., ref. (132)). Nonetheless, the subjectivity inherent in these frameworks, such as the durations of the calibration and validation periods used, introduces a degree of uncertainty/subjectivity in the achieved performance metrics (133). Proposed splitting approaches range from calibrating on all available data (134) to using as few as 2–7 years for seasonal variability (77). To facilitate the comparison of our models' performance relative to others, we allocate the initial three-quarters of the 40-year historical data (1984-2014) for calibration and the subsequent quarter (2014-2024) for validation.

Optimization problem and algorithm. The optimization problem, which is to minimize our objective function, i.e., the Loss function (L), for individual components of modeled shoreline variability, is outlined as:

$$\begin{aligned} &\min_{\mathbf{p}\in\mathbb{R}^N} \quad L(\mathbf{p}) \\ &\text{subject to} \quad lb_i \leq p_i \leq ub_i, \quad i = 1, \ldots, N. \end{aligned} \qquad [24]$$

In this optimization problem, we optimize the vector of parameters ($\mathbf{p}$) within the convolutional framework (excluding the amplitude, A) for each component of shoreline variability. For example, in the case of the alongshore component (Y_{Al}, Eq. 12), we aim to optimize the four parameters (i.e., $N = 4$) in $\mathbf{p}$ ($\mathbf{p} = [k_{Al}, \theta_{Al}, \tau_{Al}, \alpha_r]$), with each parameter ($p_i$) constrained by a specific, user-defined lower bound (lb_i) and upper bound (ub_i) based on physical justifications.

The constrained optimization problem delineated in Eq. 24 is non-convex for several reasons, including (but not limited to): (1) the convolutional framework adopted, where non-polynomial and non-affine dependence on these parameters creates a mapping from parameters to model outputs, introduces a highly nonlinear relationship between the optimizable parameters and the modeled shoreline positions, and (2) due to these nonlinear interactions, the Loss function (L; Eq. 22) is anticipated to exhibit several local minima throughout its landscape. To alleviate this potential issue in our constrained optimization problem, we adopt the AdamW (135) optimization algorithm. This gradient-based algorithm (26), by incorporating enhancements to its predecessor, i.e., Adam (136), is presently an extensively used and reliable default option for training state-of-the-art deep neural networks across various domains. Some features, including improved weight decay implementation and momentum-based parameter updates, render this method efficient in convergence and stable during the optimization process. In our AdamW architecture, we use the following hyperparameters: learning rate of $\alpha = 0.001$, first-moment exponential decay rate of $\beta_1 = 0.9$, second-moment exponential decay rate of $\beta_2 = 0.999$, numerical stabilizer of $\epsilon = 10^{-8}$, and weight decay of $\lambda = 0.01$ with a maximum of 3000 optimization iterations (epochs). We additionally implement random seeding of initial parameters in our optimization process, meaning that for each parameter (p_i), we start the optimization with 10 random initial values between its user-defined lower bound (lb_i) and upper bound (ub_i). This reduces the likelihood of converging to unfavorable local minima of the Loss function (L) during the optimization of each modeled shoreline variability component for individual transects.

Uncertainty quantification. A fully propagated uncertainty analysis would require independent error estimates for satellite-derived shorelines, wave forcing, and water levels at every transect. Satellite-derived shoreline uncertainty (∼16.7 m) is quantified only at the small fraction of transects where lidar/GPS ground truth is available (∼1% of transects, concentrated in patches across central Oregon, northern Oregon, and southern Washington; refer to ref. (56) for details), and cannot be reliably generalized across all 10,599 transects spanning diverse littoral cells. Similarly, wave and water level forcing uncertainties have not been independently characterized for this region. We therefore adopt an indirect approach that aims to capture the combined effect of data and model (data+model) uncertainty without requiring explicit error estimates for each input source. To this end, we adopt Autoregressive (AR) modeling to characterize the temporal structure of hindcast residuals and generate probabilistic uncertainty bands. For each component $i \in \{CS, CI, Al\}$ at each transect, the residuals between observed and modeled shoreline positions are normalized by the calibration-period $RMSE$ as:

$$\epsilon_i(t) = \frac{y_i(t) - \hat{y}_i(t)}{\text{RMSE}_i}, \qquad [25]$$

where $y_i(t)$ and $\hat{y}_i(t)$ are the observed and modeled shoreline positions, respectively. An $AR(l)$ model is then fitted to the normalized residuals $\epsilon_i(t)$ as:

$$\epsilon_i(t) = \sum_{k=1}^{l} \phi_k \, \epsilon_i(t-k) + \eta(t), \qquad \eta(t) \sim \mathcal{N}(0, \sigma^2), \qquad [26]$$

where ϕ_k are the autoregressive coefficients, $\eta(t)$ is a random perturbation term, σ^2 is the variance of the random perturbation term estimated during the AR fitting procedure, and the model order l is selected by minimizing the Akaike Information Criterion (AIC), which penalizes model complexity. This step captures the temporal autocorrelation structure of the residuals, effectively distinguishing the approach from simply adding random perturbation (white noise) to the hindcast. An ensemble of 100 stochastic realizations is then generated by driving the fitted AR model with random white noise and rescaling by the calibration $RMSE$ via:

$$\hat{y}_i^{(b)}(t) = \hat{y}_i(t) + \text{RMSE}_i \cdot \tilde{\epsilon}_i^{(b)}(t), \qquad b = 1, \ldots, 100, \qquad [27]$$

where $\tilde{\epsilon}_i^{(b)}(t)$ is a synthetic residual time series produced by filtering independent $\mathcal{N}(0, \sigma^2)$ draws through the estimated AR coefficients. The 95% uncertainty bands are obtained as the 2.5th and 97.5th empirical percentiles across the ensemble:

$$\hat{y}_i^{2.5}(t) = P_{2.5}\left[\hat{y}_i^{(b)}(t)\right], \qquad \hat{y}_i^{97.5}(t) = P_{97.5}\left[\hat{y}_i^{(b)}(t)\right]. \qquad [28]$$

This procedure is applied independently to each component at each transect. The total shoreline position uncertainty is obtained by summing the component-level ensembles before extracting percentiles, thereby preserving inter-component interactions in the tails of the distribution. We also tested an Autoregressive Moving Average (ARMA) model with Bayesian Information Criterion (BIC)-based order selection, which produced negligible differences in the resulting uncertainty bands compared to AR (results not shown), supporting the use of the simpler AR formulation. For low-frequency components (e.g., cross-shore interannual), strong autocorrelation in the AR model can cause synthetic residuals to drift, producing unrealistically wide uncertainty bands. We therefore limit the ensemble perturbations to $\pm 2RMSE$, which is slightly more conservative than the $\pm 1.96RMSE$ expected for a 95% interval under the assumption of normality (i.e., the residuals being fairly normally distributed around zero). This ensures physically plausible bounds while preserving the temporal structure of the residuals. This empirical approach implicitly captures multiple interacting data+model (often termed epistemic) uncertainty sources, including forcing data errors, satellite-derived shoreline measurement uncertainty, unresolved physical processes, and parameter optimization limitations, without requiring their individual quantification (e.g., refs. (33, 137, 138)). Uncertainty bands for the relative sea level rise- and residual-induced trend components (Y_{RSLR} and Y_R) are estimated separately via block-bootstrapping (nine blocks of approximately equal length, with replacement) of the historical still water level and shoreline position time series, respectively.

Limitations. Our modeling effort faces multiple limitations, primarily associated with uncertainties in shoreline position data (1984-2024) used for calibration and validation of the hindcast shorelines. Landsat missions operate at relatively low resolution (30 m/pixel—15 m/pixel pan-sharpened), resulting in a positional $RMSE$ of ~16.7 m after corrections (for hydrodynamic contributions, outliers, and residual biases) (27, 126). This error margin, though satisfactory compared to other coastal regions (e.g., refs. (33, 139)), remains relatively high given the PNW's energetic wave climate and predominantly low-sloping beach morphology (140). Furthermore, the temporal resolution of the satellite-derived data diminishes pre-1999, when observations relied solely on Landsat 5. Also, the scarcity of datum-based shoreline positions (lidar- and GPS-derived data) limits most transects to merely 2-3 lidar data points, substantially reducing correction accuracy compared to the negligible fraction (~1%) of transects with several (≥10) datum-based shoreline position measurements (27, 28). As widely recognized, uncertainties in the data immediately translate into uncertainties and errors in the modeling results (e.g., refs. (28, 33, 37)). Thus, as a data-driven framework, our model can only achieve hindcasting accuracy commensurate with the quality of the observed data.

A related limitation is the propagation of errors among EOF modes of shoreline position variability. Because our modeled components rely on these modes, inaccuracies in the modes propagate directly into hindcast errors. This misplacement of variability from one EOF mode to others (known as "mode mixing") arises because real-world coastal processes interact nonlinearly, whereas EOF, as a purely statistical technique, enforces orthogonal decomposition that cannot fully represent these interactions (75, 141, 142). Although the orthogonality feature efficiently distinguishes between two well-documented modes of shoreline position variability (i.e., cross-shore and alongshore) across the PNW, it may inadequately capture the PNW's complex morphodynamics (e.g., ref. (54)), particularly when localized unresolved processes (e.g., sinks and sources of sediment) are in play. For simplicity and interpretability, we use only the top 3 EOF modes. While these modes account for the most (~91%) of variability in shorelines on average (Refer to ref. (56)), the omission of lower-ranked modes (which collectively account for ~9% of variability on average) introduces an additional source of error in our modeling results, potentially missing localized variability.

Our framework treats each component of shoreline position change independently, optimizing on a transect-by-transect basis without explicitly incorporating spatial proximity effects or conserving sediment mass. While this is a recognized trade-off in reduced-complexity shoreline modeling (13, 31), it means that processes such as alongshore sediment redistribution between adjacent transects are not explicitly resolved. We also acknowledge that representing a three-dimensional morphodynamic system through a single shoreline proxy (one-dimensional in space) limits the framework's ability to resolve cross-shore profile changes, as shoreline position is only loosely coupled to total sediment volume (143). However, these are shared limitations of most shoreline-focused reduced-complexity models and do not uniquely affect our framework.

Optimizing 13 parameters on a transect-by-transect basis introduces a substantial degree of equifinality, whereby different parameter sets produce nearly identical hindcast performance (144). This behavior is observed across repeated optimization runs (results not shown), and is particularly concerning for lower-frequency components (e.g., the cross-shore interannual mode), where limited effective cycles make it harder to distinguish between competing parameter sets. To account for the resulting parameter uncertainty, we use a conservative uncertainty quantification procedure (outlined in the Uncertainty quantification section). Equifinality further underscores the need for stochastic, ensemble approaches in long-term coastal morphodynamic projections (144).

Lastly, hydrodynamic datasets introduce uncertainty in both the forcing functions and the corrections applied to satellite-derived shoreline positions (Refer to ref. (56)). The CSIRO wave bulk parameter dataset (145, 146), as a hindcast product, contains inherent uncertainties from spatiotemporally sparse or error-prone buoy calibration data (79, 80). Also, the water level time series, despite retaining only stations with >90% data coverage during 1984-2024, required imputation of missing values using multi-year averages. This interpolation methodology introduces additional errors in the water level time series used across all transects, particularly since the source tide gauge stations (71, 147) are situated in geographically distant coastal environments, potentially failing to precisely capture localized hydrodynamic conditions.

These input uncertainties collectively propagate through the convolutional framework, affecting hindcast accuracy across the PNW.

ACKNOWLEDGMENTS. We thank Randall Pittman and the Coastal Imaging Laboratory (CIL) at Oregon State University for computational resources and technical assistance. Any use of trade, firm, or product names is for descriptive purposes only and does not imply endorsement by the U.S. Government.

DATA AVAILABILITY. Data and models, produced as part of this study, are available at: [https://oregonstate.box.com/s/hayy3n4mjbpoo7zl7picvhrc366ed6xn].

AUTHOR CONTRIBUTION. M.T. and S.V. developed the initial concept for this study. M.T. performed and verified the analysis and wrote the original manuscript. S.V. and P.R. contributed to the writing of the manuscript. P.R. secured the funding to support this research. All authors discussed the results and edited the manuscript.

FUNDING DECLARATION. We acknowledge funding that supported this research in part from the Cascadia Coastlines and Peoples Hazards Research Hub, an NSF Coastlines and People Large-Scale Hub (NSF award number 2103713). This work was also supported in part by sustained funding from the Northwest Association of Networked Ocean Observing Systems (NANOOS) on NOAA-IOOS Award NA21NOS0120093 and from NOAA via the NOS/NCCOS/CRP Effects of Sea-Level Rise (ESLR) Program (award number NA19NOS4780180).

COMPETING INTERESTS. The authors declare no competing interests.

1. EB Barbier, et al., The value of estuarine and coastal ecosystem services. *Ecol. monographs* **81**, 169–193 (2011).
2. MI Vousdoukas, et al., Sandy coastlines under threat of erosion. *Nat. climate change* **10**, 260–263 (2020).
3. JD Lopez-Rivas, JC Cardenas, What is the economic value of coastal and marine ecosystem services? a systematic literature review. *Mar. Policy* **161**, 106033 (2024).
4. N Elko, et al., The future of nearshore processes research. *Shore Beach* **83**, 13 (2015).
5. D Anderson, P Ruggiero, JA Antolínez, FJ Méndez, J Allan, A climate index optimized for longshore sediment transport reveals interannual and multidecadal littoral cell rotations. *J. Geophys. Res. Earth Surf.* **123**, 1958–1981 (2018).
6. RJ Nicholls, JR French, B van Maanen, Simulating decadal coastal morphodynamics. *Geomorphology* pp. 1–2 (2015).
7. GR Lesser, Jv Roelvink, JTM van Kester, G Stelling, Development and validation of a three-dimensional morphological model. *Coast. engineering* **51**, 883–915 (2004).
8. PD Komar, *Beach Processes and Sedimentation.* (Prentice-Hall), p. 429 (1977).
9. AS Farris, JW Long, EA Himmelstoss, Accuracy of shoreline forecasting using sparse data. *Ocean. & Coast. Manag.* **239**, 106621 (2023).
10. MB Gravens, NC Kraus, H Hanson, GENESIS: Generalized model for simulating shoreline change. Report 2: Workbook and system user's manual, (U.S. Army Engineer Waterways Experiment Station, Coastal Engineering Research Center), Technical Report CERC-89-19 (1991).
11. D Roelvink, et al., Modelling storm impacts on beaches, dunes and barrier islands. *Coast. engineering* **56**, 1133–1152 (2009).
12. DL Passeri, et al., The roles of storminess and sea level rise in decadal barrier island evolution. *Geophys. Res. Lett.* **47**, e2020GL089370 (2020).
13. E Hunt, et al., Shoreline modelling on timescales of days to decades. *Camb. Prisms: Coast. Futur.* **1**, e16 (2023).
14. CR Sherwood, et al., Modeling the morphodynamics of coastal responses to extreme events: What shape are we in? *Annu. review marine science* **14**, 457–492 (2022).
15. J Reyns, B Jagers, R Ranasinghe, H Kernkamp, D Roelvink, A three-dimensional process-based morphodynamic model on orthogonal unstructured grids for coastal applications. *Coast. Eng.* p. 104915 (2025).
16. J French, et al., Appropriate complexity for the prediction of coastal and estuarine geomorphic behaviour at decadal to centennial scales. *Geomorphology* **256**, 3–16 (2016).
17. M O'Shea, J Murphy, , et al., Developing a process driven morphological model for long term evolution of a dynamic coastal embayment. *Open J. Mar. Sci.* **10**, 93 (2020).
18. S Vitousek, et al., Scalable, data-assimilated models predict large-scale shoreline response to waves and sea-level rise. *Sci. Reports* **14**, 28029 (2024).
19. TW Hsu, SH Ou, SK Wang, On the prediction of beach changes by a new 2-d empirical eigenfunction model. *Coast. Eng.* **23**, 255–270 (1994).
20. HN Southgate, KM Wijnberg, M Larson, M Capobianco, H Jansen, Analysis of field data of coastal morphological evolution over yearly and decadal timescales. part 2: Non-linear techniques. *J. Coast. Res.* pp. 776–789 (2003).
21. RA Holman, AH Sallenger, TC Lippmann, JW Haines, The application of video image processing to the study of nearshore processes. *Oceanography* **6**, 78–85 (1993).
22. M Davidson, et al., The coastview project: Developing video-derived coastal state indicators in support of coastal zone management. *Coast. Eng.* **54**, 463–475 (2007).
23. A Luijendijk, et al., The state of the world's beaches. *Sci. reports* **8**, 1–11 (2018).
24. K Vos, KD Splinter, MD Harley, JA Simmons, IL Turner, Coastsat: A google earth engine-enabled python toolkit to extract shorelines from publicly available satellite imagery. *Environ. Model. & Softw.* **122**, 104528 (2019).
25. MD Harley, MA Kinsela, Coastsnap: A global citizen science program to monitor changing coastlines. *Cont. Shelf Res.* **245**, 104796 (2022).
26. Y LeCun, Y Bengio, G Hinton, Deep learning. *nature* **521**, 436–444 (2015).
27. IL Turner, MD Harley, R Almar, EW Bergsma, Satellite optical imagery in coastal engineering. *Coast. Eng.* **167**, 103919 (2021).
28. S Vitousek, et al., The future of coastal monitoring through satellite remote sensing. *Camb. Prisms: Coast. Futur.* **1**, e10 (2023).
29. JA Simmons, KD Splinter, Data-driven shoreline modelling at timescales of days to years. *Coast. Eng.* **197**, 104685 (2025).
30. JW Long, NG Plant, Extended kalman filter framework for forecasting shoreline evolution. *Geophys. Res. Lett.* **39** (2012).
31. J Montaño, et al., Blind testing of shoreline evolution models. *Sci. reports* **10**, 2137 (2020).
32. S Vitousek, PL Barnard, P Limber, L Erikson, B Cole, A model integrating longshore and cross-shore processes for predicting long-term shoreline response to climate change. *J. Geophys. Res. Earth Surf.* **122**, 782–806 (2017).
33. S Vitousek, K Vos, KD Splinter, L Erikson, PL Barnard, A model integrating satellite-derived shoreline observations for predicting fine-scale shoreline response to waves and sea-level rise across large coastal regions. *J. Geophys. Res. Earth Surf.* **128**, e2022JF006936 (2023).
34. M Davidson, E Hunt, N Valiente, A unified, data-informed model for shoreline evolution due to longshore and cross-shore processes. *J. Geophys. Res. Ocean.* **130**, e2025JC022379 (2025).
35. M Itzkin, LJ Moore, P Ruggiero, PA Hovenga, SD Hacker, Combining process-based and data-driven approaches to forecast beach and dune change. *Environ. Model. & Softw.* **153**, 105404 (2022).
36. K Calcraft, KD Splinter, JA Simmons, LA Marshall, Do lstm memory states reflect the relationships in reduced-complexity sandy shoreline models. *Environ. Model. & Softw.* **183**, 106236 (2025).
37. Y Mao, et al., Benchmarking shoreline prediction models over multi-decadal timescales. *Commun. Earth & Environ.* **6**, 581 (2025).
38. HT Thai, Machine learning for structural engineering: A state-of-the-art review in *Structures.* Vol. 38, pp. 448–491 (2022).
39. E Gomez-de la Peña, G Coco, C Whittaker, J Montaño, On the use of convolutional deep learning to predict shoreline change. *Earth Surf. Dyn.* **11**, 1145–1160 (2023).
40. S Adusumilli, et al., Predicting shoreline changes along the california coast using deep learning applied to satellite observations. *J. Geophys. Res. Mach. Learn. Comput.* **1**, e2024JH000172 (2024).
41. K Calcraft, JA Simmons, LA Marshall, KD Splinter, A generalized data-driven shoreline model at the regional scale. *J. Geophys. Res. Mach. Learn. Comput.* **3**, e2025JH000989 (2026).
42. C Rudin, et al., Interpretable machine learning: Fundamental principles and 10 grand challenges. *Stat. Surv.* **16**, 1–85 (2022).
43. JS Dramsch, et al., Explainability can foster trust in artificial intelligence in geoscience. *Nat. Geosci.* **18**, 112–114 (2025).
44. SR Riggs, WJ Cleary, SW Snyder, Influence of inherited geologic framework on barrier shoreface morphology and dynamics. *Mar. geology* **126**, 213–234 (1995).
45. LD Wright, *Morphodynamics of Inner Continental Shelves.* (CRC Press), p. 241 (1995).
46. JAG Cooper, AN Green, C Loureiro, Geological constraints on mesoscale coastal barrier behaviour. *Glob. Planet. Chang.* **168**, 15–34 (2018).
47. JK Miller, RG Dean, A simple new shoreline change model. *Coast. Eng.* **51**, 531–556 (2004).
48. ML Yates, R Guza, W O'reilly, Equilibrium shoreline response: Observations and modeling. *J. Geophys. Res. Ocean.* **114** (2009).
49. M Davidson, K Splinter, I Turner, A simple equilibrium model for predicting shoreline change. *Coast. Eng.* **73**, 191–202 (2013).
50. DL Kriebel, RG Dean, Convolution method for time-dependent beach-profile response. *J. Waterw. Port, Coastal, Ocean. Eng.* **119**, 204–226 (1993).
51. S Vitousek, et al., Are equilibrium shoreline models just convolutions? *J. Geophys. Res. Earth Surf.* **130**, e2025JF008452 (2025).
52. Y Mao, ShoreShop 2.0: Advancements in Shoreline Change Prediction Models (https://github.com/ShoreShop/ShoreModel_Benchmark) (2025).
53. JC Allan, PD Komar, *Morphologies of beaches and dunes on the Oregon coast, with tests of the geometric dune-erosion model.* (State of Oregon, Department of Geology and Mineral Industries), (2005).
54. P Ruggiero, GM Kaminsky, G Gelfenbaum, B Voigt, Seasonal to interannual morphodynamics along a high-energy dissipative littoral cell. *J. Coast. Res.* **21**, 553–578 (2005).
55. P Ruggiero, et al., National assessment of shoreline change: historical shoreline change along the pacific northwest coast, (US Geological Survey), Technical report (2013).

56. M Taherkhani, et al., ENSO and PDO drive shoreline position anomalies in the US Pacific Northwest. *PNAS Nexus* **5**, pgaf404 (2026).
57. PD Komar, *The Pacific Northwest coast: living with the shores of Oregon and Washington.* (Duke University Press), (1997).
58. T Burch, CR Sherwood, Historical bathymetric changes near the entrance to grays harbor, washington, (Pacific Northwest National Lab.(PNNL), Richland, WA (United States)), Technical report (1992).
59. GM Kaminsky, P Ruggiero, MC Buijsman, D McCandless, G Gelfenbaum, Historical evolution of the columbia river littoral cell. *Mar. Geol.* **273**, 96–126 (2010).
60. P Ruggiero, Is the intensifying wave climate of the us pacific northwest increasing flooding and erosion risk faster than sea-level rise? *J. Waterw. Port, Coastal, Ocean. Eng.* **139**, 88–97 (2013).
61. AW Stevens, et al., Climate controls on longshore sediment transport and coastal morphology adjacent to engineered inlets. *Coast. Eng.* **194**, 104617 (2024).
62. GM Kaminsky, MC Buijsman, P Ruggiero, Predicting shoreline change at decadal scale in the pacific northwest, usa in *Coastal Engineering 2000.* pp. 2400–2413 (2001).
63. M Buijsman, G Kaminsky, Shoreline change associated with jetty construction, deterioration, and rehabilitation at grays harbor, washington. *Shore & Beach* **71**, 15–22 (2003).
64. P Ruggiero, J List, D Hanes, J Eshleman, Probabilistic shoreline change modeling in *Coastal Engineering 2006: (In 5 Volumes).* (World Scientific), pp. 3417–3429 (2007).
65. P Ruggiero, M Buijsman, GM Kaminsky, G Gelfenbaum, Modeling the effects of wave climate and sediment supply variability on large-scale shoreline change. *Mar. Geol.* **273**, 127–140 (2010).
66. M Taherkhani, M Leung, P Ruggiero, S Vitousek, J Allan, Multiscale assessment of shoreline evolution in the us pacific northwest via a process-based model in *Coastal Sediments 2023: The Proceedings of the Coastal Sediments 2023.* pp. 1437–1451 (2023).
67. JA Antolínez, FJ Méndez, D Anderson, P Ruggiero, GM Kaminsky, Predicting climate-driven coastlines with a simple and efficient multiscale model. *J. Geophys. Res. Earth Surf.* **124**, 1596–1624 (2019).
68. The MathWorks Inc., Matlab version: 24.1 (r2024a) (2024).
69. PL Barnard, et al., Extreme oceanographic forcing and coastal response due to the 2015–2016 el niño. *Nat. Commun.* **8**, 14365 (2017).
70. JC Allan, PD Komar, Morphologies of beaches and dunes on the Oregon coast, with tests of the geometric dune-erosion model, (Oregon Department of Geology and Mineral Industries (DOGAMI)), Technical report (2005).
71. Center for Operational Oceanographic Products and Services, NOAA Tides and Currents (https://tidesandcurrents.noaa.gov/map/index.html) (2024).
72. RU Moskvichev, et al., Wave driven cross shore and alongshore transport reveal more extreme projections of shoreline change in island environments. *Sci. Reports* **15**, 10794 (2025).
73. KA Serafin, P Ruggiero, PL Barnard, HF Stockdon, The influence of shelf bathymetry and beach topography on extreme total water levels: Linking large-scale changes of the wave climate to local coastal hazards. *Coast. Eng.* **150**, 1–17 (2019).
74. CJ Willmott, On the validation of models. *Phys. geography* **2**, 184–194 (1981).
75. O Repina, et al., Evaluating five shoreline change models against 40 years of field survey data at an embayed sandy beach. *Coast. Eng.* **199**, 104738 (2025).
76. J Montaño, et al., A multiscale approach to shoreline prediction. *Geophys. Res. Lett.* **48**, e2020GL090587 (2021).
77. X Chen, M Banno, N Mori, Less is more: Short-term window calibration improves seasonal shoreline prediction in modeling. *Geophys. Res. Lett.* **52**, e2025GL117764 (2025).
78. K Vos, MD Harley, IL Turner, KD Splinter, Pacific shoreline erosion and accretion patterns controlled by el niño/southern oscillation. *Nat. Geosci.* **16**, 140–146 (2023).
79. S Wu, et al., Evaluation of ncep-cfsv2, era5, and ccmp wind datasets against buoy observations over zhejiang nearshore waters. *Ocean. Eng.* **259**, 111832 (2022).
80. T Kodaira, et al., Uncertainty in wave hindcasts in the north atlantic ocean. *Mar. Struct.* **89**, 103370 (2023).
81. T Chataigner, et al., Sensitivity of a one-line longshore shoreline change model to the mean wave direction. *Coast. Eng.* **172**, 104025 (2022).
82. M D'Anna, D Idier, B Castelle, S Vitousek, G Le Cozannet, Reinterpreting the bruun rule in the context of equilibrium shoreline models. *J. Mar. Sci. Eng.* **9**, 974 (2021).
83. A Seenath, J Dale, On the bruun rule suitability for modelling shoreline change. *Ocean. & Coast. Manag.* **255**, 107237 (2024).
84. A Seenath, Fundamental limitations of shoreline models. *Nat. Water* pp. 1–2 (2025).
85. U.S. Geological Survey, Landsat 5 mission (U.S. Geological Survey) (2013).
86. M Graffin, et al., Waterline responses to climate forcing along the north american west coast. *Commun. Earth & Environ.* **6**, 444 (2025).
87. G García-Medina, HT Özkan-Haller, P Ruggiero, Wave resource assessment in oregon and southwest washington, usa. *Renew. Energy* **64**, 203–214 (2014).
88. KA Serafin, P Ruggiero, HF Stockdon, The relative contribution of waves, tides, and nontidal residuals to extreme total water levels on us west coast sandy beaches. *Geophys. Res. Lett.* **44**, 1839–1847 (2017).
89. L McInnes, J Healy, N Saul, L Großberger, Umap: Uniform manifold approximation and projection. *J. Open Source Softw.* **3**, 861 (2018).
90. B Castelle, et al., Satellite-derived sandy shoreline trends and interannual variability along the atlantic coast of europe. *Sci. Reports* **14**, 13002 (2024).
91. A Gu, K Goel, C Ré, Efficiently modeling long sequences with structured state spaces. *arXiv preprint arXiv:2111.00396* (2021).
92. A Gu, T Dao, Mamba: Linear-time sequence modeling with selective state spaces. *arXiv preprint arXiv:2312.00752* (2023).
93. LH Erikson, C Hegermiller, PL Barnard, P Ruggiero, M van Ormondt, Projected wave conditions in the eastern north pacific under the influence of two cmip5 climate scenarios. *Ocean. Model.* **96**, 171–185 (2015).
94. W Sweet, et al., Global and regional sea level rise scenarios for the united states: Updated mean projections and extreme water level probabilities along u.s. coastlines, (National Oceanic and Atmospheric Administration, National Ocean Service, Silver Spring, MD), Technical Report NOS 01 (2022).
95. W Cai, et al., Anthropogenic impacts on twentieth-century enso variability changes. *Nat. Rev. Earth & Environ.* **4**, 407–418 (2023).
96. JC Allan, PD Komar, Extreme storms on the pacific northwest coast during the 1997-98 el niño and 1998-99 la niña. *J. coastal Res.* pp. 175–193 (2002).
97. H Chen, et al., Central-pacific el niño-southern oscillation less predictable under greenhouse warming. *Nat. Commun.* **15**, 4370 (2024).
98. JF Lübbecke, MJ McPhaden, Assessing the twenty-first-century shift in enso variability in terms of the bjerknes stability index. *J. Clim.* **27**, 2577–2587 (2014).
99. W Sun, B Wang, J Liu, Y Dai, Recent changes of pacific decadal variability shaped by greenhouse forcing and internal variability. *J. Geophys. Res. Atmospheres* **127**, e2021JD035812 (2022).
100. PL Barnard, et al., Dynamic flood modeling essential to assess the coastal impacts of climate change. *Sci. reports* **9**, 4309 (2019).
101. R Ranasinghe, On the need for a new generation of coastal change models for the 21st century. *Sci. reports* **10**, 2010 (2020).
102. A Durap, Multi-decadal spatiotemporal shoreline vulnerability assessment (1987–2025): integrating erosion-accretion dynamics for disaster risk reduction across 90 coastal transects. *Nat. Hazards* pp. 1–39 (2025).
103. A Durap, Beachface steepness modulates erosion but not recovery: Multi-decadal spatiotemporal shoreline evidence across 390 transects. *J. Sea Res.* p. 102644 (2025).
104. J Atkins, Othercolor plotting tool for MATLAB (https://www.mathworks.com/matlabcentral/fileexchange/30564-othercolor) (2025).
105. Stephen23, ColorBrewer: Attractive and Distinctive Colormaps (https://github.com/DrosteEffect/BrewerMap) (2025).
106. DJ Kroon, 2D Line Curvature and Normals (https://www.mathworks.com/matlabcentral/fileexchange/32696-2d-line-curvature-and-normals) (2025).
107. G Reeves, Smooth2a (https://www.mathworks.com/matlabcentral/fileexchange/23287-smooth2a) (2025).
108. L Zhaoxu, Taylor diagram class (https://www.mathworks.com/matlabcentral/fileexchange/130889-taylor-diagram-class) (2025).
109. S Vitousek, et al., The application of ensemble wave forcing to quantify uncertainty of shoreline change predictions. *J. Geophys. Res. Earth Surf.* **126**, e2019JF005506 (2021).
110. B Castelle, G Masselink, Morphodynamics of wave-dominated beaches. *Camb. Prisms: Coast. Futur.* **1**, e1 (2023).
111. P Ruggiero, PD Komar, JC Allan, Increasing wave heights and extreme value projections: The wave climate of the us pacific northwest. *Coast. Eng.* **57**, 539–552 (2010).
112. P Blondeaux, G Vittori, Boundary layer and sediment dynamics under sea waves in *Advances in coastal and ocean engineering.* (World Scientific), pp. 133–190 (1999).
113. MB Cardenas, H Jiang, Wave-driven porewater and solute circulation through rippled elastic sediment under highly transient forcing. *Limnol. Oceanogr. Fluids Environ.* **1**, 23–37 (2011).
114. S Rakhimbekova, DM O'Carroll, MS Andersen, MZ Wu, CE Robinson, Effect of transient wave forcing on the behavior of arsenic in a nearshore aquifer. *Environ. Sci. & Technol.* **52**, 12338–12348 (2018).
115. KA Serafin, P Ruggiero, Simulating extreme total water levels using a time-dependent, extreme value approach. *J. Geophys. Res. Ocean.* **119**, 6305–6329 (2014).
116. EJ Theuerkauf, AB Rodriguez, SR Fegley, RA Luettich Jr, Sea level anomalies exacerbate beach erosion. *Geophys. Res. Lett.* **41**, 5139–5147 (2014).
117. R Almar, et al., Influence of el niño on the variability of global shoreline position. *Nat. communications* **14**, 3133 (2023).
118. HF Stockdon, RA Holman, PA Howd, AH Sallenger Jr, Empirical parameterization of setup, swash, and runup. *Coast. engineering* **53**, 573–588 (2006).
119. PD Komar, J Allan, GM Dias-Mendez, JJ Marra, P Ruggiero, El niño and la niña: erosion processes and impacts in *Coastal Engineering 2000.* pp. 2414–2427 (2001).
120. JW Kamphuis, Alongshore sediment transport rate. *J. Waterw. Port, Coastal, Ocean. Eng.* **117**, 624–640 (1991).
121. CERC (US), *Shore protection manual.* (Department of the Army, Waterways Experiment Station, Corps of Engineers) Vol. 1, (1984).
122. I Turki, R Medina, G Coco, M Gonzalez, An equilibrium model to predict shoreline rotation of pocket beaches. *Mar. Geol.* **346**, 220–232 (2013).
123. C Jaramillo, M González, R Medina, I Turki, An equilibrium-based shoreline rotation model. *Coast. Eng.* **163**, 103789 (2021).
124. M Casas-Prat, et al., Wind-wave climate changes and their impacts. *Nat. Rev. Earth & Environ.* **5**, 23–42 (2024).
125. S Vitousek, et al., Doubling of coastal flooding frequency within decades due to sea-level rise. *Sci. reports* **7**, 1399 (2017).
126. M Taherkhani, et al., Sea-level rise exponentially increases coastal flood frequency. *Sci. reports* **10**, 6466 (2020).
127. P Bruun, Sea-level rise as a cause of shore erosion. *J. Waterw. Harb. division* **88**, 117–130 (1962).
128. RS Nerem, et al., Climate-change–driven accelerated sea-level rise detected in the altimeter era. *Proc. national academy sciences* **115**, 2022–2025 (2018).
129. S Rahmstorf, M Vermeer, Discussion of: Houston, jr and dean, rg, 2011. sea-level acceleration based on us tide gauges and extensions of previous global-gauge analyses. journal of coastal research, 27 (3), 409–417. *J. Coast. Res.* **27**, 784–787 (2011).
130. G Duveiller, D Fasbender, M Meroni, Revisiting the concept of a symmetric index of agreement for continuous datasets. *Sci. reports* **6**, 19401 (2016).
131. KE Taylor, Summarizing multiple aspects of model performance in a single diagram. *J. geophysical research: atmospheres* **106**, 7183–7192 (2001).

132. EB Goldstein, G Coco, NG Plant, A review of machine learning applications to coastal sediment transport and morphodynamics. *Earth-science reviews* **194**, 97–108 (2019).
133. V Cerqueira, L Torgo, I Mozetič, Evaluating time series forecasting models: An empirical study on performance estimation methods. *Mach. Learn.* **109**, 1997–2028 (2020).
134. H Shen, BA Tolson, J Mai, Time to update the split-sample approach in hydrological model calibration. *Water Resour. Res.* **58**, e2021WR031523 (2022).
135. I Loshchilov, F Hutter, Decoupled weight decay regularization. *arXiv preprint arXiv:1711.05101* (2017).
136. DP Kingma, J Ba, Adam: A method for stochastic optimization. *arXiv preprint arXiv:1412.6980* (2014).
137. E Moges, Y Demissie, L Larsen, F Yassin, Sources of hydrological model uncertainties and advances in their analysis. *Water* **13**, 28 (2021).
138. A Kroon, MA de Schipper, PH van Gelder, SG Aarninkhof, Ranking uncertainty: Wave climate variability versus model uncertainty in probabilistic assessment of coastline change. *Coast. Eng.* **158**, 103673 (2020).
139. B Castelle, et al., Satellite-derived shoreline detection at a high-energy meso-macrotidal beach. *Geomorphology* **383**, 107707 (2021).
140. M Graffin, et al., Monitoring interdecadal coastal change along dissipative beaches via satellite imagery at regional scale. *Camb. Prisms: Coast. Futur.* **1**, e42 (2023).
141. D Dommenget, M Latif, A cautionary note on the interpretation of eofs. *J. climate* **15**, 216–225 (2002).
142. AH Monahan, JC Fyfe, MH Ambaum, DB Stephenson, GR North, Empirical orthogonal functions: The medium is the message. *J. Clim.* **22**, 6501–6514 (2009).
143. NG Valiente, RJ McCarroll, G Masselink, T Scott, M Wiggins, Multi-annual embayment sediment dynamics involving headland bypassing and sediment exchange across the depth of closure. *Geomorphology* **343**, 48–64 (2019).
144. A Kroon, JC Christiaanse, AP Luijendijk, MAd Schipper, R Ranasinghe, Parameter uncertainty in medium-term coastal morphodynamic modeling. *Sci. Reports* **15**, 18471 (2025).
145. T Durrant, M Hemer, G Smith, C Trenham, D Greenslade, Cawcr wave hindcast-aggregated collection. *V5. CSIRO. Serv. Collect.* (2019).
146. CSIRO Data Access Portal, CAWCR Wave Hindcast Aggregated Collection (https://data.csiro.au/collection/csiro:39819) (2024).
147. Center for Operational Oceanographic Products and Services, NOAA Tides and Currents Web Services (https://tidesandcurrents.noaa.gov/web_services_info.html) (2024).

Supporting Information for

A convolutional, scale-adaptive framework for large-scale shoreline change modeling

Mohsen Taherkhani[a,b,c], Sean Vitousek[d], and Peter Ruggiero[e]

[a]Department of Civil, Environmental and Construction Engineering, University of Central Florida, Orlando, FL 32816, USA. [b]Center for Integrated Coastal Research, University of Central Florida, Orlando, FL 32816, USA. [c]Department of Civil and Construction Engineering, Oregon State University, Corvallis, OR 97331, USA. [d]U.S. Geological Survey, Pacific Coastal and Marine Science Center, Santa Cruz, CA 95060, USA. [e]College of Earth, Ocean, and Atmospheric Sciences, Oregon State University, Corvallis, OR 97331, USA.

Corresponding Author: Mohsen Taherkhani (E-mail: mohsen.taherkhani@ucf.edu)

The LaTeX template used to create this document can be accessed here: https://www.overleaf.com/latex/templates/tagged/pnas-official

This PDF file includes:

Supporting Information Text

Spatial coverage and discretization. Building upon the methodology established by ref. (1), Taherkhani et al. (2026) (2) constructed shore-perpendicular transects at 50-m alongshore intervals throughout the U.S. Pacific Northwest (PNW) coastline. From an initial compilation of approximately 15,000 transects spanning the PNW's outer coast, a rigorous selection process was implemented to ensure data quality and consistency. Only those transects were retained that met specific criteria: sandy beach segments extending several hundred meters alongshore, a minimum of 2 lidar-derived shoreline positions, and at least 160 and 96 satellite-derived shoreline positions during the 1984-2024 and 1984-1999 periods, respectively. This systematic screening process yielded 10,599 qualified transects distributed across 22 pre-defined sandy beach-dominated littoral cells across the PNW (3). The coastal segment between La Push and Neah Bay in northern Washington was excluded from our hindcasting analysis due to the relative quality degradation of satellite-derived shoreline data in this region. For additional methodological details, refer to Taherkhani et al. (2026) (2).

Historical wave, water level, and shoreline data. For our modeling effort, we utilized the CSIRO wave hindcast product (4, 5), which provides hourly wave triplets (significant wave heights, peak wave periods, and wave direction) on a global rectangular grid. This product has been rigorously validated against buoy observations and altimeters, demonstrating satisfactory results (6, 7). Our analysis incorporated hourly wave triplets from 17 deep water nodes situated in close proximity to the PNW coastline for the 1984-2024 period. To approximate breaking point wave conditions, we downscaled the deep water wave conditions to the 20-m depth contour using pre-developed lookup tables (8) as a SWAN model (9) surrogate. We then projected the daily averages of these propagated wave triplets onto our 50-m spaced alongshore transects. Additionally, we obtained historical water level data for our analyses from NOAA tide gauge stations (10) along the PNW coastline through the NOAA API service (11). Time series of daily water levels were assigned to each transect based on proximity to the nearest tide gauge station. We acknowledge the inherent limitations of this dataset, particularly regarding the spatial distribution of tide gauge stations across diverse and distant coastal environments, despite our methodology prioritizing stations with high data coverage (>90%) and using temporal averaging for data imputation.

Our analyses incorporated shoreline position data from three distinct sources: Earth-observing satellite imagery, airborne lidar surveys, and ground-based GPS surveys. Over 99% of shoreline positions are derived from Landsat 5, 7, and 8 missions' imagery acquired between 1984 and 2024 (12) using the CoastSat toolbox (13). We supplemented these with spatially high-resolution lidar surveys conducted in 2002 (14), 2009-2011 (15), and 2016 (16), which provided datum-based shoreline positions at the mean high water (MHW) level, approximately the 2.1 m North American Vertical Datum 1988 (NAVD88) elevation (3). Further enhancing our dataset, GPS-derived shoreline positions (also MHW position-based) have been collected seasonally to annually along select Oregon and Washington beaches since 1997 (17, 18) at an alongshore spacing of approximately 1-3 km. Both lidar and GPS measurements provide sub-meter horizontal accuracy (3). Notably, the shoreline positions derived from satellites serve as a visual proxy for standardized datum-based shoreline positions and may not precisely align with datum-based measurements, necessitating rectification for potential outliers, hydrodynamic contributions, and biases. Building upon and refining the methodology proposed by Graffin et al. (2023) (19) for the Columbia River Littoral Cell (CRLC) in northern Oregon and southern Washington, and utilizing available datum-based shoreline positions, Taherkhani et al. (2026) (2) corrected the raw satellite-derived shoreline positions for hydrodynamic contributions and biases throughout the entire PNW. For comprehensive details regarding historical wave, water level, and shoreline data utilized and the correction methodology for satellite-derived shoreline positions, refer to Taherkhani et al. (2026) (2).

Determining the dominant modes of historical shoreline variability. As detailed by Taherkhani et al. (2026) (2), Empirical Orthogonal Function (EOF) analysis (20) was used to examine the dominant patterns of shoreline position variability along the PNW coast via a MATLAB toolbox (21). This approach was guided by the established understanding that adjacent littoral cells function as distinct systems with minimal sediment exchange between them (3). Accordingly, the EOF framework was applied independently within each littoral cell. This method enabled identification and characterization of the primary 100 modes of shoreline position variability within each distinct littoral cell system. Fig. S1 provides a visual representation of the top three EOF modes and their corresponding variability explained across the PNW, as well as within individual littoral cells.

Spectral characteristics of the utilized Kernel (K) and Forcing (F) functions in our convolutional framework. As described in the main text, the general form of shoreline position variability in our convolutional framework is defined as:

$$Y(t) = \int_{t_0}^{t} \frac{-A\left(t-\tau\right)^{k-1} e^{-\frac{t-\tau}{\theta}}}{\theta^{k}\,\Gamma(k)}\, F(\tau)\, d\tau. \qquad [1]$$

Utilizing spectral analysis is advantageous for revealing potential effects of convolving distinct Forcing functions with Kernel functions, particularly regarding how the form of the Kernel function may modify the Forcing function upon convolution, which is demonstrated in the shoreline position response. Evaluating the Fourier transform of both sides of Eq. 1, it will turn into:

$$\mathcal{F}\left\{Y(t)\right\} = \mathcal{F}\left\{\int_{t_0}^{t} \frac{-A(t-\tau)^{k-1} e^{-\frac{t-\tau}{\theta}}}{\theta^{k}\Gamma(k)} F(\tau) d\tau\right\}. \qquad [2]$$

Note that the Fourier transform of the convolution of two functions is equal to the multiplication of the Fourier transform of each of them:

$$\widehat{Y}(\omega) = \widehat{K}(\omega) \cdot \widehat{F}(\omega) \quad [3]$$

The Fourier transform of the Kernel function (K) will appear as:

$$\widehat{K}(\omega) = \mathcal{F}\left\{ \frac{-A(t-\tau)^{k-1} e^{-\frac{t-\tau}{\theta}}}{\theta^k \Gamma(k)} \right\} = \frac{-A}{(1+i\omega\theta)^k}. \quad [4]$$

Then, Eq. 2 gets simplified to:

$$\widehat{Y}(\omega) = -A\left(1 + i\,\omega\,\theta\right)^{-k} \cdot \widehat{F}(\omega). \quad [5]$$

Here, the first term on the RHS (excluding the amplitude, A; i.e., $(1+i\,\omega\,\theta)^{-k}$) is often termed a "frequency-response factor (or transfer function)." In signal processing applications, this function delineates the effects on various frequencies as they traverse the kernel, such as the magnitude of which frequencies are boosted or attenuated, and the extent of the timing shift (phase lag) (22). Below represents how the magnitude (Eq. 6) of the Kernel function (K) appears when convolved with Forcing functions (F) approaching very low (i.e., $\omega \to 0$; Eq. 7) and high (i.e., $\omega \to \infty$; Eq. 8) frequencies:

$$\left|\widehat{K}(\omega)\right| = \left[1 + (\omega\,\theta)^2\right]^{-\frac{k}{2}}, \quad [6]$$

$$\omega \to 0 \implies \left|\widehat{K}(\omega)\right| \to 1, \quad [7]$$

$$\omega \to \infty \implies \left|\widehat{K}(\omega)\right| \to (\omega\,\theta)^{-k}. \quad [8]$$

This indicates that at lower frequencies, the Kernel function does not alter the magnitude of the Forcing function; however, at higher frequencies, the magnitude decreases substantially. Accordingly, the phase lag (Eq. 9), at both lower and higher frequencies (Eqs. 10 and 11, respectively), is expressed as:

$$\arg\left[\widehat{K}(\omega)\right] = -\,k\,\tan^{-1}\!\left(\omega\,\theta\right), \quad [9]$$

$$\omega \to 0 \implies \arg\left[\widehat{K}(\omega)\right] \to 0, \quad [10]$$

$$\omega \to \infty \implies \arg\left[\widehat{K}(\omega)\right] \to -k\frac{\pi}{2}. \quad [11]$$

This indicates that Forcing functions with lower frequencies generate a negligible phase lag, but at higher frequencies, the phase lag increases, resulting in shoreline positions exhibiting a more significant phase lag relative to the forcing function (the negative sign in Eq. 11 means that the forcing function leads the shoreline positions).

Simplifying the convolutional architecture of the interdecadal cross-shore shoreline position to Bruun rule. Assuming that the relative sea level rise (RSLR) in the time series of water levels during 1984-2024 approximately resembles a 2nd-order polynomial (through time), then, following the Forcing function defined for other components of shoreline position variability (i.e., F_{CS}, F_{CI}, and F_{Al}), the Forcing function for the interdecadal cross-shore component (F_{RSLR}) can be defined as:

$$F_{RSLR}(t) = \frac{d}{dt}\eta_{RSLR}(t) = \frac{d}{dt}\left(a\,t^2 + b\,t + c\right) = 2a\,t + b. \quad [12]$$

By utilizing a Kernel function similar to other components, the Kernel function for the interdecadal cross-shore component (K_{RSLR}) can be expressed as:

$$K_{RSLR}(t-\tau) = \frac{-A_{RSLR}\,(t-\tau)^{k_{RSLR}-1}\,e^{-\frac{t-\tau}{\theta_{RSLR}}}}{\theta_{RSLR}^{k_{RSLR}}\Gamma\left(k_{RSLR}\right)}. \quad [13]$$

Then, the interdecadal cross-shore component (RSLR-induced) shoreline position variability (Y_{RSLR}) has a convolutional form of the following:

$$\begin{aligned} Y_{RSLR}(t) &= \left[K_{RSLR} * F_{RSLR}\right](t) \\ &= \int_{t_0}^{t} K_{RSLR}(t-\tau)\,F_{RSLR}(\tau)\,d\tau \\ &= \int_{t_0}^{t} \frac{-A_{RSLR}\,(t-\tau)^{k_{RSLR}-1}\,e^{-\frac{t-\tau}{\theta_{RSLR}}}}{\theta_{RSLR}^{k_{RSLR}}\Gamma\left(k_{RSLR}\right)}\left(2a\,\tau + b\right)d\tau. \end{aligned} \quad [14]$$

Taking advantage of a change of variables (i.e., $u = t - \tau$), the equation above can emerge as:

$$Y_{RSLR}(t) = 2a\int_0^{t-t_0} \frac{-A_{RSLR}\,u^{k_{RSLR}-1}\,e^{-\frac{u}{\theta_{RSLR}}}}{\theta_{RSLR}^{k_{RSLR}}\Gamma\left(k_{RSLR}\right)}\,(t-u)\,du + \;b\int_0^{t-t_0} \frac{-A_{RSLR}\,u^{k_{RSLR}-1}\,e^{-\frac{u}{\theta_{RSLR}}}}{\theta_{RSLR}^{k_{RSLR}}\Gamma\left(k_{RSLR}\right)}\,du. \quad [15]$$

In this transformed equation, a particular integral form, generally known as "lower incomplete gamma function" appears, which has the following form:

$$\gamma(s,x) = \int_0^x t^{s-1} e^{-t}\, dt. \tag{16}$$

Subsequently, using the definition of the lower incomplete gamma function, Y_{RSLR} (Eq. 15) is expressed as:

$$Y_{RSLR}(t) = -\frac{A_{RSLR}}{\Gamma\big(k_{RSLR}\big)} \left\{ 2a \left[t\, \gamma\Big(k_{RSLR}, \frac{t-t_0}{\theta_{RSLR}}\Big) - \theta_{RSLR}\, \gamma\Big(k_{RSLR}+1, \frac{t-t_0}{\theta_{RSLR}}\Big) \right] + b\, \gamma\Big(k_{RSLR}, \frac{t-t_0}{\theta_{RSLR}}\Big) \right\}. \tag{17}$$

For further simplification, we apply a property of frequency-response factors for Forcing functions of extremely low frequency (i.e., $\omega \to 0$; Eq. 10), which physically represents the interdecadal fluctuations in the water level time series. This phenomenon, as a more severe (lower frequency) instance relative to interannual variations in water level time series, implies that k approaches 1 ($k \to 1$; or, equivalently, $\theta_{RSLR} \gg t - t_0$), manifesting as very gradual passive flooding-like behavior in reality. Taking $t_0 = 0$, Eq. 17 gets simplified to:

$$Y_{RSLR}(t) \approx -\frac{A_{RSLR}}{\theta_{RSLR}} \Big(a\, t^2 + b\, t \Big) = -\frac{A_{RSLR}}{\theta_{RSLR}} \int_0^t \frac{d}{d\tau} \eta_{RSLR}(\tau)\, d\tau = -C_{RSLR} \cdot \eta_{RSLR}(t). \tag{18}$$

This is equivalent to the famous Bruun rule (23), where $C_{RSLR} = \frac{A_{RSLR}}{\theta_{RSLR}}$ is a transect-specific constant, encompassing the influence of the shoreface slope ($\tan\beta$) at that transect. Following the same assumptions as above, it can be shown that applying a higher-order polynomial (e.g., a 3rd- or 4th-order polynomial) to represent the very low-frequency interdecadal variations in the water level time series yields the identical conclusion achieved above, yet the transect-specific constant (proportionality constant; $C_{RSLR} = \frac{A_{RSLR}}{\theta_{RSLR}}$) remains unchanged, meaning that $Y_{RSLR}(t) \propto -\eta_{RSLR}(t)$.

Modifying the mathematical representation of the Forcing function in our convolutional framework. The general convolutional form in evaluating the variability in shoreline positions is described as:

$$Y(t) = \int_{t_0}^{t} K(t-\tau) F(\tau)\, d\tau, \tag{19}$$

where the Gamma Probability Distribution Function (PDF)-like Kernel function (K) has the following form:

$$K(t-\tau) = \frac{-A\, \big(t-\tau\big)^{k-1} e^{-\frac{t-\tau}{\theta}}}{\theta^k\, \Gamma(k)}. \tag{20}$$

Here, if we assign $\mathfrak{F}$ as the anti-derivative of F (i.e., $\frac{d\mathfrak{F}}{dt} = F$), then, via integrating by parts, Eq. 19 can be formulated as:

$$Y(t) \;=\; \Big[K(t-\tau)\, \mathfrak{F}(\tau) \Big]_{t_0}^{t} \;-\; \int_{t_0}^{t} \mathfrak{F}(\tau)\, \frac{d}{d\tau} K(t-\tau)\, d\tau. \tag{21}$$

Further expansion of the equation above will yield:

$$\begin{aligned} Y(t) = {} & \frac{-A\, (t-\tau)^{k-1} e^{-\frac{t-\tau}{\theta}}}{\theta^k\, \Gamma\big(k\big)}\, \mathfrak{F}(\tau) \Bigg|_{\tau=t_0}^{\tau=t} - \int_{t_0}^{t} \mathfrak{F}(\tau)\, \frac{d}{d\tau} \left[\frac{-A\, (t-\tau)^{k-1} e^{-\frac{t-\tau}{\theta}}}{\theta^k\, \Gamma\big(k\big)} \right] d\tau \\ = {} & \frac{A\, t^{k-1}\, e^{-t/\theta}}{\theta^k\, \Gamma\big(k\big)}\, \mathfrak{F}(t_0) + \int_{t_0}^{t} \mathfrak{F}(\tau)\, \frac{d}{d\tau} \left[\frac{A\, (t-\tau)^{k-1} e^{-\frac{t-\tau}{\theta}}}{\theta^k\, \Gamma\big(k\big)} \right] d\tau \\ = {} & \frac{A\, t^{k-1}\, e^{-t/\theta}}{\theta^k\, \Gamma\big(k\big)}\, \mathfrak{F}(t_0) - \frac{A}{\theta^k\, \Gamma\big(k\big)} \int_{t_0}^{t} \mathfrak{F}(\tau)\, e^{-\frac{t-\tau}{\theta}}\, (t-\tau)^{k-2} \left[(k-1) - \frac{t-\tau}{\theta} \right] d\tau \\ = {} & \frac{A\, t^{k-1}\, e^{-t/\theta}}{\theta^k\, \Gamma\big(k\big)}\, \mathfrak{F}(t_0) - \frac{A(k-1)}{\theta^k\, \Gamma\big(k\big)} \int_{t_0}^{t} \mathfrak{F}(\tau)\, e^{-\frac{t-\tau}{\theta}}\, (t-\tau)^{k-2} d\tau + \frac{A}{\theta^{k+1}\, \Gamma\big(k\big)} \int_{t_0}^{t} \mathfrak{F}(\tau)\, e^{-\frac{t-\tau}{\theta}}\, (t-\tau)^{k-1} d\tau. \end{aligned} \tag{22}$$

Recalling the general form of the Kernel function (Eq. 20), if we define a new Kernel function, changing only the shape parameter as $k_{new} = k - 1$, this function will have the form:

$$K^*_{\text{new}}(t-\tau) = -\frac{1}{\theta}\, \frac{A(t-\tau)^{k-2}\, e^{-(t-\tau)/\theta}}{\theta^{k-1}\, \Gamma\big(k-1\big)}, \tag{23}$$

or, equivalently:

$$K_{\text{new}}(t-\tau) = -\,\frac{A(t-\tau)^{k-2}\, e^{-(t-\tau)/\theta}}{\theta^{k-1}\, \Gamma\big(k-1\big)}. \tag{24}$$

Then, by using the mathematical form of the new Kernel function, Eq. 22 gets simplified to:

$$Y(t) = \underbrace{\frac{A\,t^{k-1}\,e^{-t/\theta}}{\theta^k\,\Gamma\big(k\big)}\,\mathfrak{F}(t_0)}_{\text{Decays to 0 eventually}} + \frac{1}{\theta}\int_{t_0}^{t}\mathfrak{F}(\tau)\,K_{\text{new}}(t-\tau)d\tau - \frac{1}{\theta}\int_{t_0}^{t}\mathfrak{F}(\tau)\,K(t-\tau)d\tau. \qquad [25]$$

Given the exponential decrease on the end tail of the defined Kernel functions, the first term on the RHS of Eq. 25 above approaches zero eventually (after a few years in our long time series, assuming that $t_0 = 0$). With that in mind, comparing Eqs. 19 and 25, it is apparent that a clear link exists between the type of the specified Forcing functions and the corresponding Kernel functions inside our convolutional architecture. Defining the forcing functions without taking the time derivative of the corresponding anomalous term, contrary to our implemented methodology in the main text, is noteworthy for two reasons: (1) It adds a convolutional term that employs a new Kernel function with a reduced shape parameter ($k_{new} = k - 1$), which effectively reduces the time lag between the forcing (anomaly term) and response (shoreline position) signals, and (2) In the context of a "shallow" Convolutional Neural Network (CNN), using the anti-derivative of the initial forcing ($\mathfrak{F}$) introduces an additional convolution term (layer), whereby two different filters/kernels are applied to the forcing function ($\mathfrak{F}$), thus increasing the complexity of this shallow CNN. It can be shown that this procedure is recursive; each additional anti-derivative adds a convolutional layer with a new kernel function (although these functions have a different mathematical nature than the ones used in conventional deep CNNs) whose shape parameter is reduced by one (as long as the new shape parameter remains greater than or equal to 1). This creates a progressively deeper convolutional framework that captures increasingly complex dynamics between forcing and response, drawing stronger connections with state-of-the-art, deep CNNs. This also underscores the intrinsic nonlinearities present in our convolutional framework and the temporal spectrum dependencies between the chosen Forcing and Kernel functions in modeling shoreline position variation.

Redefining the convolutional framework as differential equations. Using the Fourier transform, we showed that our central convolution equation (Eq. 1) can be written as:

$$\widehat{Y}(\omega) = -\,A\,\big(1 + i\,\omega\,\theta\big)^{-\,k}\cdot\widehat{F}(\omega), \qquad [26]$$

and, it can be rearranged into:

$$\big(1 + i\,\omega\,\theta\big)^{k}\,\widehat{Y}(\omega) = -\,A\,\widehat{F}(\omega). \qquad [27]$$

Then, taking the inverse Fourier transform of both sides, the equation above is expressed as:

$$\mathcal{F}^{-1}\Big\{\big(1 + i\,\omega\,\theta\big)^{k}\,\widehat{Y}(\omega)\Big\}(t) \;=\; \mathcal{F}^{-1}\Big\{-A\,\widehat{F}(\omega)\Big\}(t), \qquad [28]$$

and, after some manipulation, it is represented as:

$$\big(1 + \theta\,D\big)^{k}\,Y(t) = -\,A\,F(t). \qquad [29]$$

In a special case, if k is an integer ($k = n$), the equation above can be rearranged into an nth-order linear differential equation:

$$\begin{gathered}(1 + \theta\,D)^{n}\,Y(t) = -\,A\,F(t)\\ \sum_{m=0}^{n}\binom{n}{m}\frac{\theta^m}{A}\frac{d^{\,m}Y(t)}{dt^{\,m}} = -\,F(t).\end{gathered} \qquad [30]$$

For example, in the case of $n = 2$, the main convolution equation (Eq. 1) can be simply written as:

$$\frac{1}{A}\Big(Y(t) + 2\theta\frac{dY}{dt} + \theta^2\frac{d^2Y}{dt^2}\Big) = -F(t). \qquad [31]$$

For non-integer k, the result is not a standard differential equation and requires fractional calculus.

In essence, comparing Eqs. 25 and 31 demonstrates a duality: Y can be seen as a result of convolving F (or its anti-derivatives) with specific Kernel functions, while F can be seen as being related to Y through a differential (or fractional differential) operation. This provides a flexible mathematical framework for modeling the dynamic nonlinear relationship between hydrodynamic forcings and shoreline position variability. This mathematical duality suggests that structured State-Space Models (SSMs; see e.g., (24)), which operate on the same continuous-time ODE formulation, may be a naturally well-suited deep learning architecture for shoreline change modeling, and potentially a direction that could be explored in future work.

Comparing our model's hindcasting performance to the benchmark models/ensembles. Table S1 compares our model's hindcast performance to the leading benchmarks in shoreline change modeling studies. We exclusively consider the most recent (2020-2026) benchmarking studies encompassing multiple models of diverse categories (i.e., process-based, reduced-complexity, or DL-based), as well as studies covering spatial extents on the order of hundreds of kilometers of sandy coasts, providing a holistic view on the current state of our hybrid, convolution-based model while spanning the expansive sandy beaches of the PNW.

Table S1. Comparison of our model's hindcast performance with the most recent, leading shoreline change benchmarking studies and models applied over spatial extents of hundreds of kilometers alongshore. The index of agreement (d) and Mielke's index (λ) are closely related mathematically, though Mielke's index tends to be more penalizing—meaning that, for instance, $\lambda = 0.5$ represents marginally better hindcast skill than $d = 0.5$. NMSE stands for Normalized Mean Square Error.

Study	Geographical area	Spatial extent (km)	# Models	Temporal coverage		RMSE (m)	λ, d, or $NMSE$
				Calibration	Validation		
Montaño et al. (2020) (25) (ShoreShop 1.0) (Benchmarking study)	Tairua Beach, New Zealand	1.2	10	1999–2014		3.0 (Calibration)	λ = 0.76 (Calibration)
					2014–2017	4.5 (Validation)	λ = 0.45 (Validation)
Vitousek et al. (2023) (26)	California coastline, U.S.	1760	1	1995–2015			
					2015–2020	12.4 (Validation)	d = 0.559 (Validation)
Vitousek et al. (2024) (27)	The U.S. South Atlantic Coast	1850	1	1990–2015			
					2015–2020	12.3 (Validation)	d = 0.44 (Validation)
Repina et al. (2025) (28) (Benchmarking study)	Narrabeen–Collaroy Beach, New South Wales, Australia	3.6	5	1979–1999			λ = 0.38–0.99 (Calibration)
					1999–2019	15–19 (Validation)	λ = 0.33–0.49 (Validation)
Mao et al. (2025) (29) (ShoreShop 2.0) (Benchmarking study)	Curl Curl Beach, New South Wales, Australia	∼1	34	1999–2019			
					2019–2023	∼8.9 at best (Validation)	λ = 0.5–0.6 (Validation)
Moskvichev et al. (2025) (30)	Island of Oʻahu, Hawaiʻi, U.S.	110	1	1990–2020			
					2020–2023	9.0 (Validation)	d = 0.3 (Validation)
Calcraft et al. (2026) (31)	New South Wales coastline, Australia	2000	1	1988–2019			
					2019–2025	12.9 (Validation)	$NMSE$ = 0.89 (Validation)
Our model	**The U.S. Pacific Northwest**	**530**	**1**	**1984–2014**		**14.1 (Calibration)**	**λ = 0.66 (Calibration)**
					2014–2024	**14.1 (Validation)**	**λ = 0.51 (Validation)**

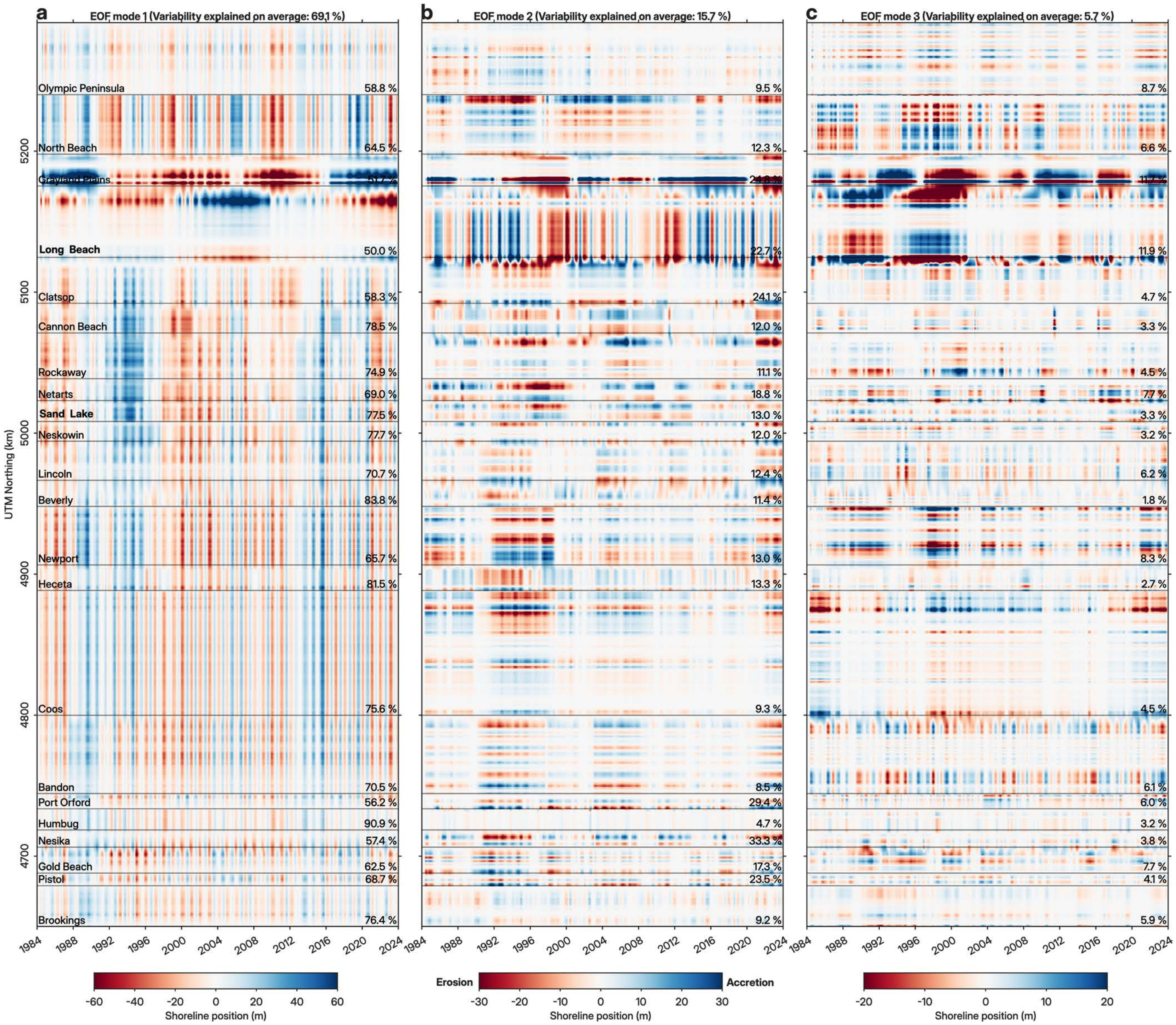

Fig. S1. Spatiotemporal representation of the top three EOF modes of historical shoreline position variability (1984-2024) across all 22 analyzed littoral cells in the PNW. Heatmaps of **(a)** EOF mode 1, **(b)** EOF mode 2, and **(c)** EOF mode 3, where the y-axis represents alongshore position (UTM Northing) spanning all littoral cells from south (Brookings) to north (Olympic Peninsula), and the x-axis represents time. The average percentage of total observed shoreline position variability explained by each mode across all littoral cells is specified in each panel title, with the per-littoral cell percentages displayed alongside each littoral cell. Positive shoreline position values indicate accretion (seaward movement) and negative values denote erosion (landward movement). In all littoral cells (except Long Beach), mode 1 predominantly captures cross-shore migration, while the combination of modes 2 and 3 indicates alongshore migration (e.g., curvature or breathing variability). Long Beach is a notable exception, with EOF mode 1 representing primarily alongshore variability (which, combined with mode 3, accounts for ∼62% of variability), while mode 2 mainly captures cross-shore variability (∼23% of variability). EOF analysis results are adopted from ref. (2).

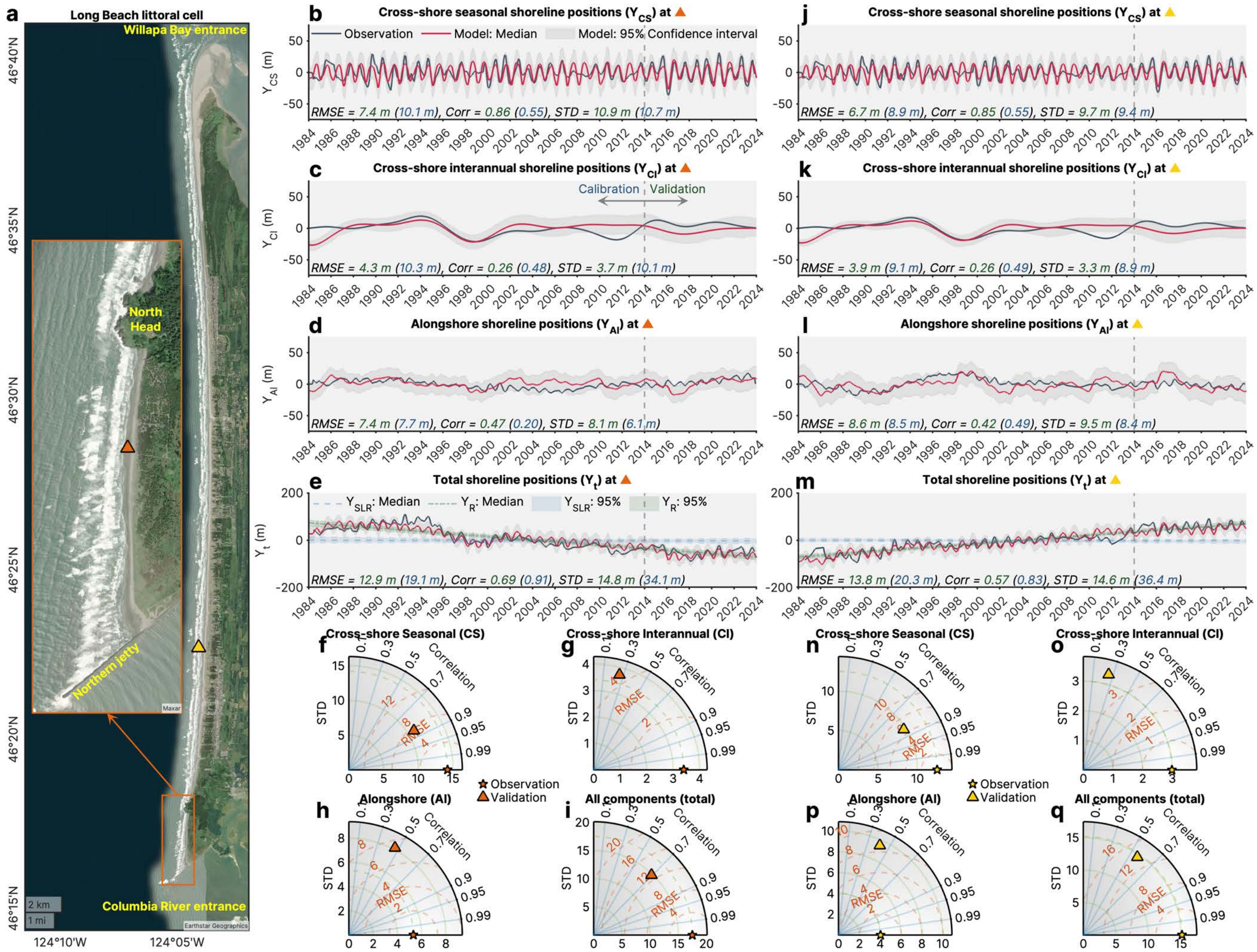

Fig. S2. Time series of the modeled and observed components of shoreline position variability and their hindcast performance for two example transects in Long Beach littoral cell, Washington. **(a)** The location of the example transects (transects #40 and #227, respectively, from south toward north, out of 839 transects) within this littoral cell. **(b-e)** Time series of the hindcast and observed shoreline positions for distinct components of variability, namely, cross-shore seasonal (Y_{CS}), cross-shore interannual (Y_{CI}), and alongshore (Y_{Al}) components, and total shoreline positions (Y_t), respectively, for the example transect denoted by the orange triangle in panel (a), with validation values shown first and calibration values in parentheses. Gray shading represents the 95% confidence intervals (C.I.) of the hindcast. The median trends and 95% C.I. of the relative sea level rise-induced (Y_{RSLR}) and residual (Y_R) components are also shown in panels (e) and (m). The dashed vertical lines separate the calibration (1984–2014) and validation (2014–2024) periods. **(f-i)** Taylor diagrams for the various components and total shoreline positions in this example transect during the validation period. The Root-Mean-Squared-Error ($RMSE$), Pearson correlation coefficient ($Corr$), and standard deviation (STD) for modeled individual components and total shoreline positions, for both calibration and validation periods, are shown in the respective panels. Panels **(j-q)** represent the same information (as shown in panels (b-i)) for the second example transect in this littoral cell, shown via the yellow triangle in panel (a). Credit: basemaps, Earthstar Geographics (via MATLAB (32)).

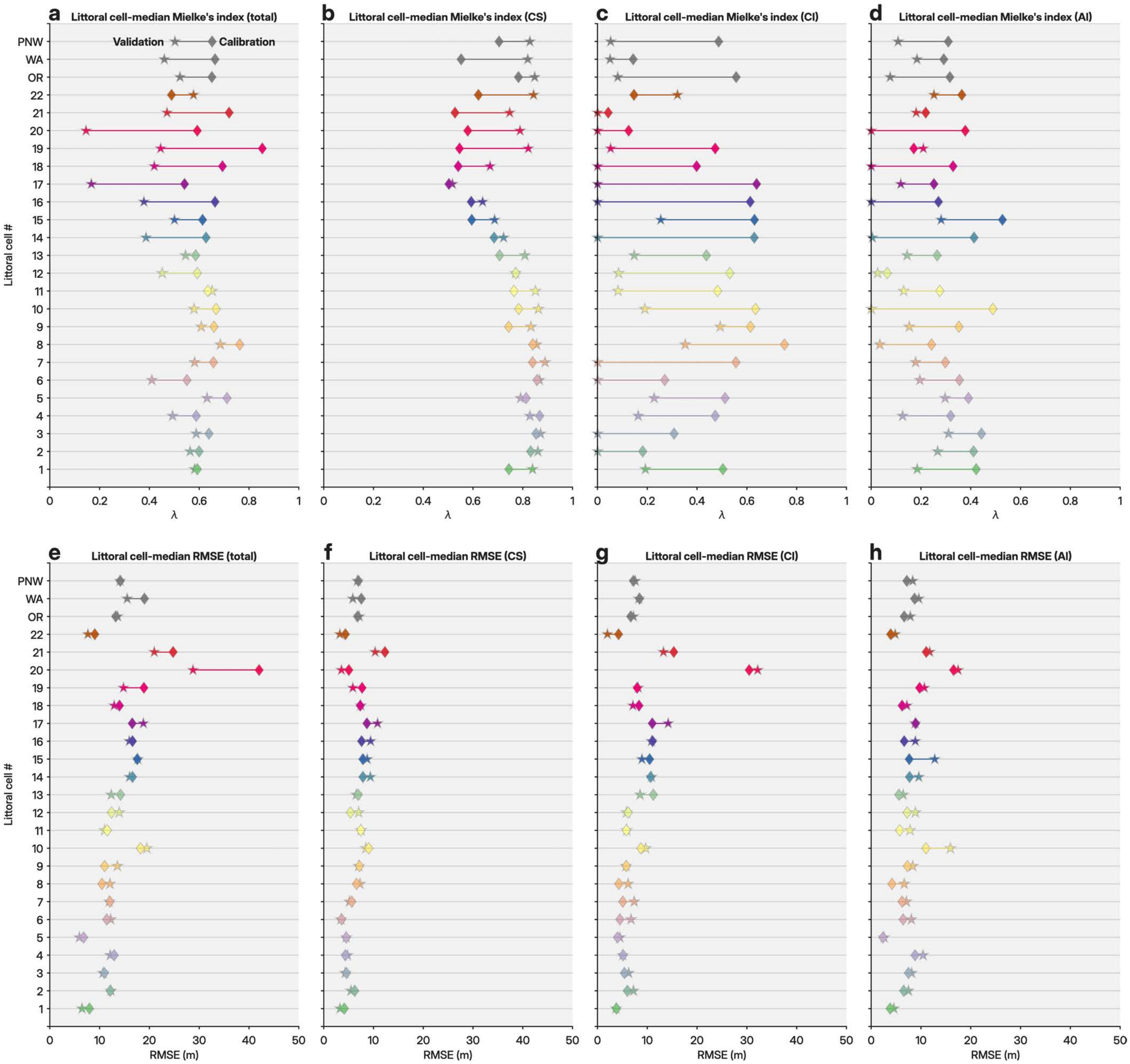

Fig. S3. Littoral cell-median Mielke's index (λ) and Root-Mean-Square-Error ($RMSE$) for total and individual components of shoreline position variability across the 22 analyzed littoral cells in the PNW. (a-d) Mielke's index (λ; where 0 indicates no skill and 1 indicates perfect agreement) for total, cross-shore seasonal (CS), cross-shore interannual (CI), and alongshore (Al) components, respectively. **(e-h)** Root-Mean-Squared-Error ($RMSE$; in meters) for the same components. Diamonds and stars denote littoral cell-median values during the calibration (1984-2014) and validation (2014-2024) periods, respectively. Regional medians aggregated across Oregon (OR), Washington (WA), and the entire PNW are shown at the top of each panel.

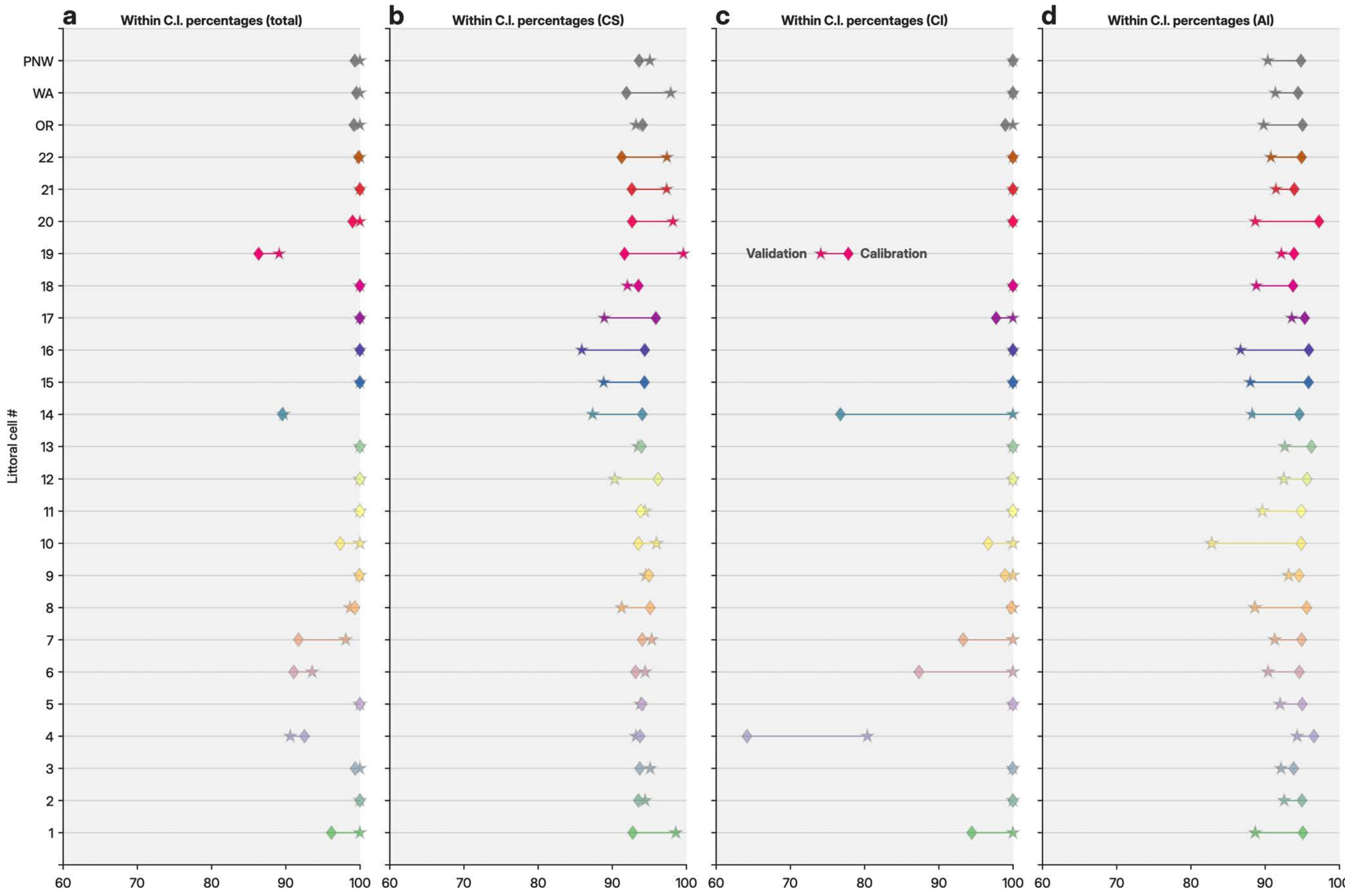

Fig. S4. Empirical coverage percentages of the 95% confidence intervals (C.I.) for total and individual components of shoreline position variability across the 22 analyzed littoral cells in the PNW. Within-C.I. percentages, i.e., the fraction of observed shoreline positions falling within the modeled 95% C.I. bands derived from the autoregressive (AR) residual-based uncertainty quantification, for **(a)** total, **(b)** cross-shore seasonal (CS), **(c)** cross-shore interannual (CI), and **(d)** alongshore (Al) components of shoreline position variability. Diamonds and stars denote littoral cell-median values during the calibration (1984-2014) and validation (2014-2024) periods, respectively. Regional medians aggregated across Oregon (OR), Washington (WA), and the entire PNW are shown at the top of each panel. Coverage rates near or above the nominal 95% level indicate well-calibrated to slightly conservative uncertainty bands.

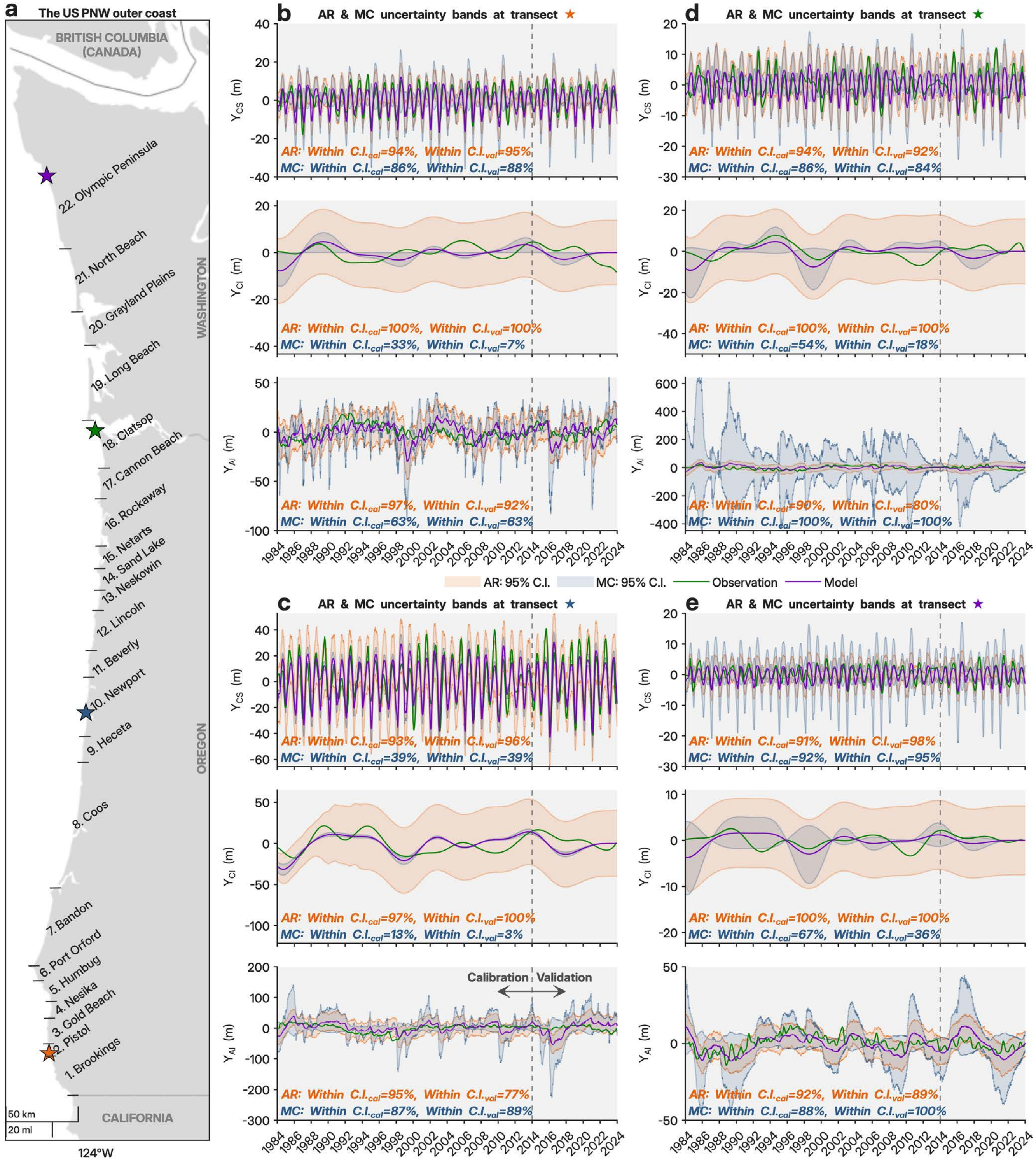

Fig. S5. Comparison of autoregressive (AR) residual-based and Monte Carlo (MC) parameter perturbation uncertainty bands at four selected example transects across the PNW. (a) Map of the PNW outer coast showing the locations of the four example transects. **(b-e)** Time series of observed and modeled shoreline positions for the cross-shore seasonal (Y_{CS}), cross-shore interannual (Y_{CI}), and alongshore (Y_{Al}) components at each transect, with the AR-based 95% C.I. (orange shading) and MC-based 95% C.I. (blue shading) overlaid, each derived from 100 ensemble simulations. For the MC approach, the four kernel parameters of each component (A, k, θ, τ) are randomly perturbed around their optimized values: A is sampled in normal space, while k, θ, and τ are sampled in log-space to preserve positivity. In both cases, the perturbation standard deviation is taken as the standard deviation of each parameter across all transects within the corresponding littoral cell, and the model is re-evaluated for each realization. The within-C.I. coverage rates during calibration (1984-2014) and validation (2014-2024) periods are reported for both methods on each panel. The dashed vertical line separates the calibration and validation periods. The four transects were selected to span a range of performance levels and geomorphic settings: (b) a well-performing transect near the south of Pistol littoral cell (transect #40 out of 157 transects, from south to north), representative of open-coast conditions; (c) a moderately performing transect near the south of Newport littoral cell (transect #285 out of 712 transects); (d) a relatively poor-performing transect at the northern extremity of Clatsop littoral cell, adjacent to the southern jetty of the Columbia River entrance (transect #519 out of 561 transects); and (e) a moderately performing transect adjacent to the unjettied entrance of Hoh River in Olympic Peninsula littoral cell (transect #880 out of 923 transects). Credit: basemaps, Natural Earth (via MATLAB (32)).

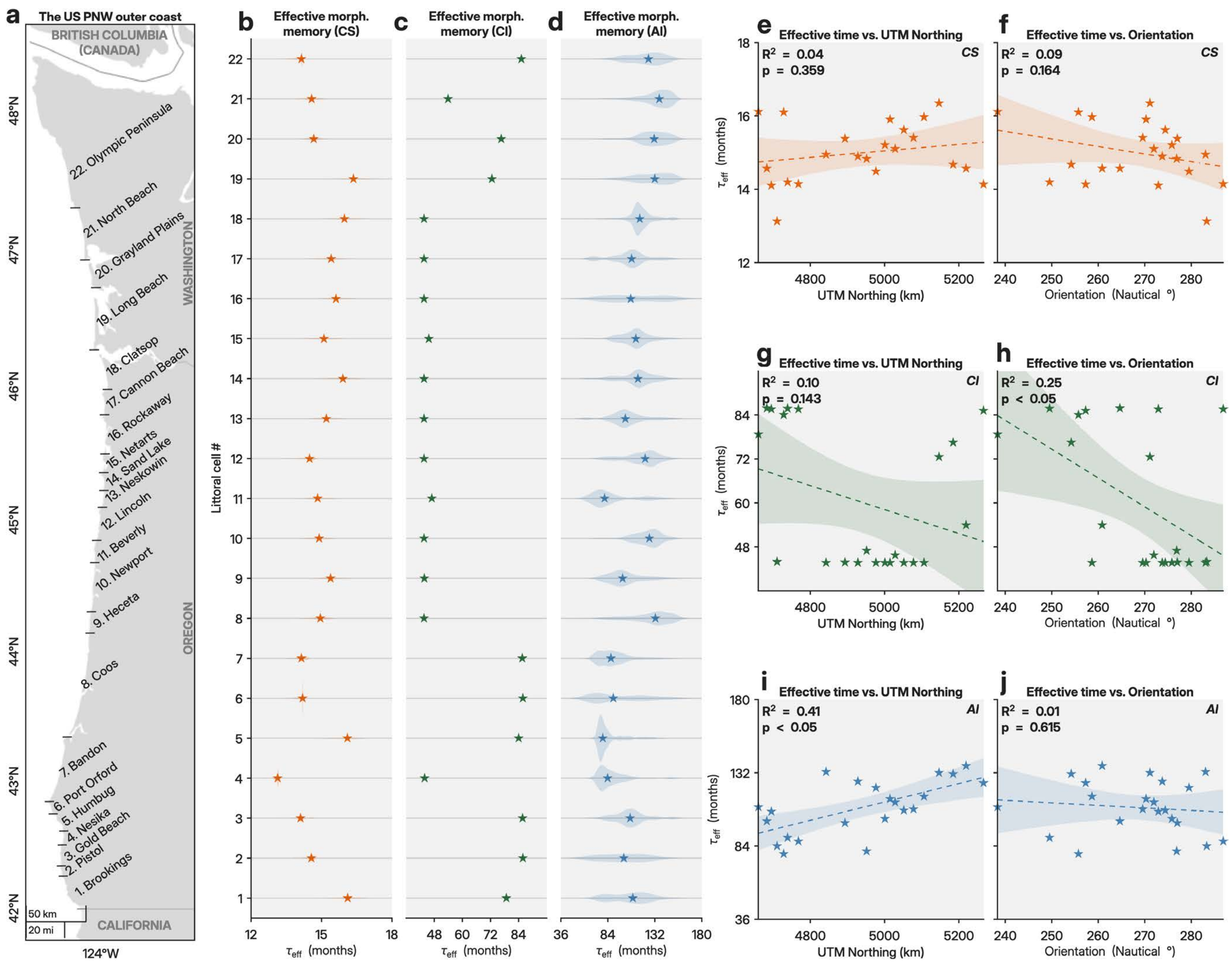

Fig. S6. Effective morphodynamic memory (τ_{eff}) of the optimized kernel functions (K) across the 22 analyzed littoral cells in the PNW. (a) Map of the U.S. Pacific Northwest (PNW) outer coast showing the locations and boundaries of all 22 analyzed littoral cells. **(b–d)** Violin plots depicting the within-littoral cell distribution of τ_{eff} (in months) for the cross-shore seasonal (CS; orange), cross-shore interannual (CI; green), and alongshore (Al; blue) components, respectively. Stars denote littoral cell-median values. **(e–j)** Littoral cell-median τ_{eff} linearly regressed against littoral cell-average UTM Northing (left column; in km) and shore-normal orientation (right column; in nautical degrees of seaward shore-normals) for each component (denoted at the top-right of each panel), with the coefficient of determination (R^2) and its corresponding p-value (with a significance level of $\alpha = 0.05$) reported. Dashed lines indicate the best-fit regression, with shading representing the 95% confidence interval (C.I.) of the linear fit. Credit: basemaps, Natural Earth (via MATLAB (32)).

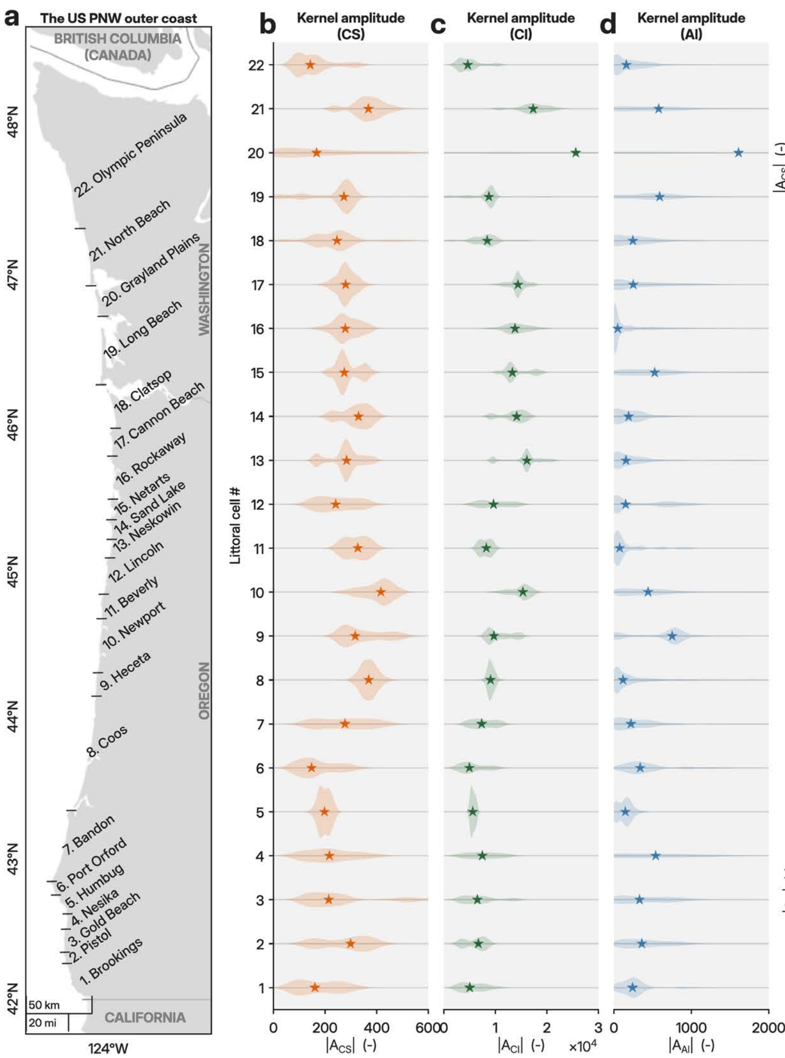

Fig. S7. Kernel amplitude ($|A|$) of the optimized kernel functions (K) across the 22 analyzed littoral cells in the PNW. (a) Map of the U.S. Pacific Northwest (PNW) outer coast showing the locations and boundaries of all 22 analyzed littoral cells. **(b–d)** Violin plots depicting the within-littoral cell distribution of $|A|$ (dimensionless) for the cross-shore seasonal (CS; orange), cross-shore interannual (CI; green), and alongshore (Al; blue) components, respectively. Stars denote littoral cell-median values. **(e–j)** Littoral cell-median $|A|$ linearly regressed against littoral cell-average UTM Northing (left column; in km) and shore-normal orientation (right column; in nautical degrees of seaward shore-normals) for each component (denoted at the top-right of each panel), with the coefficient of determination (R^2) and its corresponding p-value (with a significance level of $\alpha = 0.05$) reported. Dashed lines indicate the best-fit regression, with shading representing the 95% confidence interval (C.I.) of the linear fit. Credit: basemaps, Natural Earth (via MATLAB (32)).

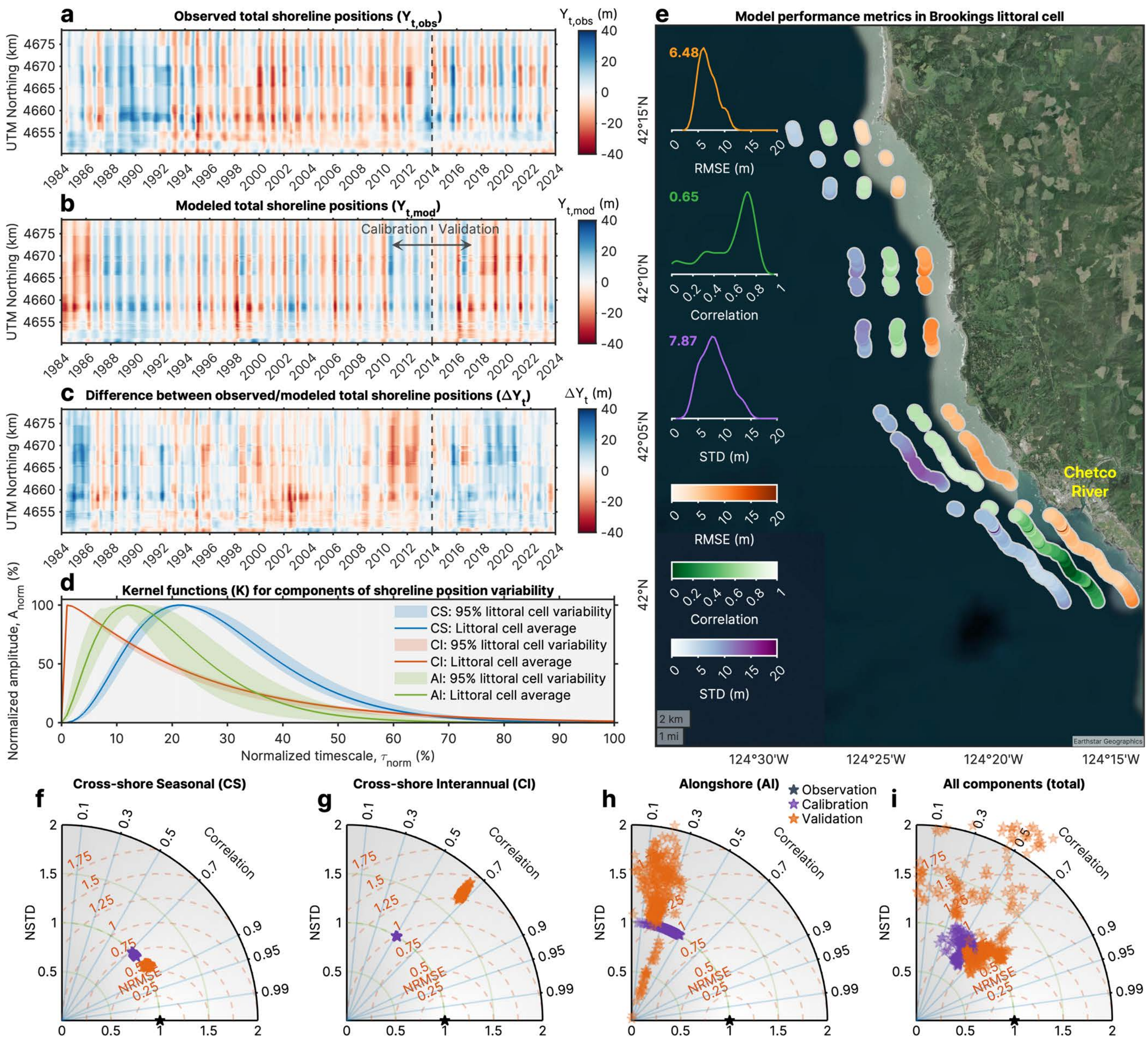

Fig. S8. Hindcast performance of the historical (observed) shoreline positions throughout Brookings littoral cell, Oregon. Spatiotemporal representation (heatmap; y-axis denotes the UTM northing and x-axis specifies time) of the total **(a)** observed ($Y_{t,obs}$) and **(b)** modeled (hindcast) ($Y_{t,mod}$) shoreline positions, alongside **(c)** their difference ($\Delta Y_t = Y_{t,obs} - Y_{t,mod}$). The dashed vertical line separates the calibration (1984–2014) and validation (2014–2024) periods. **(d)** The normalized (adjusted for amplitude [A] and effective morphodynamic memory [τ_{eff}]) shapes of the convolution kernel functions (K) optimized for all transects across this littoral cell, colored by component (orange: CS, green: CI, blue: Al), with solid lines representing the littoral cell average and shading denoting the 95% within-littoral cell variability across transects. **(e)** Spatial (alongshore) variability of the Root-Mean-Squared-Error ($RMSE$), Pearson correlation coefficient ($Corr$), and standard deviation (STD) of the modeled total shoreline positions during the validation period (2014-2024) in this littoral cell. This panel also features the kernel density estimation (KDE) for each metric across all transects within this littoral cell, alongside their littoral cell-median values shown by their corresponding color (the y-axis is not scaled). **(f-i)** The normalized (for standard deviation [$NSTD$] and Root-Mean-Squared-Error [$NRMSE$]) Taylor diagrams for distinct modeled components and the total shoreline position variability of all transects in this littoral cell, during both calibration and validation periods, where each point corresponds to an individual transect. Credit: basemaps, Earthstar Geographics (via MATLAB (32)).

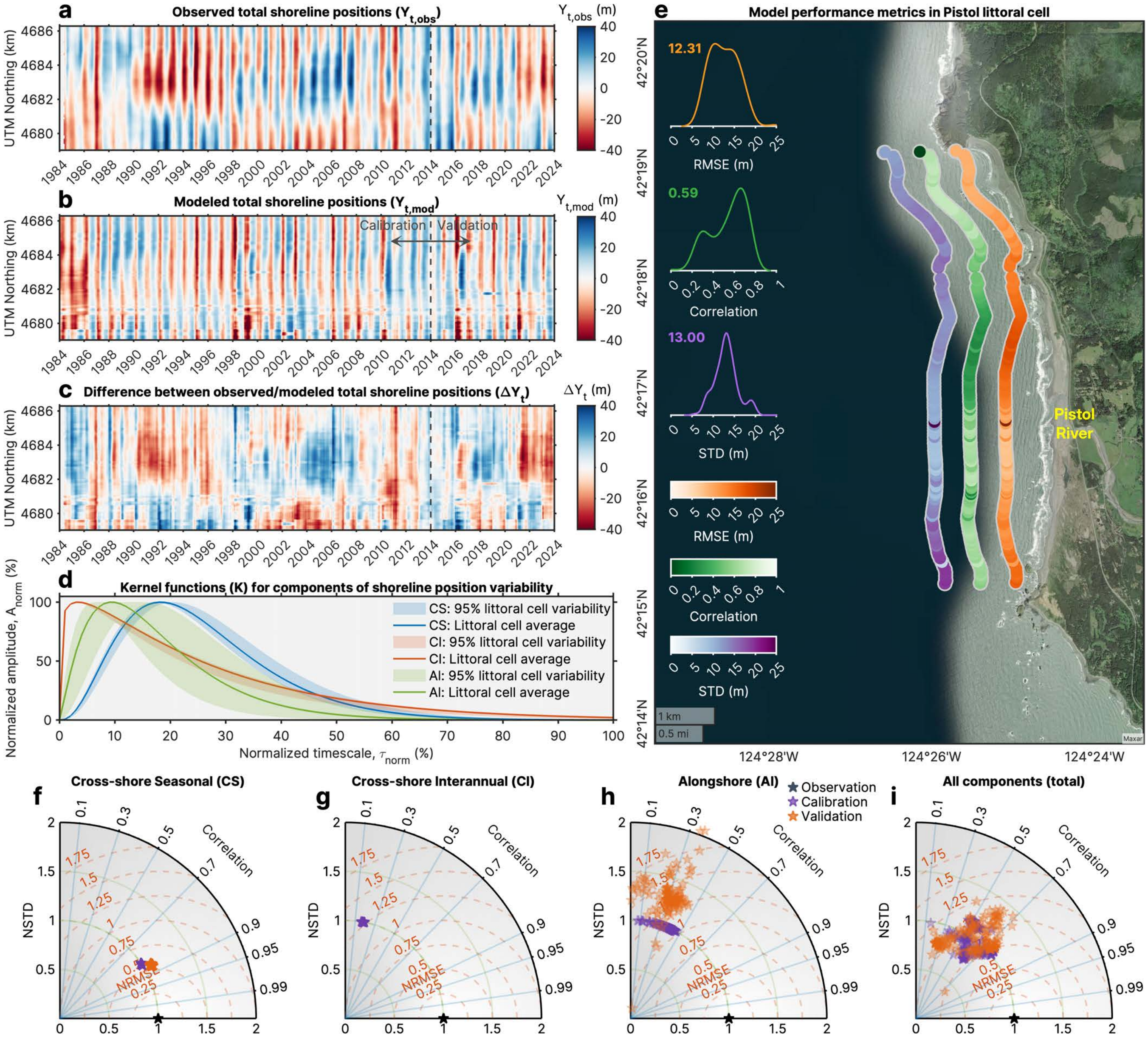

Fig. S9. Hindcast performance of the historical (observed) shoreline positions throughout Pistol littoral cell, Oregon. Spatiotemporal representation (heatmap; y-axis denotes the UTM northing and x-axis specifies time) of the total **(a)** observed ($Y_{t,obs}$) and **(b)** modeled (hindcast) ($Y_{t,mod}$) shoreline positions, alongside **(c)** their difference ($\Delta Y_t = Y_{t,obs} - Y_{t,mod}$). The dashed vertical line separates the calibration (1984–2014) and validation (2014–2024) periods. **(d)** The normalized (adjusted for amplitude [A] and effective morphodynamic memory [τ_{eff}]) shapes of the convolution kernel functions (K) optimized for all transects across this littoral cell, colored by component (orange: CS, green: CI, blue: Al), with solid lines representing the littoral cell average and shading denoting the 95% within-littoral cell variability across transects. **(e)** Spatial (alongshore) variability of the Root-Mean-Squared-Error ($RMSE$), Pearson correlation coefficient ($Corr$), and standard deviation (STD) of the modeled total shoreline positions during the validation period (2014-2024) in this littoral cell. This panel also features the kernel density estimation (KDE) for each metric across all transects within this littoral cell, alongside their littoral cell-median values shown by their corresponding color (the y-axis is not scaled). **(f-i)** The normalized (for standard deviation [$NSTD$] and Root-Mean-Squared-Error [$NRMSE$]) Taylor diagrams for distinct modeled components and the total shoreline position variability of all transects in this littoral cell, during both calibration and validation periods, where each point corresponds to an individual transect. Credit: basemaps, Earthstar Geographics (via MATLAB (32)).

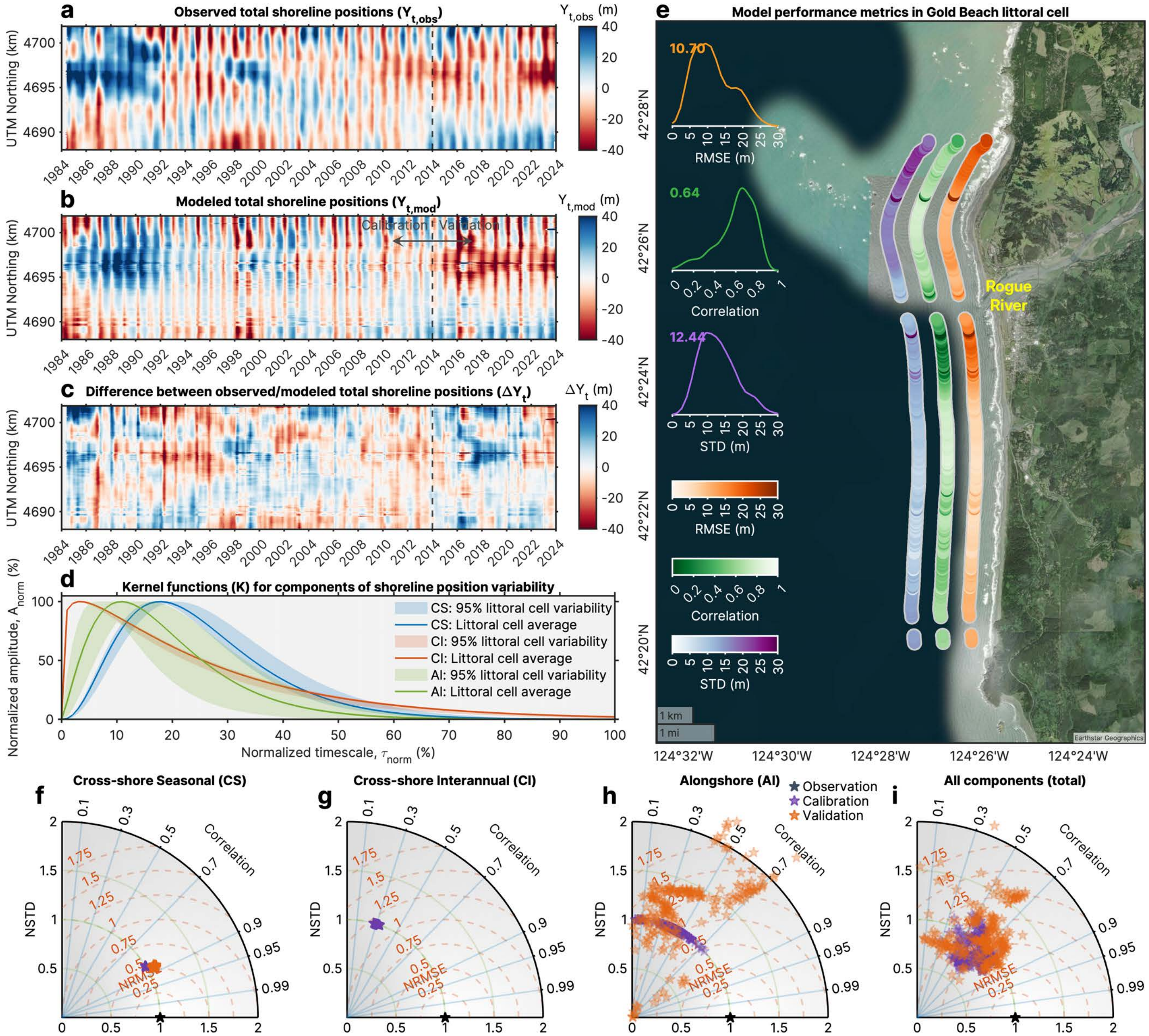

Fig. S10. Hindcast performance of the historical (observed) shoreline positions throughout Gold Beach littoral cell, Oregon. Spatiotemporal representation (heatmap; y-axis denotes the UTM northing and x-axis specifies time) of the total **(a)** observed ($Y_{t,obs}$) and **(b)** modeled (hindcast) ($Y_{t,mod}$) shoreline positions, alongside **(c)** their difference ($\Delta Y_t = Y_{t,obs} - Y_{t,mod}$). The dashed vertical line separates the calibration (1984–2014) and validation (2014–2024) periods. **(d)** The normalized (adjusted for amplitude [A] and effective morphodynamic memory [τ_{eff}]) shapes of the convolution kernel functions (K) optimized for all transects across this littoral cell, colored by component (orange: CS, green: CI, blue: Al), with solid lines representing the littoral cell average and shading denoting the 95% within-littoral cell variability across transects. **(e)** Spatial (alongshore) variability of the Root-Mean-Squared-Error ($RMSE$), Pearson correlation coefficient ($Corr$), and standard deviation (STD) of the modeled total shoreline positions during the validation period (2014-2024) in this littoral cell. This panel also features the kernel density estimation (KDE) for each metric across all transects within this littoral cell, alongside their littoral cell-median values shown by their corresponding color (the y-axis is not scaled). **(f-i)** The normalized (for standard deviation [$NSTD$] and Root-Mean-Squared-Error [$NRMSE$]) Taylor diagrams for distinct modeled components and the total shoreline position variability of all transects in this littoral cell, during both calibration and validation periods, where each point corresponds to an individual transect. Credit: basemaps, Earthstar Geographics (via MATLAB (32)).

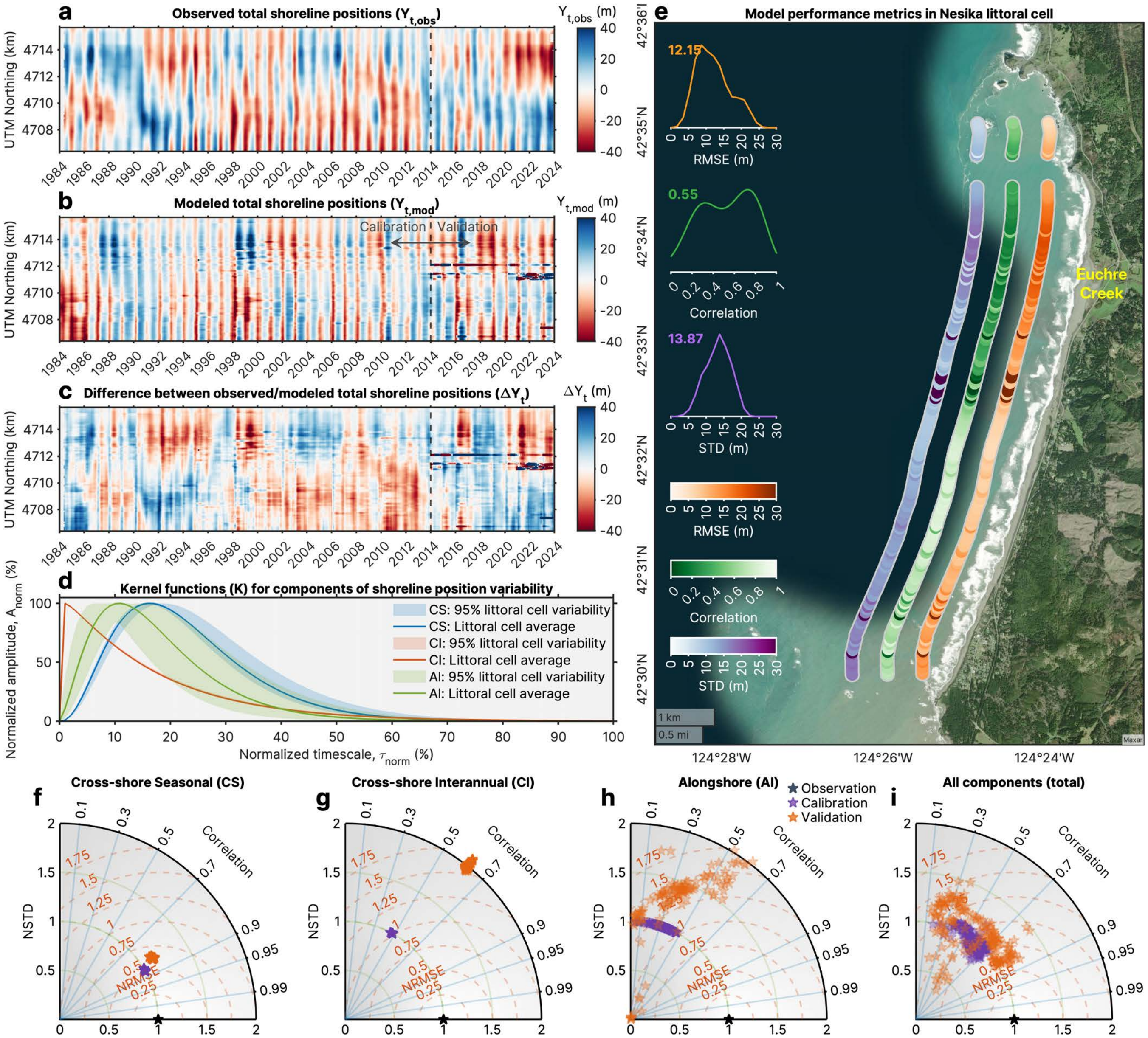

Fig. S11. Hindcast performance of the historical (observed) shoreline positions throughout Nesika littoral cell, Oregon. Spatiotemporal representation (heatmap; y-axis denotes the UTM northing and x-axis specifies time) of the total **(a)** observed ($Y_{t,obs}$) and **(b)** modeled (hindcast) ($Y_{t,mod}$) shoreline positions, alongside **(c)** their difference ($\Delta Y_t = Y_{t,obs} - Y_{t,mod}$). The dashed vertical line separates the calibration (1984–2014) and validation (2014–2024) periods. **(d)** The normalized (adjusted for amplitude [A] and effective morphodynamic memory [τ_{eff}]) shapes of the convolution kernel functions (K) optimized for all transects across this littoral cell, colored by component (orange: CS, green: CI, blue: Al), with solid lines representing the littoral cell average and shading denoting the 95% within-littoral cell variability across transects. **(e)** Spatial (alongshore) variability of the Root-Mean-Squared-Error ($RMSE$), Pearson correlation coefficient ($Corr$), and standard deviation (STD) of the modeled total shoreline positions during the validation period (2014-2024) in this littoral cell. This panel also features the kernel density estimation (KDE) for each metric across all transects within this littoral cell, alongside their littoral cell-median values shown by their corresponding color (the y-axis is not scaled). **(f-i)** The normalized (for standard deviation [$NSTD$] and Root-Mean-Squared-Error [$NRMSE$]) Taylor diagrams for distinct modeled components and the total shoreline position variability of all transects in this littoral cell, during both calibration and validation periods, where each point corresponds to an individual transect. Credit: basemaps, Earthstar Geographics (via MATLAB (32)).

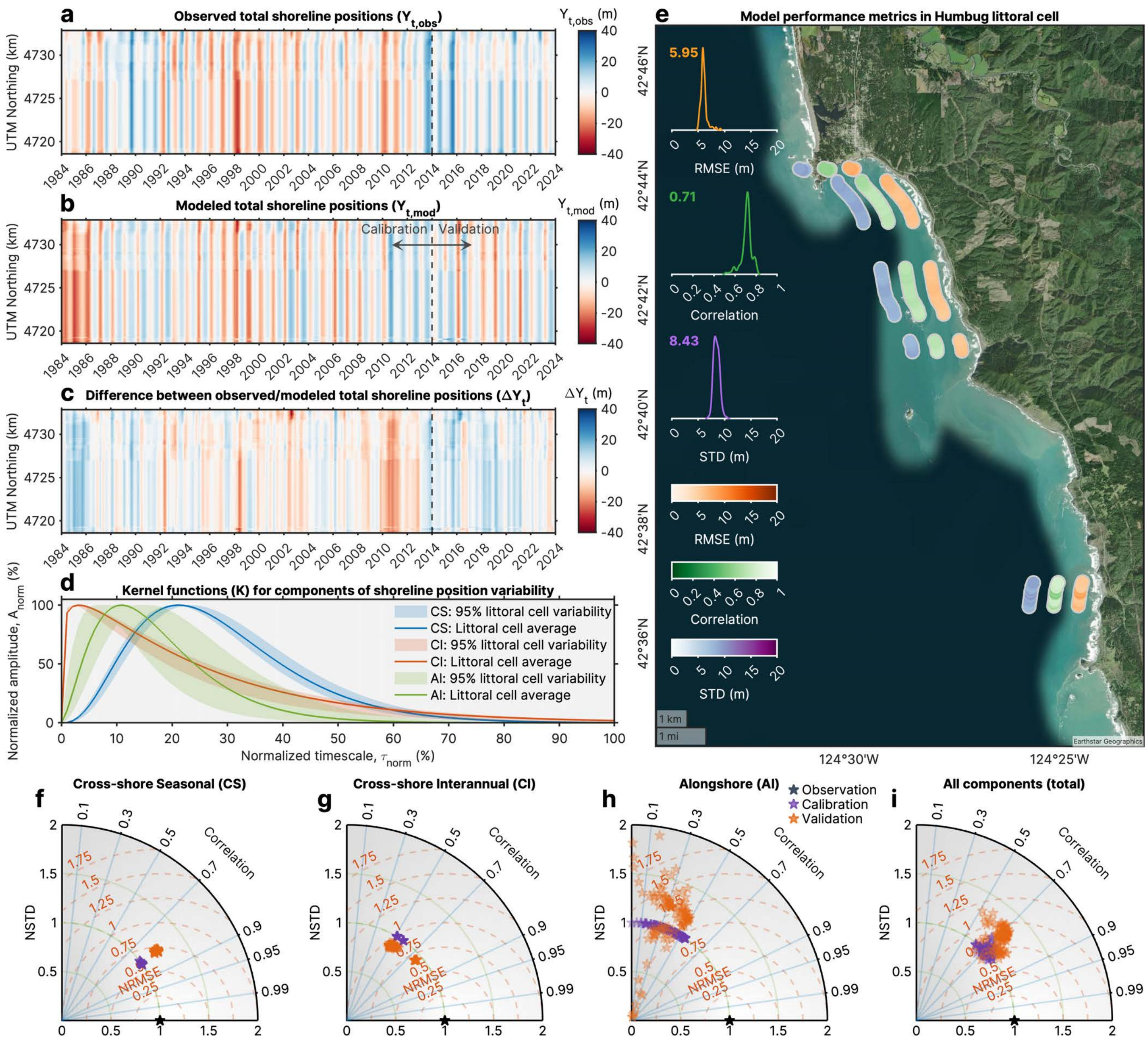

Fig. S12. Hindcast performance of the historical (observed) shoreline positions throughout Humbug littoral cell, Oregon. Spatiotemporal representation (heatmap; y-axis denotes the UTM northing and x-axis specifies time) of the total **(a)** observed ($Y_{t,obs}$) and **(b)** modeled (hindcast) ($Y_{t,mod}$) shoreline positions, alongside **(c)** their difference ($\Delta Y_t = Y_{t,obs} - Y_{t,mod}$). The dashed vertical line separates the calibration (1984–2014) and validation (2014–2024) periods. **(d)** The normalized (adjusted for amplitude [A] and effective morphodynamic memory [τ_{eff}]) shapes of the convolution kernel functions (K) optimized for all transects across this littoral cell, colored by component (orange: CS, green: CI, blue: Al), with solid lines representing the littoral cell average and shading denoting the 95% within-littoral cell variability across transects. **(e)** Spatial (alongshore) variability of the Root-Mean-Squared-Error ($RMSE$), Pearson correlation coefficient ($Corr$), and standard deviation (STD) of the modeled total shoreline positions during the validation period (2014-2024) in this littoral cell. This panel also features the kernel density estimation (KDE) for each metric across all transects within this littoral cell, alongside their littoral cell-median values shown by their corresponding color (the y-axis is not scaled). **(f-i)** The normalized (for standard deviation [$NSTD$] and Root-Mean-Squared-Error [$NRMSE$]) Taylor diagrams for distinct modeled components and the total shoreline position variability of all transects in this littoral cell, during both calibration and validation periods, where each point corresponds to an individual transect. Credit: basemaps, Earthstar Geographics (via MATLAB (32)).

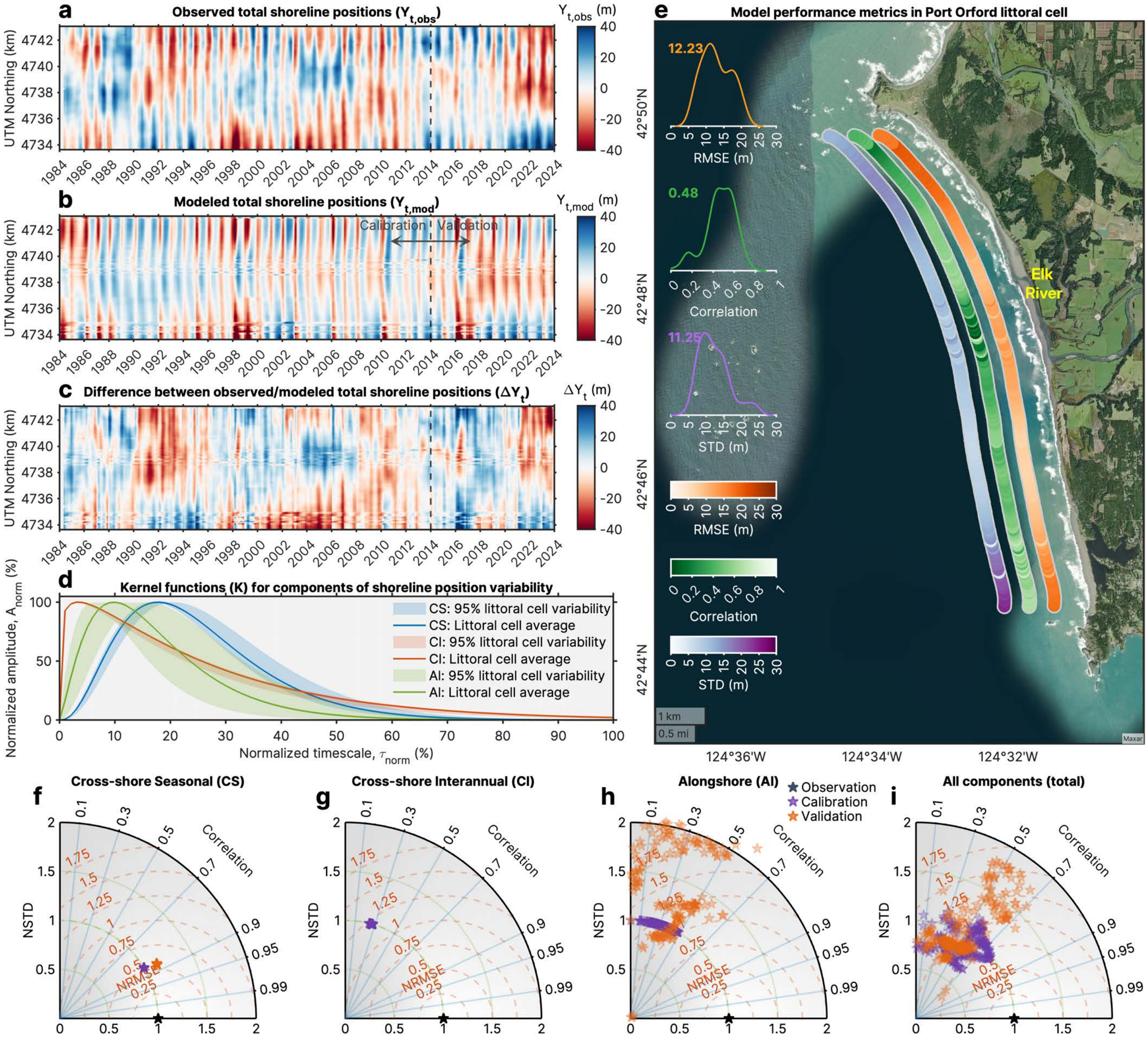

Fig. S13. Hindcast performance of the historical (observed) shoreline positions throughout Port Orford littoral cell, Oregon. Spatiotemporal representation (heatmap; y-axis denotes the UTM northing and x-axis specifies time) of the total **(a)** observed ($Y_{t,obs}$) and **(b)** modeled (hindcast) ($Y_{t,mod}$) shoreline positions, alongside **(c)** their difference ($\Delta Y_t = Y_{t,obs} - Y_{t,mod}$). The dashed vertical line separates the calibration (1984–2014) and validation (2014–2024) periods. **(d)** The normalized (adjusted for amplitude [A] and effective morphodynamic memory [τ_{eff}]) shapes of the convolution kernel functions (K) optimized for all transects across this littoral cell, colored by component (orange: CS, green: CI, blue: Al), with solid lines representing the littoral cell average and shading denoting the 95% within-littoral cell variability across transects. **(e)** Spatial (alongshore) variability of the Root-Mean-Squared-Error ($RMSE$), Pearson correlation coefficient ($Corr$), and standard deviation (STD) of the modeled total shoreline positions during the validation period (2014-2024) in this littoral cell. This panel also features the kernel density estimation (KDE) for each metric across all transects within this littoral cell, alongside their littoral cell-median values shown by their corresponding color (the y-axis is not scaled). **(f-i)** The normalized (for standard deviation [$NSTD$] and Root-Mean-Squared-Error [$NRMSE$]) Taylor diagrams for distinct modeled components and the total shoreline position variability of all transects in this littoral cell, during both calibration and validation periods, where each point corresponds to an individual transect. Credit: basemaps, Earthstar Geographics (via MATLAB (32)).

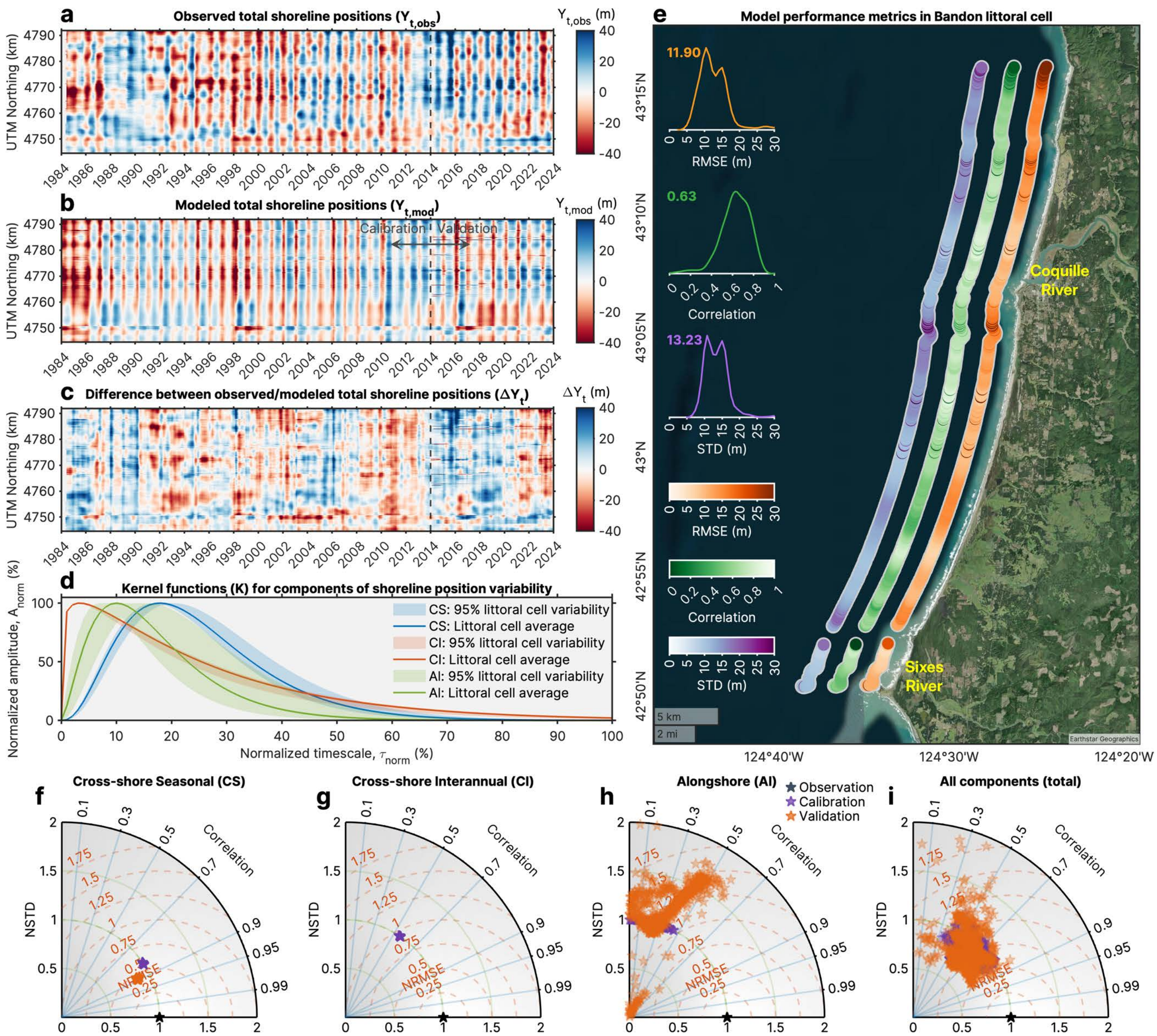

Fig. S14. Hindcast performance of the historical (observed) shoreline positions throughout Bandon littoral cell, Oregon. Spatiotemporal representation (heatmap; y-axis denotes the UTM northing and x-axis specifies time) of the total **(a)** observed ($Y_{t,obs}$) and **(b)** modeled (hindcast) ($Y_{t,mod}$) shoreline positions, alongside **(c)** their difference ($\Delta Y_t = Y_{t,obs} - Y_{t,mod}$). The dashed vertical line separates the calibration (1984–2014) and validation (2014–2024) periods. **(d)** The normalized (adjusted for amplitude [A] and effective morphodynamic memory [τ_{eff}]) shapes of the convolution kernel functions (K) optimized for all transects across this littoral cell, colored by component (orange: CS, green: CI, blue: Al), with solid lines representing the littoral cell average and shading denoting the 95% within-littoral cell variability across transects. **(e)** Spatial (alongshore) variability of the Root-Mean-Squared-Error ($RMSE$), Pearson correlation coefficient ($Corr$), and standard deviation (STD) of the modeled total shoreline positions during the validation period (2014-2024) in this littoral cell. This panel also features the kernel density estimation (KDE) for each metric across all transects within this littoral cell, alongside their littoral cell-median values shown by their corresponding color (the y-axis is not scaled). **(f-i)** The normalized (for standard deviation [$NSTD$] and Root-Mean-Squared-Error [$NRMSE$]) Taylor diagrams for distinct modeled components and the total shoreline position variability of all transects in this littoral cell, during both calibration and validation periods, where each point corresponds to an individual transect. Credit: basemaps, Earthstar Geographics (via MATLAB (32)).

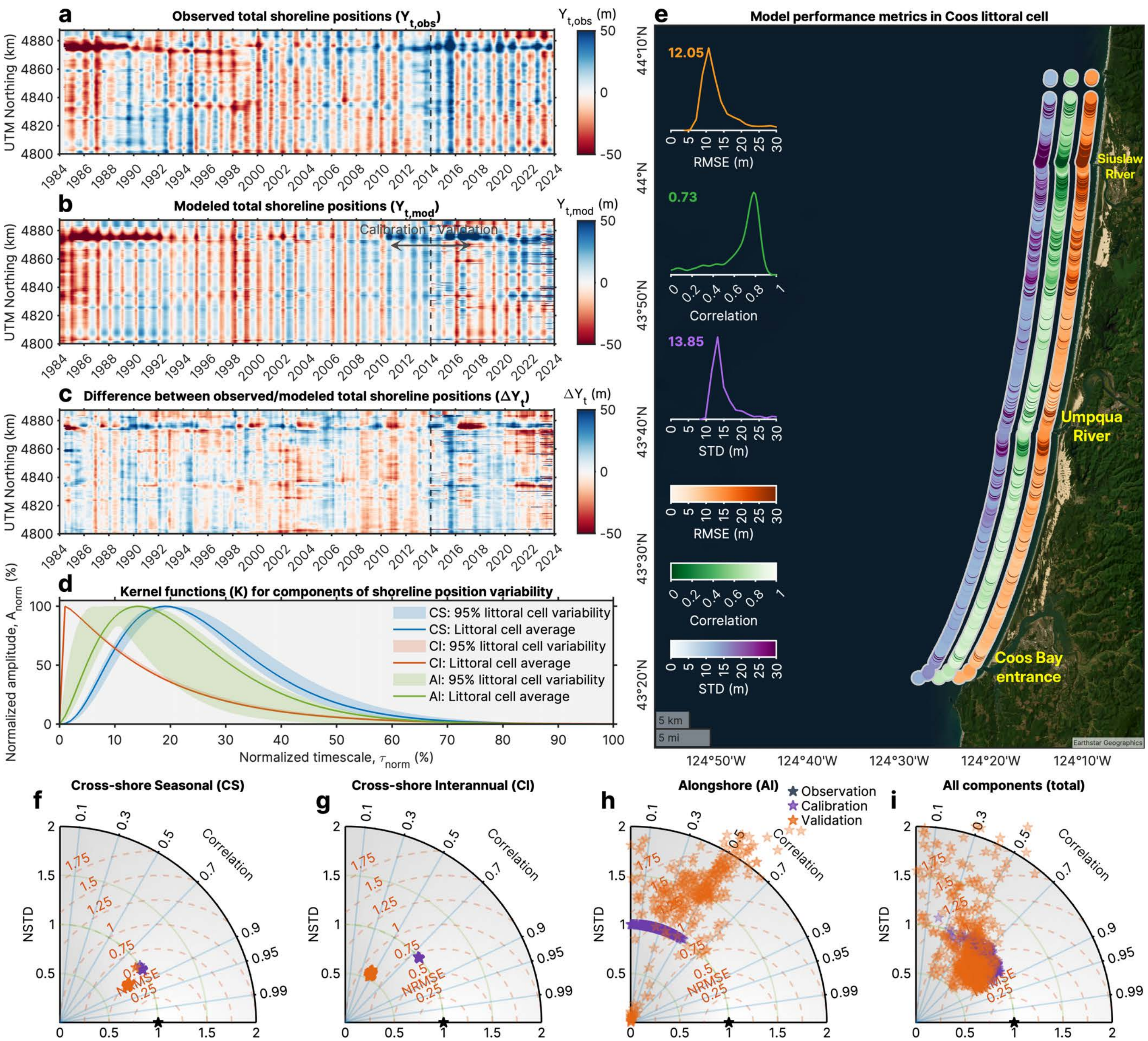

Fig. S15. Hindcast performance of the historical (observed) shoreline positions throughout Coos littoral cell, Oregon. Spatiotemporal representation (heatmap; y-axis denotes the UTM northing and x-axis specifies time) of the total **(a)** observed ($Y_{t,obs}$) and **(b)** modeled (hindcast) ($Y_{t,mod}$) shoreline positions, alongside **(c)** their difference ($\Delta Y_t = Y_{t,obs} - Y_{t,mod}$). The dashed vertical line separates the calibration (1984–2014) and validation (2014–2024) periods. **(d)** The normalized (adjusted for amplitude [A] and effective morphodynamic memory [τ_{eff}]) shapes of the convolution kernel functions (K) optimized for all transects across this littoral cell, colored by component (orange: CS, green: CI, blue: Al), with solid lines representing the littoral cell average and shading denoting the 95% within-littoral cell variability across transects. **(e)** Spatial (alongshore) variability of the Root-Mean-Squared-Error ($RMSE$), Pearson correlation coefficient ($Corr$), and standard deviation (STD) of the modeled total shoreline positions during the validation period (2014-2024) in this littoral cell. This panel also features the kernel density estimation (KDE) for each metric across all transects within this littoral cell, alongside their littoral cell-median values shown by their corresponding color (the y-axis is not scaled). **(f-i)** The normalized (for standard deviation [$NSTD$] and Root-Mean-Squared-Error [$NRMSE$]) Taylor diagrams for distinct modeled components and the total shoreline position variability of all transects in this littoral cell, during both calibration and validation periods, where each point corresponds to an individual transect. Credit: basemaps, Earthstar Geographics (via MATLAB (32)).

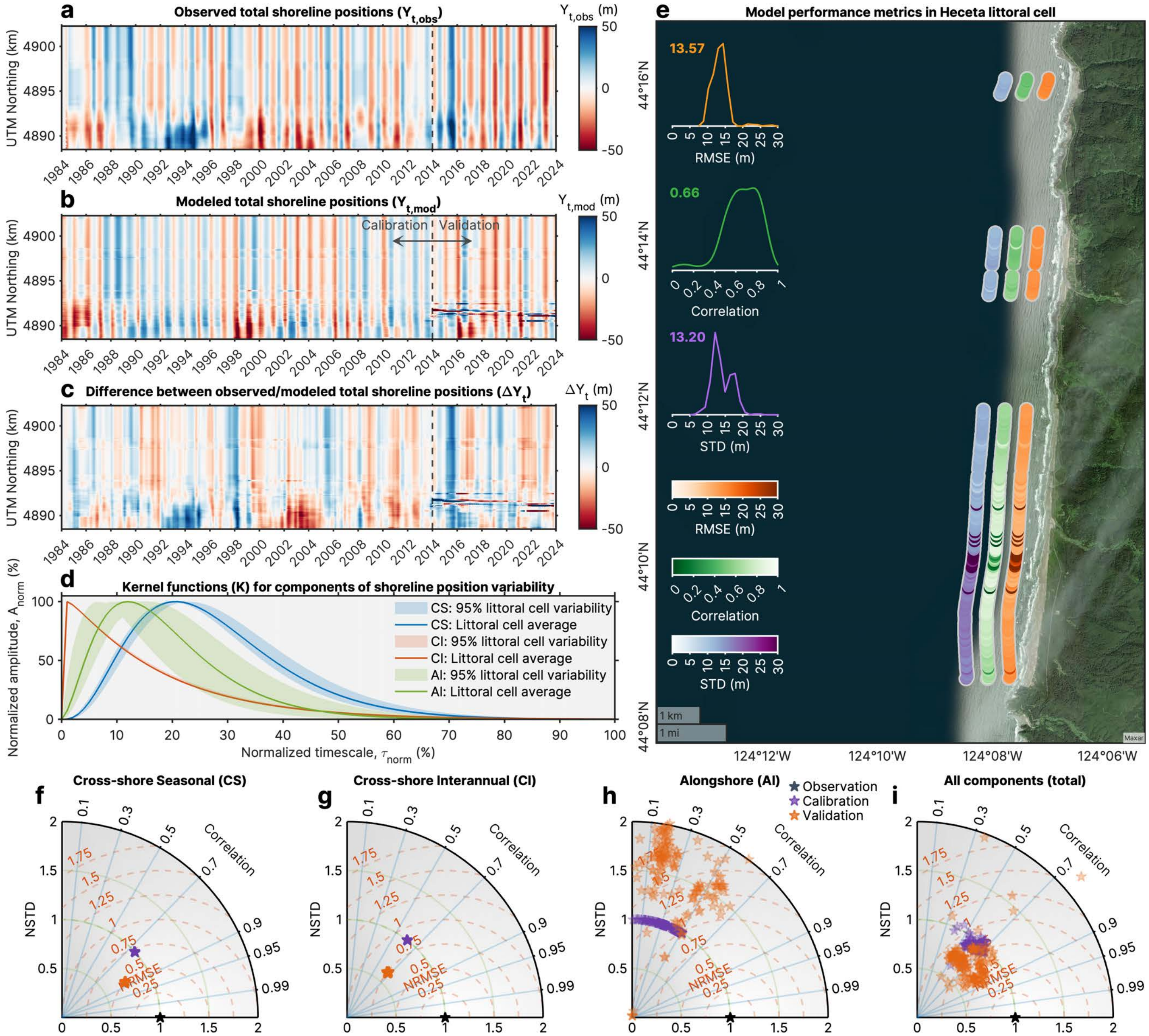

Fig. S16. Hindcast performance of the historical (observed) shoreline positions throughout Heceta littoral cell, Oregon. Spatiotemporal representation (heatmap; y-axis denotes the UTM northing and x-axis specifies time) of the total **(a)** observed ($Y_{t,obs}$) and **(b)** modeled (hindcast) ($Y_{t,mod}$) shoreline positions, alongside **(c)** their difference ($\Delta Y_t = Y_{t,obs} - Y_{t,mod}$). The dashed vertical line separates the calibration (1984–2014) and validation (2014–2024) periods. **(d)** The normalized (adjusted for amplitude [A] and effective morphodynamic memory [τ_{eff}]) shapes of the convolution kernel functions (K) optimized for all transects across this littoral cell, colored by component (orange: CS, green: CI, blue: Al), with solid lines representing the littoral cell average and shading denoting the 95% within-littoral cell variability across transects. **(e)** Spatial (alongshore) variability of the Root-Mean-Squared-Error ($RMSE$), Pearson correlation coefficient ($Corr$), and standard deviation (STD) of the modeled total shoreline positions during the validation period (2014-2024) in this littoral cell. This panel also features the kernel density estimation (KDE) for each metric across all transects within this littoral cell, alongside their littoral cell-median values shown by their corresponding color (the y-axis is not scaled). **(f-i)** The normalized (for standard deviation [$NSTD$] and Root-Mean-Squared-Error [$NRMSE$]) Taylor diagrams for distinct modeled components and the total shoreline position variability of all transects in this littoral cell, during both calibration and validation periods, where each point corresponds to an individual transect. Credit: basemaps, Earthstar Geographics (via MATLAB (32)).

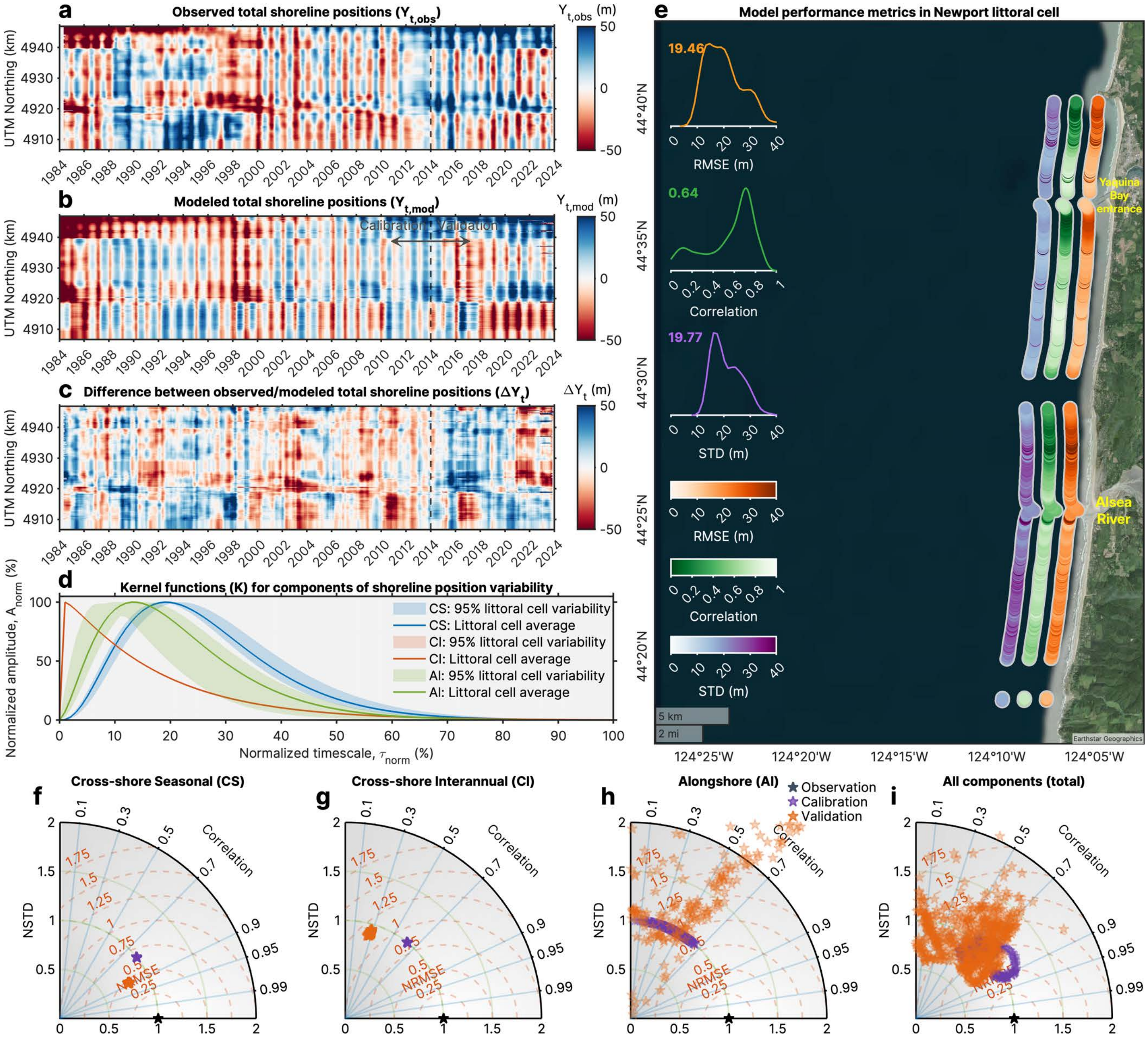

Fig. S17. Hindcast performance of the historical (observed) shoreline positions throughout Newport littoral cell, Oregon. Spatiotemporal representation (heatmap; y-axis denotes the UTM northing and x-axis specifies time) of the total **(a)** observed ($Y_{t,obs}$) and **(b)** modeled (hindcast) ($Y_{t,mod}$) shoreline positions, alongside **(c)** their difference ($\Delta Y_t = Y_{t,obs} - Y_{t,mod}$). The dashed vertical line separates the calibration (1984–2014) and validation (2014–2024) periods. **(d)** The normalized (adjusted for amplitude [A] and effective morphodynamic memory [τ_{eff}]) shapes of the convolution kernel functions (K) optimized for all transects across this littoral cell, colored by component (orange: CS, green: CI, blue: Al), with solid lines representing the littoral cell average and shading denoting the 95% within-littoral cell variability across transects. **(e)** Spatial (alongshore) variability of the Root-Mean-Squared-Error ($RMSE$), Pearson correlation coefficient ($Corr$), and standard deviation (STD) of the modeled total shoreline positions during the validation period (2014-2024) in this littoral cell. This panel also features the kernel density estimation (KDE) for each metric across all transects within this littoral cell, alongside their littoral cell-median values shown by their corresponding color (the y-axis is not scaled). **(f-i)** The normalized (for standard deviation [$NSTD$] and Root-Mean-Squared-Error [$NRMSE$]) Taylor diagrams for distinct modeled components and the total shoreline position variability of all transects in this littoral cell, during both calibration and validation periods, where each point corresponds to an individual transect. Credit: basemaps, Earthstar Geographics (via MATLAB (32)).

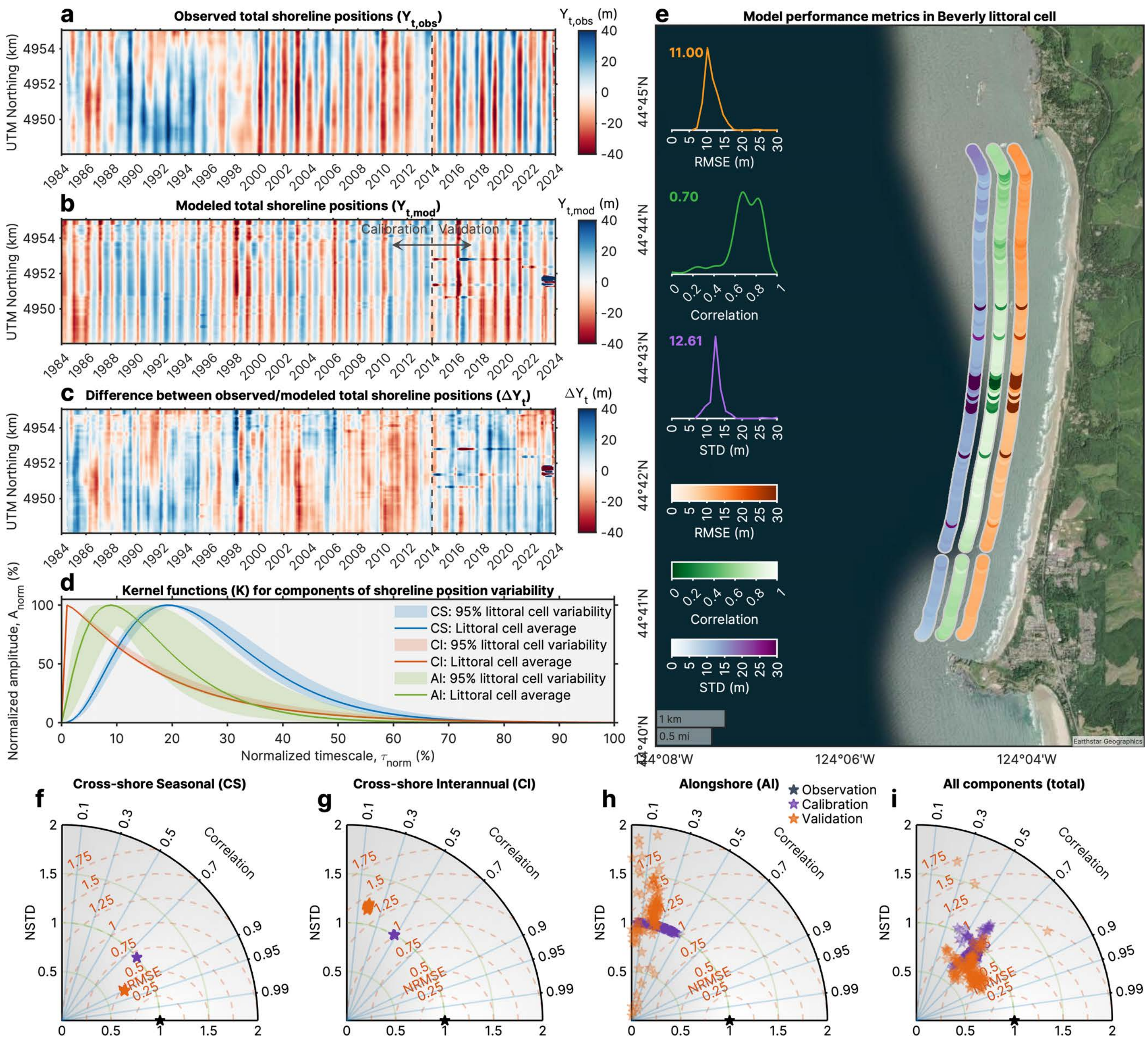

Fig. S18. Hindcast performance of the historical (observed) shoreline positions throughout Beverly littoral cell, Oregon. Spatiotemporal representation (heatmap; y-axis denotes the UTM northing and x-axis specifies time) of the total **(a)** observed ($Y_{t,obs}$) and **(b)** modeled (hindcast) ($Y_{t,mod}$) shoreline positions, alongside **(c)** their difference ($\Delta Y_t = Y_{t,obs} - Y_{t,mod}$). The dashed vertical line separates the calibration (1984–2014) and validation (2014–2024) periods. **(d)** The normalized (adjusted for amplitude [A] and effective morphodynamic memory [τ_{eff}]) shapes of the convolution kernel functions (K) optimized for all transects across this littoral cell, colored by component (orange: CS, green: CI, blue: Al), with solid lines representing the littoral cell average and shading denoting the 95% within-littoral cell variability across transects. **(e)** Spatial (alongshore) variability of the Root-Mean-Squared-Error ($RMSE$), Pearson correlation coefficient ($Corr$), and standard deviation (STD) of the modeled total shoreline positions during the validation period (2014-2024) in this littoral cell. This panel also features the kernel density estimation (KDE) for each metric across all transects within this littoral cell, alongside their littoral cell-median values shown by their corresponding color (the y-axis is not scaled). **(f-i)** The normalized (for standard deviation [$NSTD$] and Root-Mean-Squared-Error [$NRMSE$]) Taylor diagrams for distinct modeled components and the total shoreline position variability of all transects in this littoral cell, during both calibration and validation periods, where each point corresponds to an individual transect. Credit: basemaps, Earthstar Geographics (via MATLAB (32)).

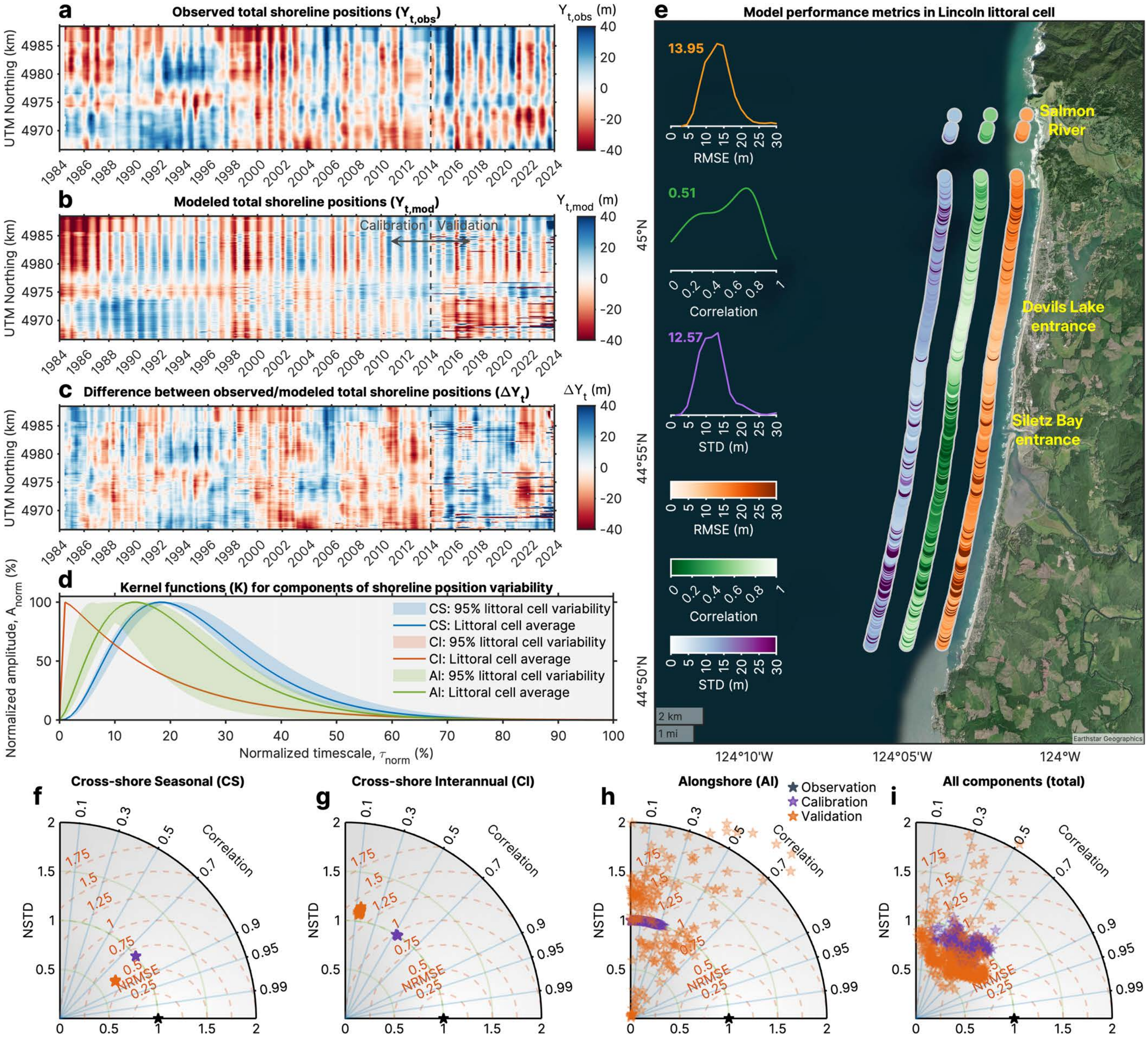

Fig. S19. Hindcast performance of the historical (observed) shoreline positions throughout Lincoln littoral cell, Oregon. Spatiotemporal representation (heatmap; y-axis denotes the UTM northing and x-axis specifies time) of the total **(a)** observed ($Y_{t,obs}$) and **(b)** modeled (hindcast) ($Y_{t,mod}$) shoreline positions, alongside **(c)** their difference ($\Delta Y_t = Y_{t,obs} - Y_{t,mod}$). The dashed vertical line separates the calibration (1984–2014) and validation (2014–2024) periods. **(d)** The normalized (adjusted for amplitude [A] and effective morphodynamic memory [τ_{eff}]) shapes of the convolution kernel functions (K) optimized for all transects across this littoral cell, colored by component (orange: CS, green: CI, blue: Al), with solid lines representing the littoral cell average and shading denoting the 95% within-littoral cell variability across transects. **(e)** Spatial (alongshore) variability of the Root-Mean-Squared-Error ($RMSE$), Pearson correlation coefficient ($Corr$), and standard deviation (STD) of the modeled total shoreline positions during the validation period (2014-2024) in this littoral cell. This panel also features the kernel density estimation (KDE) for each metric across all transects within this littoral cell, alongside their littoral cell-median values shown by their corresponding color (the y-axis is not scaled). **(f-i)** The normalized (for standard deviation [$NSTD$] and Root-Mean-Squared-Error [$NRMSE$]) Taylor diagrams for distinct modeled components and the total shoreline position variability of all transects in this littoral cell, during both calibration and validation periods, where each point corresponds to an individual transect. Credit: basemaps, Earthstar Geographics (via MATLAB (32)).

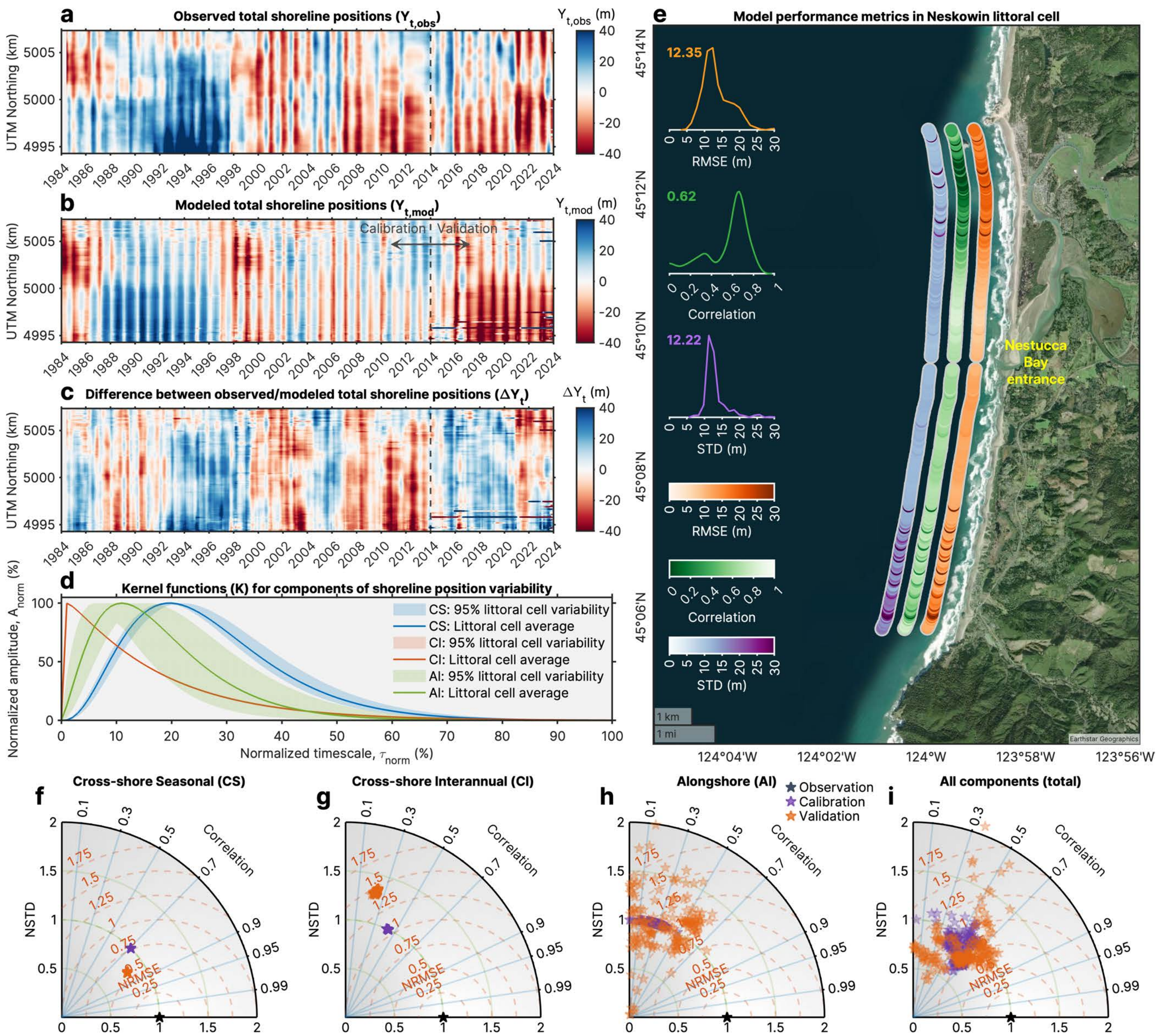

Fig. S20. Hindcast performance of the historical (observed) shoreline positions throughout Neskowin littoral cell, Oregon. Spatiotemporal representation (heatmap; y-axis denotes the UTM northing and x-axis specifies time) of the total **(a)** observed ($Y_{t,obs}$) and **(b)** modeled (hindcast) ($Y_{t,mod}$) shoreline positions, alongside **(c)** their difference ($\Delta Y_t = Y_{t,obs} - Y_{t,mod}$). The dashed vertical line separates the calibration (1984–2014) and validation (2014–2024) periods. **(d)** The normalized (adjusted for amplitude [A] and effective morphodynamic memory [τ_{eff}]) shapes of the convolution kernel functions (K) optimized for all transects across this littoral cell, colored by component (orange: CS, green: CI, blue: Al), with solid lines representing the littoral cell average and shading denoting the 95% within-littoral cell variability across transects. **(e)** Spatial (alongshore) variability of the Root-Mean-Squared-Error ($RMSE$), Pearson correlation coefficient ($Corr$), and standard deviation (STD) of the modeled total shoreline positions during the validation period (2014-2024) in this littoral cell. This panel also features the kernel density estimation (KDE) for each metric across all transects within this littoral cell, alongside their littoral cell-median values shown by their corresponding color (the y-axis is not scaled). **(f-i)** The normalized (for standard deviation [$NSTD$] and Root-Mean-Squared-Error [$NRMSE$]) Taylor diagrams for distinct modeled components and the total shoreline position variability of all transects in this littoral cell, during both calibration and validation periods, where each point corresponds to an individual transect. Credit: basemaps, Earthstar Geographics (via MATLAB (32)).

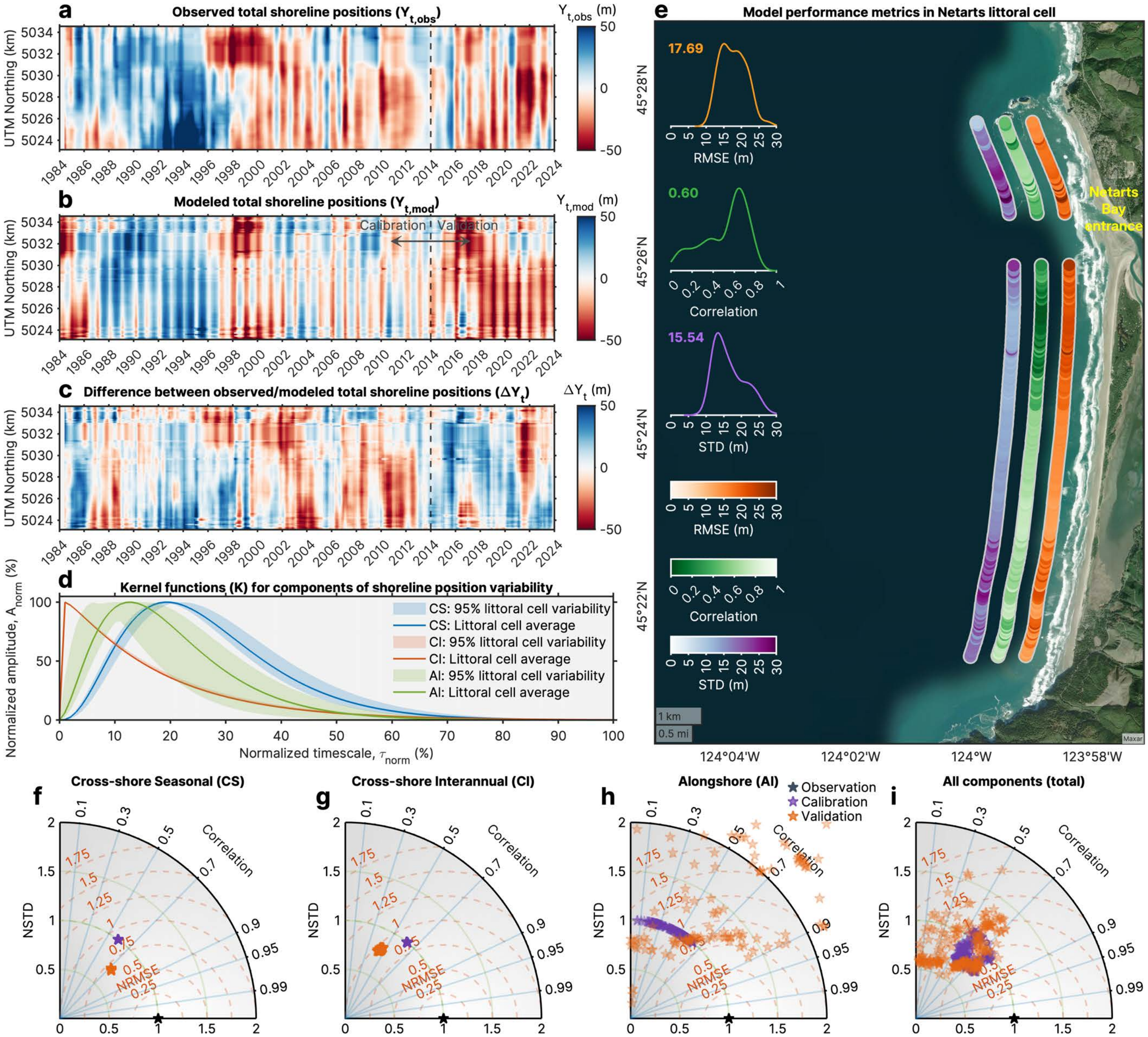

Fig. S21. Hindcast performance of the historical (observed) shoreline positions throughout Netarts littoral cell, Oregon. Spatiotemporal representation (heatmap; y-axis denotes the UTM northing and x-axis specifies time) of the total **(a)** observed ($Y_{t,obs}$) and **(b)** modeled (hindcast) ($Y_{t,mod}$) shoreline positions, alongside **(c)** their difference ($\Delta Y_t = Y_{t,obs} - Y_{t,mod}$). The dashed vertical line separates the calibration (1984–2014) and validation (2014–2024) periods. **(d)** The normalized (adjusted for amplitude [A] and effective morphodynamic memory [τ_{eff}]) shapes of the convolution kernel functions (K) optimized for all transects across this littoral cell, colored by component (orange: CS, green: CI, blue: Al), with solid lines representing the littoral cell average and shading denoting the 95% within-littoral cell variability across transects. **(e)** Spatial (alongshore) variability of the Root-Mean-Squared-Error ($RMSE$), Pearson correlation coefficient ($Corr$), and standard deviation (STD) of the modeled total shoreline positions during the validation period (2014-2024) in this littoral cell. This panel also features the kernel density estimation (KDE) for each metric across all transects within this littoral cell, alongside their littoral cell-median values shown by their corresponding color (the y-axis is not scaled). **(f-i)** The normalized (for standard deviation [$NSTD$] and Root-Mean-Squared-Error [$NRMSE$]) Taylor diagrams for distinct modeled components and the total shoreline position variability of all transects in this littoral cell, during both calibration and validation periods, where each point corresponds to an individual transect. Credit: basemaps, Earthstar Geographics (via MATLAB (32)).

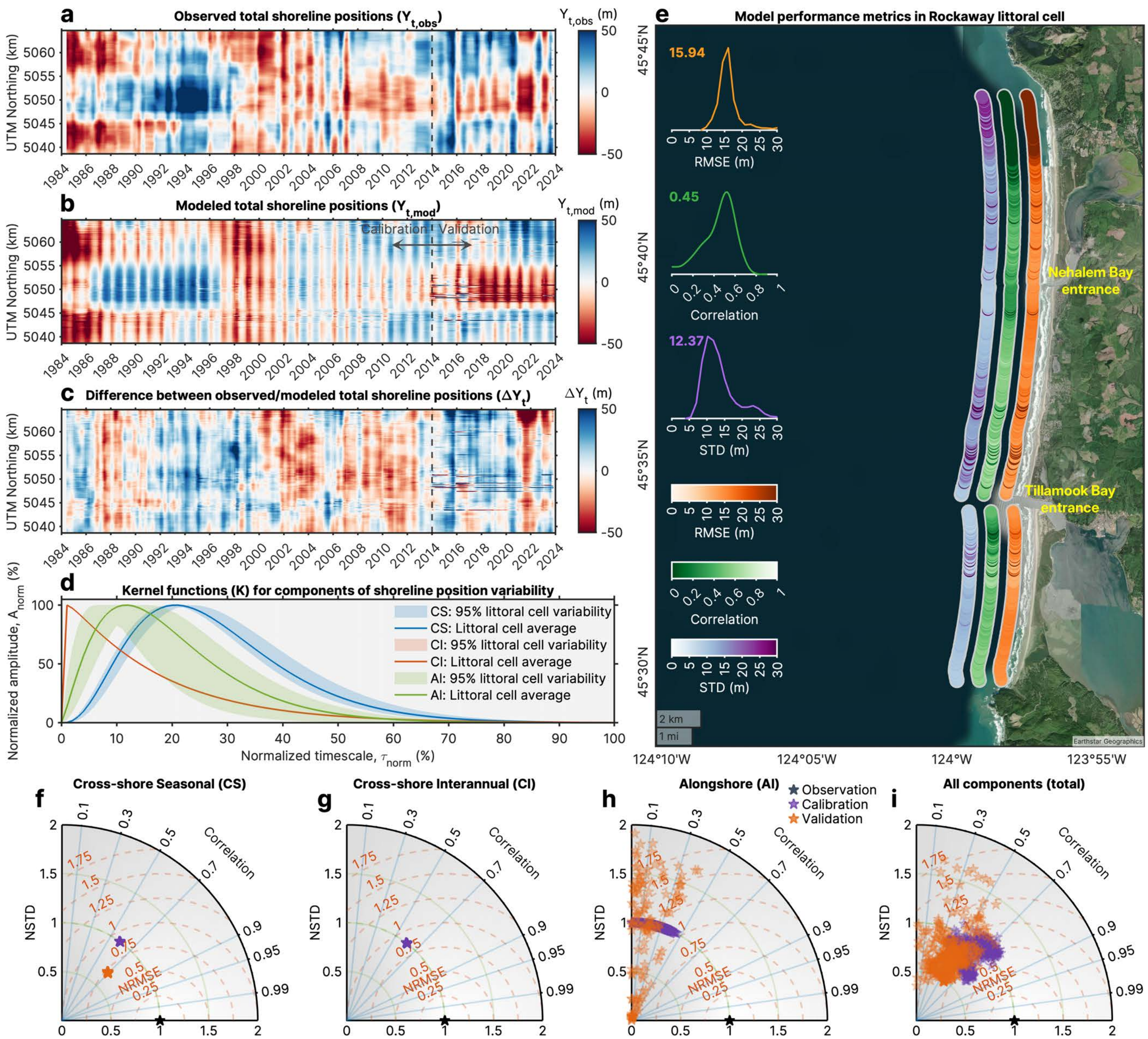

Fig. S22. Hindcast performance of the historical (observed) shoreline positions throughout Rockaway littoral cell, Oregon. Spatiotemporal representation (heatmap; y-axis denotes the UTM northing and x-axis specifies time) of the total **(a)** observed ($Y_{t,obs}$) and **(b)** modeled (hindcast) ($Y_{t,mod}$) shoreline positions, alongside **(c)** their difference ($\Delta Y_t = Y_{t,obs} - Y_{t,mod}$). The dashed vertical line separates the calibration (1984–2014) and validation (2014–2024) periods. **(d)** The normalized (adjusted for amplitude [A] and effective morphodynamic memory [τ_{eff}]) shapes of the convolution kernel functions (K) optimized for all transects across this littoral cell, colored by component (orange: CS, green: CI, blue: Al), with solid lines representing the littoral cell average and shading denoting the 95% within-littoral cell variability across transects. **(e)** Spatial (alongshore) variability of the Root-Mean-Squared-Error ($RMSE$), Pearson correlation coefficient ($Corr$), and standard deviation (STD) of the modeled total shoreline positions during the validation period (2014-2024) in this littoral cell. This panel also features the kernel density estimation (KDE) for each metric across all transects within this littoral cell, alongside their littoral cell-median values shown by their corresponding color (the y-axis is not scaled). **(f-i)** The normalized (for standard deviation [$NSTD$] and Root-Mean-Squared-Error [$NRMSE$]) Taylor diagrams for distinct modeled components and the total shoreline position variability of all transects in this littoral cell, during both calibration and validation periods, where each point corresponds to an individual transect. Credit: basemaps, Earthstar Geographics (via MATLAB (32)).

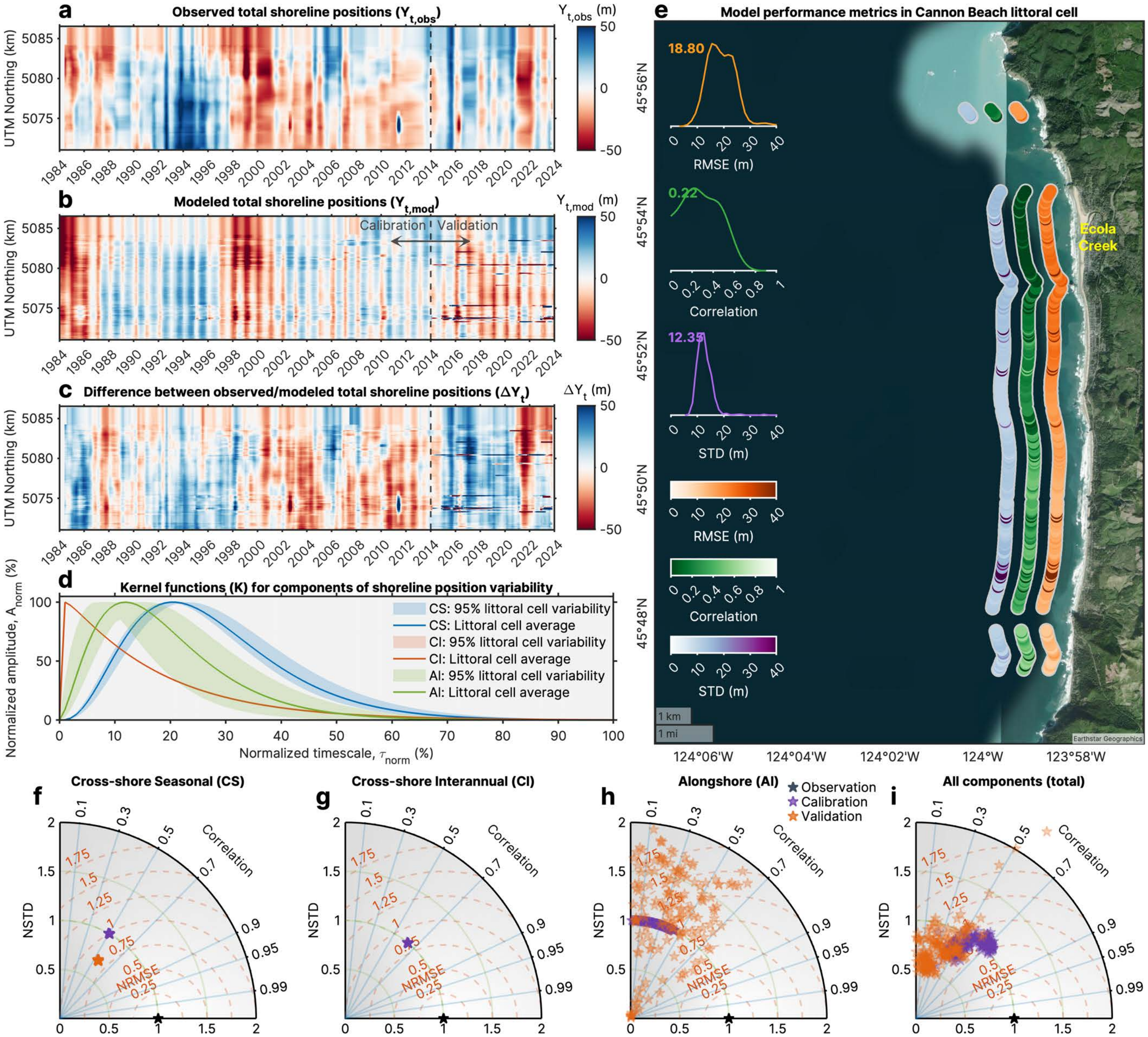

Fig. S23. Hindcast performance of the historical (observed) shoreline positions throughout Cannon Beach littoral cell, Oregon. Spatiotemporal representation (heatmap; y-axis denotes the UTM northing and x-axis specifies time) of the total **(a)** observed ($Y_{t,obs}$) and **(b)** modeled (hindcast) ($Y_{t,mod}$) shoreline positions, alongside **(c)** their difference ($\Delta Y_t = Y_{t,obs} - Y_{t,mod}$). The dashed vertical line separates the calibration (1984–2014) and validation (2014–2024) periods. **(d)** The normalized (adjusted for amplitude [A] and effective morphodynamic memory [τ_{eff}]) shapes of the convolution kernel functions (K) optimized for all transects across this littoral cell, colored by component (orange: CS, green: CI, blue: Al), with solid lines representing the littoral cell average and shading denoting the 95% within-littoral cell variability across transects. **(e)** Spatial (alongshore) variability of the Root-Mean-Squared-Error ($RMSE$), Pearson correlation coefficient ($Corr$), and standard deviation (STD) of the modeled total shoreline positions during the validation period (2014-2024) in this littoral cell. This panel also features the kernel density estimation (KDE) for each metric across all transects within this littoral cell, alongside their littoral cell-median values shown by their corresponding color (the y-axis is not scaled). **(f-i)** The normalized (for standard deviation [$NSTD$] and Root-Mean-Squared-Error [$NRMSE$]) Taylor diagrams for distinct modeled components and the total shoreline position variability of all transects in this littoral cell, during both calibration and validation periods, where each point corresponds to an individual transect. Credit: basemaps, Earthstar Geographics (via MATLAB (32)).

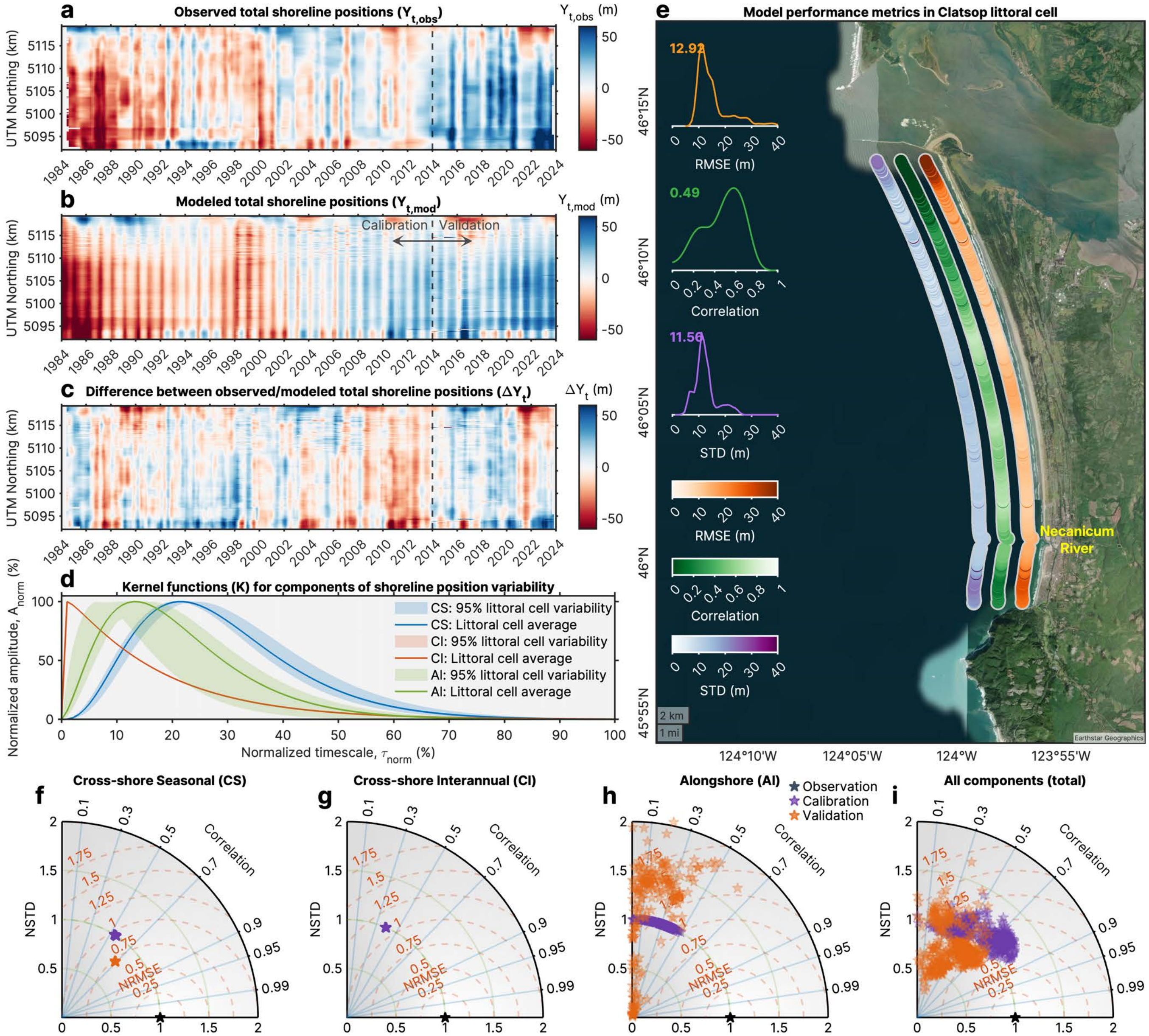

Fig. S24. Hindcast performance of the historical (observed) shoreline positions throughout Clatsop littoral cell, Oregon. Spatiotemporal representation (heatmap; y-axis denotes the UTM northing and x-axis specifies time) of the total **(a)** observed ($Y_{t,obs}$) and **(b)** modeled (hindcast) ($Y_{t,mod}$) shoreline positions, alongside **(c)** their difference ($\Delta Y_t = Y_{t,obs} - Y_{t,mod}$). The dashed vertical line separates the calibration (1984–2014) and validation (2014–2024) periods. **(d)** The normalized (adjusted for amplitude [A] and effective morphodynamic memory [τ_{eff}]) shapes of the convolution kernel functions (K) optimized for all transects across this littoral cell, colored by component (orange: CS, green: CI, blue: Al), with solid lines representing the littoral cell average and shading denoting the 95% within-littoral cell variability across transects. **(e)** Spatial (alongshore) variability of the Root-Mean-Squared-Error ($RMSE$), Pearson correlation coefficient ($Corr$), and standard deviation (STD) of the modeled total shoreline positions during the validation period (2014-2024) in this littoral cell. This panel also features the kernel density estimation (KDE) for each metric across all transects within this littoral cell, alongside their littoral cell-median values shown by their corresponding color (the y-axis is not scaled). **(f-i)** The normalized (for standard deviation [$NSTD$] and Root-Mean-Squared-Error [$NRMSE$]) Taylor diagrams for distinct modeled components and the total shoreline position variability of all transects in this littoral cell, during both calibration and validation periods, where each point corresponds to an individual transect. Credit: basemaps, Earthstar Geographics (via MATLAB (32)).

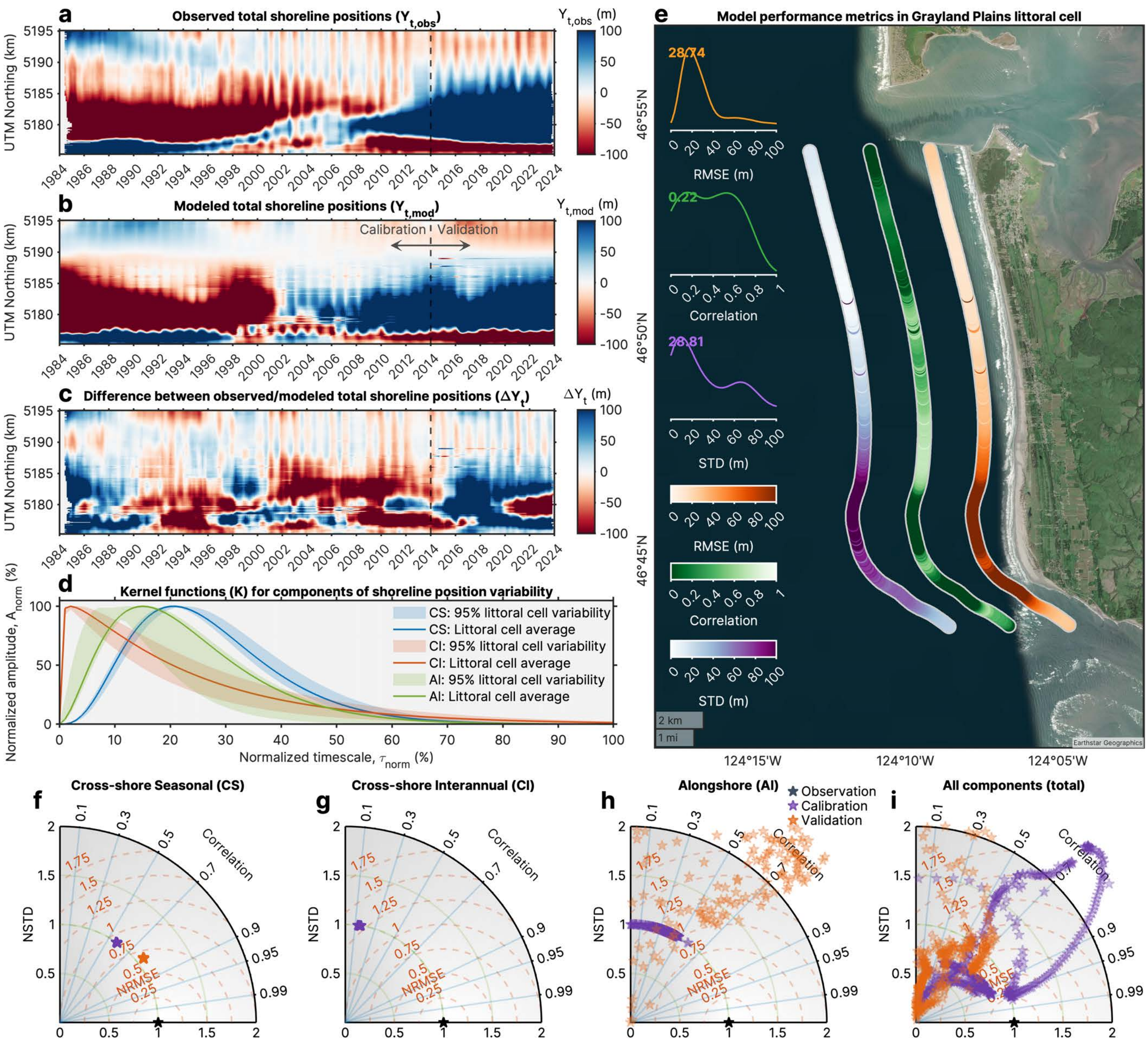

Fig. S25. Hindcast performance of the historical (observed) shoreline positions throughout Grayland Plains littoral cell, Washington. Spatiotemporal representation (heatmap; y-axis denotes the UTM northing and x-axis specifies time) of the total **(a)** observed ($Y_{t,obs}$) and **(b)** modeled (hindcast) ($Y_{t,mod}$) shoreline positions, alongside **(c)** their difference ($\Delta Y_t = Y_{t,obs} - Y_{t,mod}$). The dashed vertical line separates the calibration (1984–2014) and validation (2014–2024) periods. **(d)** The normalized (adjusted for amplitude [A] and effective morphodynamic memory [τ_{eff}]) shapes of the convolution kernel functions (K) optimized for all transects across this littoral cell, colored by component (orange: CS, green: CI, blue: Al), with solid lines representing the littoral cell average and shading denoting the 95% within-littoral cell variability across transects. **(e)** Spatial (alongshore) variability of the Root-Mean-Squared-Error ($RMSE$), Pearson correlation coefficient ($Corr$), and standard deviation (STD) of the modeled total shoreline positions during the validation period (2014-2024) in this littoral cell. This panel also features the kernel density estimation (KDE) for each metric across all transects within this littoral cell, alongside their littoral cell-median values shown by their corresponding color (the y-axis is not scaled). **(f-i)** The normalized (for standard deviation [$NSTD$] and Root-Mean-Squared-Error [$NRMSE$]) Taylor diagrams for distinct modeled components and the total shoreline position variability of all transects in this littoral cell, during both calibration and validation periods, where each point corresponds to an individual transect. Credit: basemaps, Earthstar Geographics (via MATLAB (32)).

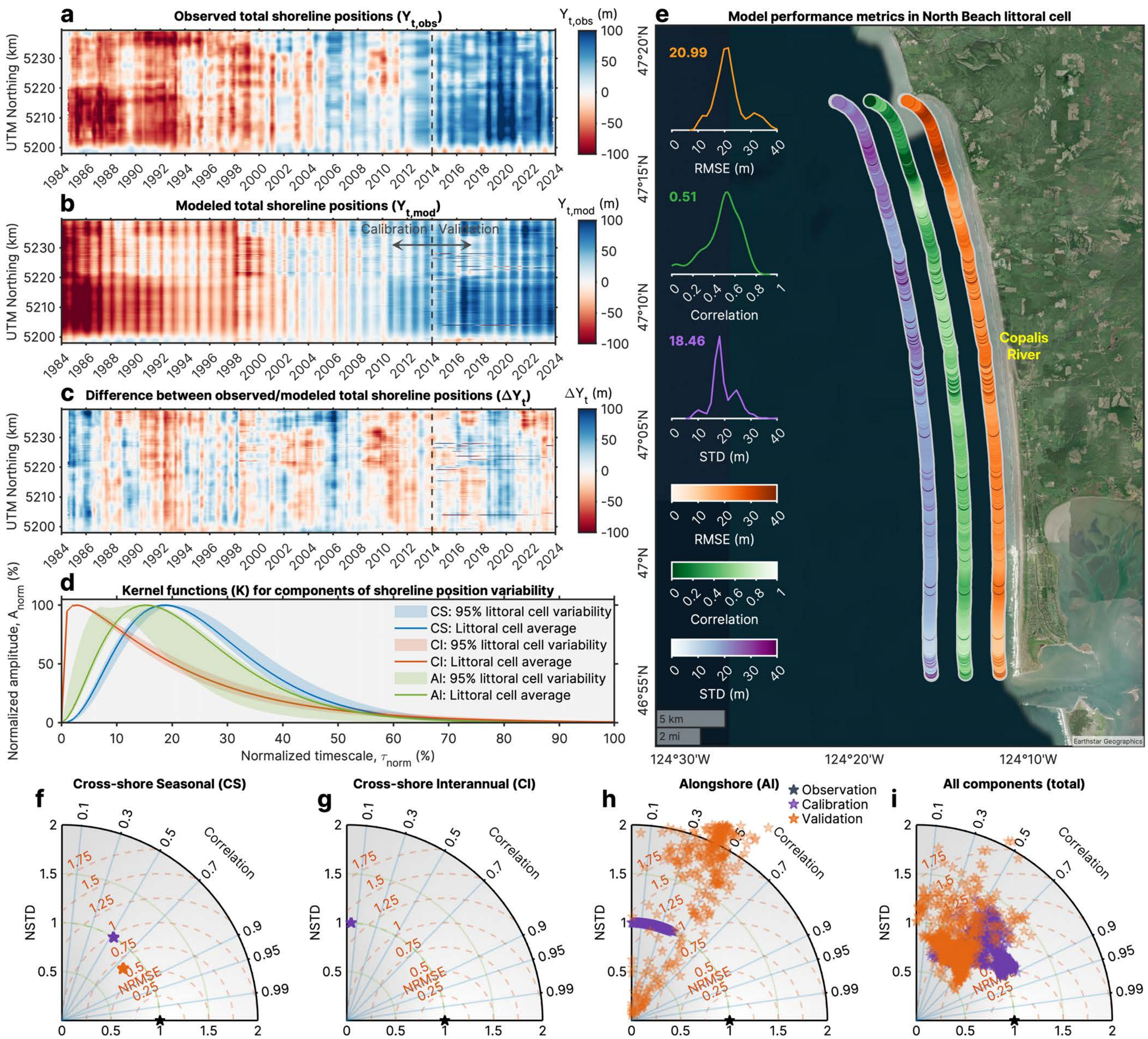

Fig. S26. Hindcast performance of the historical (observed) shoreline positions throughout North Beach littoral cell, Washington. Spatiotemporal representation (heatmap; y-axis denotes the UTM northing and x-axis specifies time) of the total **(a)** observed ($Y_{t,obs}$) and **(b)** modeled (hindcast) ($Y_{t,mod}$) shoreline positions, alongside **(c)** their difference ($\Delta Y_t = Y_{t,obs} - Y_{t,mod}$). The dashed vertical line separates the calibration (1984–2014) and validation (2014–2024) periods. **(d)** The normalized (adjusted for amplitude [A] and effective morphodynamic memory [τ_{eff}]) shapes of the convolution kernel functions (K) optimized for all transects across this littoral cell, colored by component (orange: CS, green: CI, blue: Al), with solid lines representing the littoral cell average and shading denoting the 95% within-littoral cell variability across transects. **(e)** Spatial (alongshore) variability of the Root-Mean-Squared-Error ($RMSE$), Pearson correlation coefficient ($Corr$), and standard deviation (STD) of the modeled total shoreline positions during the validation period (2014-2024) in this littoral cell. This panel also features the kernel density estimation (KDE) for each metric across all transects within this littoral cell, alongside their littoral cell-median values shown by their corresponding color (the y-axis is not scaled). **(f-i)** The normalized (for standard deviation [$NSTD$] and Root-Mean-Squared-Error [$NRMSE$]) Taylor diagrams for distinct modeled components and the total shoreline position variability of all transects in this littoral cell, during both calibration and validation periods, where each point corresponds to an individual transect. Credit: basemaps, Earthstar Geographics (via MATLAB (32)).

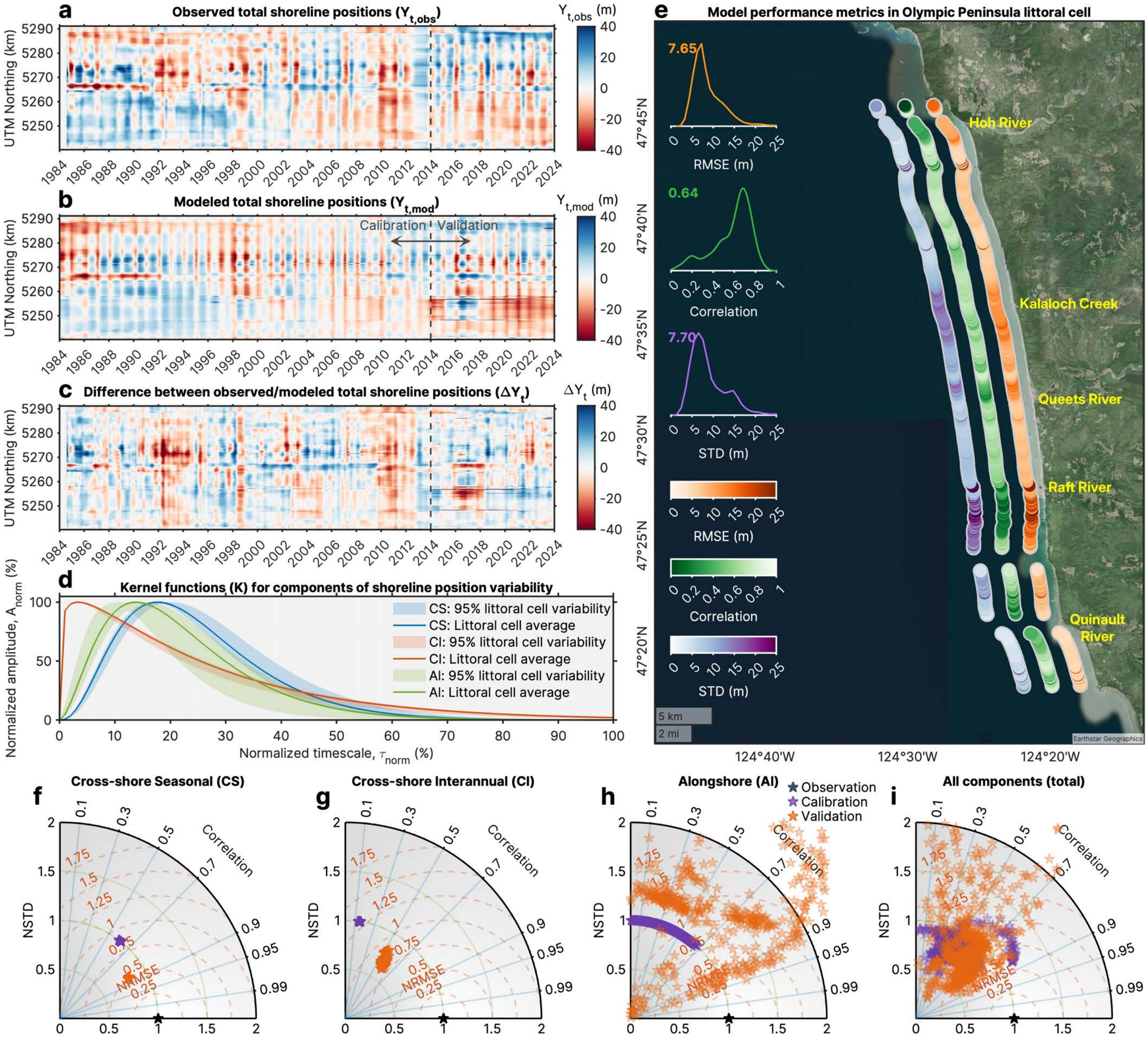

Fig. S27. Hindcast performance of the historical (observed) shoreline positions throughout Olympic Peninsula littoral cell, Washington. Spatiotemporal representation (heatmap; y-axis denotes the UTM northing and x-axis specifies time) of the total **(a)** observed ($Y_{t,obs}$) and **(b)** modeled (hindcast) ($Y_{t,mod}$) shoreline positions, alongside **(c)** their difference ($\Delta Y_t = Y_{t,obs} - Y_{t,mod}$). The dashed vertical line separates the calibration (1984–2014) and validation (2014–2024) periods. **(d)** The normalized (adjusted for amplitude $[A]$ and effective morphodynamic memory $[\tau_{eff}]$) shapes of the convolution kernel functions (K) optimized for all transects across this littoral cell, colored by component (orange: CS, green: CI, blue: Al), with solid lines representing the littoral cell average and shading denoting the 95% within-littoral cell variability across transects. **(e)** Spatial (alongshore) variability of the Root-Mean-Squared-Error ($RMSE$), Pearson correlation coefficient ($Corr$), and standard deviation (STD) of the modeled total shoreline positions during the validation period (2014-2024) in this littoral cell. This panel also features the kernel density estimation (KDE) for each metric across all transects within this littoral cell, alongside their littoral cell-median values shown by their corresponding color (the y-axis is not scaled). **(f-i)** The normalized (for standard deviation $[NSTD]$ and Root-Mean-Squared-Error $[NRMSE]$) Taylor diagrams for distinct modeled components and the total shoreline position variability of all transects in this littoral cell, during both calibration and validation periods, where each point corresponds to an individual transect. Credit: basemaps, Earthstar Geographics (via MATLAB (32)).

References

1. S Vitousek, PL Barnard, P Limber, L Erikson, B Cole, A model integrating longshore and cross-shore processes for predicting long-term shoreline response to climate change. *J. Geophys. Res. Earth Surf.* **122**, 782–806 (2017).
2. M Taherkhani, et al., ENSO and PDO drive shoreline position anomalies in the US Pacific Northwest. *PNAS Nexus* **5**, pgaf404 (2026).
3. P Ruggiero, et al., National assessment of shoreline change: historical shoreline change along the pacific northwest coast, (US Geological Survey), Technical report (2013).
4. T Durrant, M Hemer, G Smith, C Trenham, D Greenslade, Cawcr wave hindcast-aggregated collection. *V5. CSIRO. Serv. Collect.* (2019).
5. CSIRO Data Access Portal, CAWCR Wave Hindcast Aggregated Collection (https://data.csiro.au/collection/csiro:39819) (2024).
6. T Durrant, D Greenslade, M Hemer, C Trenham, *A global wave hindcast focussed on the Central and South Pacific.* (Citeseer) Vol. 40, (2014).
7. GA Smith, et al., Global wave hindcast with australian and pacific island focus: From past to present. *Geosci. Data J.* **8**, 24–33 (2021).
8. JC Allan, et al., *Coastal flood hazard study, Tillamook County, Oregon.* (Oregon Department of Geology and Mineral Industries), (2015).
9. N Booij, RC Ris, LH Holthuijsen, A third-generation wave model for coastal regions: 1. model description and validation. *J. geophysical research: Ocean.* **104**, 7649–7666 (1999).
10. Center for Operational Oceanographic Products and Services, NOAA Tides and Currents (https://tidesandcurrents.noaa.gov/map/index.html) (2024).
11. Center for Operational Oceanographic Products and Services, NOAA Tides and Currents Web Services (https://tidesandcurrents.noaa.gov/web_services_info.html) (2024).
12. D Buscombe, Y Doherty, KD Splinter, SF Vitousek, Satellite-derived shorelines for the u.s. states of oregon and washington for the period 1984-2023, obtained using coastsat (2025).
13. K Vos, KD Splinter, MD Harley, JA Simmons, IL Turner, Coastsat: A google earth engine-enabled python toolkit to extract shorelines from publicly available satellite imagery. *Environ. Model. & Softw.* **122**, 104528 (2019).
14. OCM Partners, 2002 nasa/usgs airborne lidar assessment of coastal erosion (alace) project for california, oregon, and washington coastlines (https://www.fisheries.noaa.gov/inport/item/49634) (2024).
15. OCM Partners, 2009 oregon department of geology and mineral industries (dogami) oregon lidar: North coast (https://www.fisheries.noaa.gov/inport/item/49906) (2024).
16. NOAA Office for Coastal Management, 2016 usgs west coast el-nino lidar (wa, or, ca) (https://www.fisheries.noaa.gov/inport/item/48222) (2024).
17. P Ruggiero, GM Kaminsky, G Gelfenbaum, B Voigt, Seasonal to interannual morphodynamics along a high-energy dissipative littoral cell. *J. Coast. Res.* **21**, 553–578 (2005).
18. J Allan, R Hart, Oregon beach and shoreline mapping and analysis program: 2007-2008 beach monitoring report, (State of Oregon, Department of Geology and Mineral Industries), Technical report (2008).
19. M Graffin, et al., Monitoring interdecadal coastal change along dissipative beaches via satellite imagery at regional scale. *Camb. Prisms: Coast. Futur.* **1**, e42 (2023).
20. EN Lorenz, *Empirical orthogonal functions and statistical weather prediction.* (Massachusetts Institute of Technology, Department of Meteorology Cambridge) Vol. 1, (1956).
21. Greene, C. et al., The Climate Data Toolbox for MATLAB (https://www.mathworks.com/matlabcentral/fileexchange/61345-eof) (2019).
22. RD Strum, DE Kirk, *First principles of discrete systems and digital signal processing.* (Addison-Wesley Longman Publishing Co., Inc.), (1988).
23. P Bruun, Sea-level rise as a cause of shore erosion. *J. Waterw. Harb. division* **88**, 117–130 (1962).
24. M Aoki, *State space modeling of time series.* (Springer Science & Business Media), (2013).
25. J Montaño, et al., Blind testing of shoreline evolution models. *Sci. reports* **10**, 2137 (2020).
26. S Vitousek, K Vos, KD Splinter, L Erikson, PL Barnard, A model integrating satellite-derived shoreline observations for predicting fine-scale shoreline response to waves and sea-level rise across large coastal regions. *J. Geophys. Res. Earth Surf.* **128**, e2022JF006936 (2023).
27. S Vitousek, et al., Scalable, data-assimilated models predict large-scale shoreline response to waves and sea-level rise. *Sci. Reports* **14**, 28029 (2024).
28. O Repina, et al., Evaluating five shoreline change models against 40 years of field survey data at an embayed sandy beach. *Coast. Eng.* **199**, 104738 (2025).
29. Y Mao, et al., Benchmarking shoreline prediction models over multi-decadal timescales. *Commun. Earth & Environ.* **6**, 581 (2025).
30. RU Moskvichev, et al., Wave driven cross shore and alongshore transport reveal more extreme projections of shoreline change in island environments. *Sci. Reports* **15**, 10794 (2025).
31. K Calcraft, JA Simmons, LA Marshall, KD Splinter, A generalized data-driven shoreline model at the regional scale. *J. Geophys. Res. Mach. Learn. Comput.* **3**, e2025JH000989 (2026).

32. The MathWorks Inc., Matlab version: 24.1 (r2024a) (2024).